ABSTRACT

GILMER, MATTHEW STONECIPHER. Pair-instability Supernova Explosions in 1D, 2D, and 3D and Their Observational Signatures. (Under the direction of Carla Fröhlich.)

Pair-Instability supernovae (PISNe) are an exotic class of supernovae which, in addition to being fascinating in its own right (its very existence is a topic of debate), may be important for many areas of astrophysics (early stellar populations, galaxy/chemical evolution, cosmic reionization, etc.). At present, PISNe are one of the three proposed mechanisms for explaining superluminous supernovae (SLSNe), though one major drawback is that PISN models predict longer rise times to peak luminosity than seen in observations of SLSNe. Model rise times can be reduced by having shallower progenitor envelopes and/or outward mixing of radioactive material during the explosions. Here, we present explosions and light curves for four progenitor models, with relatively shallow envelopes, that span the PISN mass range. Our light curves exhibit significantly shorter rise times than other PISNe light curves and we show that our highest mass model can explain many of the features of SLSN PTF12dam. In addition, we investigate the effects of a multidimensional treatment during the explosive burning phase of PISNe, including the first such treatment in 3D. We find a small amount of outward mixing of radioactive Ni-56 that increases with the number of dimensions, however this mixing is insufficient to significantly alter the light curve rise time. We find significant mixing between the silicon and oxygen rich layers, especially in 3D, that may affect model spectra and should be investigated in the future. We present the neutrino signals expected from our most massive and least massive PISN models. Accounting for neutrino oscillations, we compute the expected event rates for current and future neutrino detectors finding that the signal for a high-mass will be easily detectable out to 10 kpc. Furthermore, the predicted signal is easily distinguishable from those of other supernova types. Finally, we present plans and preliminary results for a new project in which we will explore the effect of our mixing results on PISN spectra.

© Copyright 2018 by Matthew Stonecipher Gilmer

All Rights Reserved

Pair-instability Supernova Explosions in 1D, 2D, and 3D and Their Observational Signatures

by
Matthew Stonecipher Gilmer

A dissertation submitted to the Graduate Faculty of
North Carolina State University
in partial fulfillment of the
requirements for the Degree of
Doctor of Philosophy

Physics

Raleigh, North Carolina

2018

APPROVED BY:

Carla Fröhlich Chair of Advisory Committee	Pierre Gremaud
James P. Kneller	Stephen P. Reynolds

BIOGRAPHY

The author was born in Baton Rouge, LA where he attended both high school and college (at LSU). At LSU, he majored in Physics (Astronomy) with a Mathematics minor. During this time he performed research in theoretical atomic physics under the direction of Professor Mette Gaarde. Also during his time at LSU, he participated in an REU (Research Experience for Undergraduates) at the LIGO Livingston Observatory (he is pleased that they successfully detected gravitational waves about five years later). After graduating from LSU, the author attended NCSU for six years where he worked on supernova hydrodynamics under the direction of Professor Carla Fröhlich. He is currently writing his PhD thesis.

ACKNOWLEDGEMENTS

Many thanks to my PhD advisor Carla Fröhlich for her infectious scientific enthusiasm which helped me stay motivated through this long and arduous endeavor. I would also like to thank the rest of the committee. Thanks to James P. Kneller and Steven P. Reynolds, who both had me as students in courses, for their scientific input and insightful knowledge given during journal club and group meetings. Thanks to Pierre Gremaud for pushing me to think critically about uncertainties.

I would also like to thank my scientific collaborators. Thanks to Raphael Hirschi for providing guidance, as well as stellar models, for this project. Thanks to Alexandra Kozyreva for computing light curves for my explosions and for sharing her extensive knowledge of pair-instability supernovae. Thanks to Manos Chatzopoulos for the FLASH expertise that he provided when I was first learning the code and for his work in our current collaboration on pair-instability supernova spectra. Finally, thanks to Warren Wright for his calculation of detector responses for neutrinos emitted from my explosion. I would also like to thank my fellow graduate students for their support

Finally, I thank my friends and family for their patience, love, and support.

TABLE OF CONTENTS

LIST OF TABLES

LIST OF FIGURES

CHAPTER

1

INTRODUCTION

Pair-instability supernovae (PISNe) are the explosive deaths of stars that produce carbon-oxygen (CO) cores in the mass range 64 $M_\odot \lesssim M_{CO} \lesssim 133\ M_\odot$. Stellar models predict that, for non-rotating stars with zero metallicity, this corresponds to a zero-age main sequence (ZAMS) mass range of $140\ M_\odot < M_{ZAMS} < 260\ M_\odot$ [Heg02]. For stars in this mass range, life is cut short when the pair instability (PI) triggers a contraction of the core shortly after core carbon burning. The contraction is reversed by explosive nuclear burning (of primarily oxygen) which releases enough energy to totally unbind the star (no remnant is formed). An extremely luminous transient follows that, with currently planned instruments, will be detectable out to distances exceeding 13 billion light years (see the discussion in Section 2.5), thereby probing the very first generation of stars. The PI occurs when the radiation pressure (which is the dominant contribution to the total pressure at this stage) in the stellar core is reduced by the reaction $\gamma + \gamma \rightarrow e^- + e^+$. Since the core is mildly degenerate at this point, some of the pressure lost from radiation is restored in the form of degeneracy pressure. However, the result for each reaction is a net decrease in pressure.

PISNe are expected to produce a wide variety of supernova (SN) types and also to span a large range in peak luminosity. On the lower end of the PISN mass range, the explosion energies can be only a few Bethe (1 Bethe equals 10^{51} erg) and the nickel yields may be less than those of ordinary core-collapse supernovae (CCSNe). Consequently, the light curves (LCs) and spectra

may resemble those resulting from other supernova mechanisms. For example, red supergiant and stripped core PISN progenitors would likely look like long-duration luminous Type II-P and Type Ib/Ic SNe, respectively [Kas11; Koz14b]. Low-mass PISNe may even explain some ".Ia supernovae" (named as such because their explosion strength is 1/10th that of ordinary supernovae) [Wha13]. Conversely, near the upper end of the PISN mass range the explosions can be extremely energetic. The yield of radioactive nickel in such explosions can approach 55 $M_\odot$ [Heg02] causing a very luminous long-duration SN. It is this potential for high luminosity that made high-mass PISNe an attractive model for superluminous supernovae (SLSNe) when they (SLSNe) were first observed about a decade ago.

The mechanism was first proposed by Rakavy & Shaviv [Rak67] and very soon after shown to cause explosions in simulations of isentropic oxygen cores by Barkat et al. [Bar67]. They (Barkat et al. [Bar67]) present the results of the explosion of such a 40 $M_\odot$ core which burns enough oxygen to be completely disrupted (a PISN). Remarkably, the results agree very well with modern simulations (although the minimum mass has shifted upwards). They also found that cores of 30 $M_\odot$ or less encountered the PI but the contraction and subsequent burning was only strong enough to cause the star to expand, thereby beginning a sequence of oscillations. Once the oscillations decayed, the star would again evolve towards the PI. The process repeated several times and oxygen was burnt in each iteration. This type of behavior is now termed a pulsational pair-instability supernova (PPISN). In modern simulations, shells of matter are ejected from the stellar envelope. Often the second shell ejected is faster than the first and catches up. The resultant shell collision is extremely efficient in converting kinetic energy to thermal energy which causes a transient whose radiated energy rivals that of full-fledged PISNe [Woo07; Wha14a; Che14b]. For these simulations, the progenitors have helium core masses in the range $35\ M_\odot \lesssim M_{He} \lesssim 65\ M_\odot$. This relatively small mass range can, like the larger mass range of PISNe, produce a shocking diversity of behavior.

It is interesting to note then, that after several decades, models of PISNe have not changed much in their predictions. The fact that vast improvements in scientific computing have resulted in models which still predict the same basic behavior is an indication that the mechanism is viable and should occur in nature. If PISNe do not occur in nature, it can mean one of two things. Either the physical ingredients of the model are incorrect or such large CO cores are not formed. The first possibility is almost unthinkable. After all, the same physical ingredients are have been used in modeling of other astrophysical phenomena for which predictions have been confirmed by observations. The second possibility is more realistic because of the fact that mass loss is, in general, poorly understood. The existence of stars of sufficiently high mass has been established (see the discussion in Section 6.3) but it remains unknown whether or not they can retain enough mass to form the large CO cores. In models of PISN progenitors, empir-

ical rates are extrapolated to unconstrained regimes of higher stellar masses. Observational evidence of PISNe would, in fact, provide valuable constraints on mass loss for stars of very high mass. The absence of any confirmed PISNe does not, however, yet constrain mass loss to be too high. One reason for this is that stars of very high mass are rare and it is possible that we have yet to observe the death of such a rare star. Furthermore, PISNe are thought to be more likely for stars made from low-metallicity gas (i.e. in the distant/early universe) because these stars are thought to be more massive and have lower mass loss rates (more details are provided in Section 2.3). Although intrinsically bright, PISNe at sufficient distances are still undetectable. It is also possible that PISNe have been observed. For instance, as mentioned above, high-mass PISNe may be suitable for explaining some recent SLSNe whose nature is still under debate (see Section 2.4) and lower mass PISNe may be hiding among classes of normal SNe.

The question of the existence of PISNe is a very interesting one which is likely to be answered in the near future. The next generation of telescopes will be able to see back to the first generation of stars as well as monitor the transient sky more completely and frequently (see Section 2.5 for a discussion). Such a discovery of PISNe would not only be a valuable confirmation of stellar models, it would also have important implications for chemical enrichment, galaxy evolution, star formation, and cosmic reionization. Here, we study the explosive and observational properties of PISNe resulting from non-rotating very massive stars (VMS; defined by Vink [Vin14] as stars with initial masses exceeding 100 $M_{\odot}$) of intermediate metallicity ($Z = 0.001$ or $\sim 0.07\ Z_{\odot}$). The choice of simulating stellar evolution without rotation is motivated by the degeneracy in mass loss estimates between a star's initial metallicity and rotation rate. Both higher metallicity and higher rotation rate contribute to increased mass loss, therefore it is necessary to only tune one for our purposes. Since stars do rotate, however, our models represent stars of a range of metallicities depending on the actual rotation rates (where our choice of $Z = 0.001$ is the minimum). Such stars are may exist throughout a wide range of distances (soon to be probed by the next generation of telescopes) due to the fact that chemical enrichment (as shown by both models and observations) is patchy. More details on this point are discussed in Section 2.3.

We are interested in the properties of PISNe throughout their allowed mass range and choose four masses to sample this range. Our models, whose initial masses are given in the names, are P150, P175, P200, and P250. Their evolution is modeled with the `GENEC` code and is described in Section 3. Our models are some of the relatively few PISN models in the literature at such high metallicity (these include Langer et al. [Lan07], Chatzopoulos et al. [Cha14], Whalen et al. [Wha14b], and Chatzopoulos et al. [Cha15]) and the only such models computed with `GENEC` besides those in Whalen et al. [Wha14b]. We are interested in applying model predictions to interpret observations of SLSNe. For this purpose, our two more massive models (P200 and

P250) are most suitable. We are also interested in making predictions for the observational signatures of low-mass PISNe (P150 and P175) to be used for comparison with current and future observations. Therefore, we perform 1D explosion simulations for all four models using the multiphysics code FLASH. These calculations and their results are presented in Chapter 4.

We also concern ourselves with exploring chemical mixing in the SN ejecta. One motivator for this endeavor is the possible connection between PISNe and SLSNe (see Section 2.4). PISNe had been explored by a few groups in 2D [Che11; Jog11; Cha14; Che14a; Che15a], but not in 3D (except by Chen et al. [Che11], but no 3D results were published). In 2D, simulations have found fluid instabilities driven by the explosive burning (at the upper and lower boundaries of the oxygen shell). They also find reverse shocks that lead to Rayleigh-Taylor (RT) instabilities either from the shock wave crossing into a hydrogen envelope or breaking out of the stellar surface (more details are given in Section 2.6). In particular, Chen et al. [Che14a] found that non-zero metallicity models, having lost their hydrogen envelopes, did not allow enough time for fluid instabilities to grow sufficiently to affect observations. We wanted to know how the picture would change in 3D. To this end, we present the first published 3D simulations of PISN explosions and compare to the corresponding 1D results. For our most massive model, P250, we present 1D, 2D, and 3D models of higher resolution. We compare the results finding enhanced mixing with increased dimensionality, especially near the silicon-oxygen (Si-O) interface. All multidimensional simulations and results are presented in Chapter 5.

Our exploration into the observational properties of our explosion models is presented in Chapter 6. This includes calculations of bolometric and broad-band LCs using the radiation-hydrodynamics code STELLA (see Section 6.2). We do this for all 1D explosion models and for the high resolution 1D and 3D explosion models. We compare our P200 and P250 results to observations of SLSN PTF12dam. As a further application of our explosion results, we compute the neutrino emission and oscillations for our most and least massive models (P150 and P250). We make predictions for what current and future neutrino detectors will see for such PISNe occurring at a distance of 10 kpc. These calculations and their results are presented in Section 6.3. Lastly, we describe a project with the goal of computing spectra from the 3D PISN explosion models, as the effects of mixing between the silicon and oxygen-rich layers of the ejecta (our main finding from our multidimensional study) are likely to affect the formation and evolution of certain spectral lines. The goals and some initial results for this project are described in Section 6.4.

Finally, we summarize our work and findings in Chapter 7. We close with a discussion of the implications of our results and the next steps for research.

CHAPTER

2

BACKGROUND

2.1 Introduction

In this Chapter, we provide context for the results to follow with relevant background information. We begin by describing the characteristics of the evolution of VMS and their fate in Section 2.2. Then, we discuss the prevalence of VMS throughout the history of the universe in Section 2.3. These sections will give some idea of the likelihood that stars reach the conditions necessary to trigger PISNe. Then, in Section 2.4, we discuss the new transient class SLSNe and its possible connection to PISNe. We complement this discussion with a look towards future observations in Section 2.5. Next, to give context for our multidimensional study that will be presented in Chapter 5, we summarize the findings of previous 2D simulations of PISNe in Section 2.6. Finally, we conclude this Chapter by summarizing the key points in Section 2.7.

2.2 Very Massive Stars

As mentioned in Chapter 1, VMS are defined as stars with initial masses exceeding 100 $Z_{\odot}$ [Vin14]. Thus, stars that will explode as PISNe all belong to this category (actually there are exceptions for rapid rotators as described in Section 6.3). Initial mass is the single most important initial condition for determining the evolution and outcome of a star. Stars like the Sun will never

reach the core conditions necessary to support the fusion of elements heavier than helium. Conversely, stars of 8 $M_\odot$ will proceed to fuse elements until an iron core is formed before dying as a CCSN. Thus, it is no surprise that the evolution of VMS differs considerably from that of regular massive stars, however unlike for regular massive stars, the evolution of VMS is largely unconstrained by observations.

Instead, most of what we know about them comes from modeling. One major difference is that VMS evolve much more quickly than lower mass stars (a 100 $M_\odot$ lives for $\sim$3 Myr whereas a 10 $M_\odot$ lives for $\sim$20 Myr and a 1 $M_\odot$ lives for $\sim$10 Gyr). This can be understood by the fact that, although more massive stars have more fuel to burn, their luminosities (which reflect their energy generation rates) are much higher. Thus, extremely high luminosities are a second main characteristic of VMS. Related to high luminosities are high effective temperatures, which means VMS emit more high frequency radiation. Because of this property, VMS may have been important in ionizing the interstellar medium during the epoch of reionization [see Vin14, and references therein].

Another prediction from models is that VMS have large convective cores, causing chemical homogeneity, throughout most of their evolution [Hir15]. In this sense, they are simpler than regular massive stars, where the size of the convective core depends on rotation and magnetic fields. Instead, the most uncertain ingredient in VMS evolution models is mass loss. In general, they are characterized by stronger mass loss than lower-mass stars, especially at high metallicities (metals have complex level-structures which cause high opacities). Because of this, many VMS models predict Wolf-Rayet stages following the stripping of hydrogen envelopes. The uncertainties in the current mass loss rates boil down to the prediction that VMS at solar metallicity cannot retain enough mass to explode as PISNe, while VMS of slightly lower metallicity (as in the Magellanic Clouds) may or may not [Hir15].

Finally, one of the most important predictions one can make from a stellar model is the mode of death. Models of stars that produce sufficiently large CO cores encounter the PI because their cores reach a certain region in T_c-ρ_c space. Stars that explode as CCSNe bypass this region because they reach the required temperatures at higher densities (see Figure 1 in Waldman [Wal08]). Still, reaching the PI is not enough for a full-fledged PISNe. The contraction must be strong enough to release enough nuclear energy to exceed the gravitational binding energy of the star, otherwise the entire star cannot become unbound and the result is a PPISN. A strong enough contraction is only achieved if the CO core is sufficiently massive. For overly massive CO cores, the contraction is even stronger which the core to become unstable to photodisintegration. The result in this case is a very large black hole.

2.3 The Prevalence of Very Massive Stars At Low and High Redshift

The prevalence of PISNe hinges on the prevalence of VMS, which is unknown, and especially so for the distant (early) universe. It is well known that star formation approximately follows what is called the initial mass function (IMF) that describes the distribution of newly-formed stars as a function of their initial masses. It is characterized by a power-law dependence of the number of stars at a given mass on that given mass. Salpeter [Sal55], who introduced the idea, found empirically a value of -2.35 for the power-law exponent (termed α). The IMF has since been amended (particularly at the low-mass end) but this value for α has hardly changed for local observations. It is natural to suspect that α may depend on the star formation environment, however. In fact, recent observational evidence suggests that this is the case.

Recent observations have been reported indicating top-heavy IMFs (those with a shallower power-law slope and thus higher probabilities for producing PISN progenitors) in nearby star clusters. For example, the Arches cluster (only ~ 100 light years from the galactic center) was recently measured to have a power-law slope of $\alpha = -1.92^{+0.23}_{-0.12}$ by Hosek et al. [Hos18]. The cluster is so dense in its core that the inner 0.25 pc could not be probed. This coupled with the fact that high-mass stars are preferentially located closer to the cluster's center of mass, suggests an even shallower slope. Schneider et al. [Sch18] find a similar value for α ($-1.90^{+0.26}_{-0.37}$) for the star-forming region, 30 Doradus, located in one of the Milky Way's satellite dwarf galaxies, the Large Magellanic Cloud. The deviations from the value from Salpeter [Sal55] may be due to (for the Arches cluster) the proximity to the galactic center or (for 30 Doradus) the low metallicity of the galaxy ($0.43 Z_\odot$ [Cho16]). It is nonetheless expected that the first generation of stars had a more top-heavy IMF whose slope has slowly steepened following the chemical enrichment of the universe.

This presumption stems from the fact that metals have more complex atomic level-structures and therefore more readily absorb radiation. This is the same idea that is behind the increased mass loss for stars of higher metallicity. In fact, many recent numerical simulations agree that the Pop III (the population of the first generation of metal-free stars) IMF is dominated by stars around 100 $M_\odot$ [Abe02; Bro04; Yos08]. However, some very recent simulations find that fragmentation may lead to stellar populations that extend below even 1 $M_\odot$ [Sta14; Sta16] which means VMS would be significantly less abundant than previously thought. Additionally, it is unclear how massive an individual Pop III star can get. The maximum mass may be limited by ionization feedback [Kru14]. However, if the maximum mass is as high as it appears to be in the local Universe (see the discussion on nearby VMS in Section 6.3), then VMS are likely to also

form in the early Universe. Furthermore, such stars would experience lower mass-loss rates due to the absence of metals in their atmospheres, allowing them to retain enough mass to explode as PISNe. There is also theoretical evidence that suggests pockets of pristine star-forming gas exist even at relatively low redshift ($2 < z < 5$) [Tor07] which increases the prospects of PISN progenitor stars existing in the local universe. So, while PISNe are expected to be more common for zero-metallicity stars in the early universe, they likely also occur for higher metallicities at distances which are more easily probed.

2.4 Pair-Instability Supernova Candidates Among Superluminous Supernovae

Much of the recent interest in PISNe can be attributed to the relatively new class of transient, SLSNe. SLSNe are defined as any SN with a peak absolute magnitude brighter than -21 [Gal12]. This roughly corresponds to 7×10^{43} erg s^{-1} which is ~ 10 times higher than the peak luminosity of a normal CCSN. SLSNe are classified as either SLSN-I (for events without hydrogen) or SLSN-II (for events with hydrogen) just as in the classification scheme for normal SNe. As is the case for normal SNe, SLSNe display a large amount of diversity within the two main types (which seems to suggest that more than one mechanism may be responsible, as is the case for normal SNe). Such high peak luminosities can easily be reached in model light curves (LCs) of high-mass PISNe due to their high ejecta masses of ^{56}Ni (which can approach 55 $M_\odot$ [Heg02]). However, PISNe are not the only model that can produce such high peak luminosities. The circum-stellar interaction between SN ejecta and previously ejected shells of material can also produce such luminosities and has been explored by Tolstov et al. [Tol17] and Wheeler et al. [Whe17], among others. The magnetar (a rapidly-rotating and highly-magnetized neutron star) model, whose power source is electromagnetic dipole radiation from the spin-down of a newly-born magnetar, has been very successful in reproducing observational features of SLSNe and has significantly grown in popularity during recent years [Des12; Nic17; Des18]. One interesting thing to note is that, for some SLSNe, it is likely that two or even three (as argued in Wang et al. [Wan16]) of these energy sources is at work. A review of the observational properties and proposed models can be found in Moriya et al. [Mor18]. While it is interesting and important to note that a debate is ongoing and alternative models to the PISN model exist, we will focus on the viability of purely Ni-powered PISN models for SLSNe here. Besides extremely high peak luminosities, there are other discriminators in observations that give a PISN interpretation considerable difficulties.

One of the simplest discriminators is the post-peak decline rate of the bolometric LC. Any

supernova light curve whose main power source is the radioactive decay of ^{56}Ni will exhibit a post-peak decline rate commensurate with the half-life of ^{56}Co (the second nuclide in the decay chain (^{56}Ni $\rightarrow$ ^{56}Co $\rightarrow$ ^{56}Fe)). Another relatively simple discriminator is the time the LC takes from the onset of the SN to rise to peak luminosity (the rise time or t_{rise}). This is somewhat complicated by the fact that the rise time is almost never precisely known for an observed SN as well as the fact that certain model uncertainties contribute to predicted rise times for PISNe. A third, and more complicated, discriminator comes from the fact that the observed SLSNe are relatively nearby (therefore the progenitors were enhanced with metals from birth). Stellar evolution models invariably predict higher mass-loss rates for higher ZAMS masses and for higher initial metallicity (Z), but the specifics remain very uncertain. Therefore, if a nearby star has a high enough ZAMS mass to eventually explode as a PISN, it probably loses its hydrogen envelope via stellar winds long before it explodes. Combining these three discriminators it is clear that the PISN model is most well-suited to explain the slowest evolving SLSNe-I that exhibit post-peak decline rates consistent with the radioactive decay of ^{56}Ni [Ins17; Jer17]. However, even for events that fit all the previously mentioned discriminators, still more discriminators related to the spectral character and evolution pose problems for PISN models to address.

To illustrate more clearly the problem, it is useful to examine some examples of SLSNe for which PISN interpretations have been proposed. Gal-Yam et al. [Gal09] was the first to propose a PISN explanation for such a SLSN, namely SN 2007bi (although Woosley et al. [Woo07] had, a few years prior, made the case that SN 2006gy was produced by circumstellar interaction with shells originating from the pulsational PI). SN 2007bi was discovered in a relatively nearby dwarf galaxy ($z = 0.1279$) and its spectra exhibited no signs pointing to the presence of either hydrogen or helium. Therefore it is an example of a SLSN-I. The peak luminosity and post-peak decline rate were consistent with the LC being powered by the ejection of > 3 $M_{\odot}$ of ^{56}Ni. However, this SN was discovered after peak luminosity, which means the first observation gave a lower limit to the actual peak luminosity and the rise time was totally unconstrained. The PISN interpretation of SN 2007bi was both supported [Kas11; Koz14b] and critiqued [Des12; Des13; Cha15; Jer16] by subsequent works. PISN models were able to sufficiently match key observables such as the bolometric LC and photospheric velocity, but they were not able to explain the blue nebular (late-time) spectra of SN 2007bi.

More recently, SLSN PTF12dam has captured the interest of PISN enthusiasts. SLSN PTF12dam, also apparently devoid of hydrogen and helium, has late-time [Nic13] and host galaxy [Che15b] properties that are very similar to those of SN 2007bi but, unlike SN 2007bi, it was caught before peak luminosity [Qui12]. The relatively fast rise to peak luminosity together with the spectral evolution over this period pose serious problems for PISN models [Nic13]. However,

as will be discussed in Section 6.2, our models predict faster-rising LCs and bluer colors than other models in the literature, therefore providing a better match to the observations of SLSN PTF12dam.

2.5 Observational Prospects for PISNe

Just as the last generation of surveys gave rise to the exciting class of exotic transients (SLSNe), we can expect more surprises in the coming decades. However, we can certainly expect more SLSN events like those described in the previous section. It is also reasonable to suspect that observations of PISNe will become common when new survey telescopes like the Large Synoptic Survey Telescope (LSST), the Wide-Field Infrared Survey Telescope (WFIRST), and the Wide-Field Imaging Surveyor for High-Redshift (WISH) see first light. These telescopes will provide an unprecedented time-dependent view of the sky out to large redshift. Whalen et al. [Wha13] use PISN rate calculations to estimate that WISH and WFIRST may observe up to ~ 1000 PISNe per year in the redshift range ($15 < z < 20$). Whalen et al. [Wha13] also estimate that for the redshift range ($5 < z < 10$), where PISNe would be visible to LSST, a similar rate is expected.

More exciting prospects will come with the launching of the the James Webb Space Telescope (JWST), the successor to the Hubble Space Telescope (HST). Although its field of view is significantly smaller than the aforementioned survey telescopes, JWST will be able to see back to the first generation of stars and galaxies. JWST will be sensitive to PISNe out to $z \gtrsim 30$ and can expect 5-10 primordial PISNe over its lifetime [Wha13]. One proposed survey may be able to increase this prospect, however. It is being proposed by the First Light At REionization project [Wan17]. They describe a plan that optimizes the surveying capabilities of JWST with the goal of detecting the first SNe, thereby placing constraints on the "truly initial" IMF.

2.6 Pair-Instability Supernova Simulations in 2D

One of the first studies of PISNe in 2D was done by Joggerst & Whalen [Jog11] with the CASTRO code [Alm10]. Their findings were very different from those in a previous paper [Jog10] which used a similar method to explore mixing in primordial CCSNe. Where with CCSNe vigorous mixing resulted in the explosion, the PISNe exhibited minimal mixing for most of the models studied. For those that did exhibit mixing, it was confined to the oxygen-rich layer of the ejecta and driven by a reverse shock. The strength of this reverse shock, and that of the resultant mixing, depended positively on the pre-explosion convective mixing between the hydrogen and helium envelopes. Their method, however, involved simulating the contraction and explosion

in 1D and then switching to 2D after burning had ceased. Therefore, their approach could not capture instabilities that might be seeded by the contraction and explosive burning.

Also using CASTRO, Chen et al. [Che14a] simulated primordial PISNe beginning at the onset of core contraction. They found that the oxygen and helium burning drove fluid instability growth during expansion at the lower and upper boundaries, respectively, of the unburnt oxygen shell. Similarly to Joggerst & Whalen [Jog11], Chen et al. [Che14a] found RT instability growth due to formation of a reverse shock when the forward shock reaches the hydrogen envelope, but only for their red supergiant model. Their blue supergiant model, which was considerably less extended in radius, experienced no such growth due to a weaker reverse shock. Similarly, a non-zero metallicity model in Chen et al. [Che15a], had lost its entire hydrogen envelope and thus was not able to form a reverse shock at all.

Finally, we note that Chatzopoulos et al. [Cha14] performed "2.5-D" simulations of PISNE in which rotational effects were included during the contraction and explosion phases. The inclusion of rotation exacerbated the asymmetries caused by fluid instabilities and even affected the yields of ^{56}Ni. While these results are interesting and should be kept in mind, we choose not to complicate our study with rotational effects so we can focus on the effects of 3D versus 2D.

2.7 Conclusion

In this Chapter, we have provided the basic conditions required for PISNe, and discussed why these conditions result in such an event. We then outlined the current knowledge pertaining to the formation of VMS and applied the dependence of their evolution on metallicity and what is known about chemical evolution towards a general picture of their prevalence throughout cosmic time. This will be important to keep in mind for the discussion on observational signatures of PISNe in Chapter 6. Then, we discussed the possibility that PISNe have already been seen and are explanations for some SLSNe, citing two main candidate events (SN 2007bi and PTF12dam). We then previewed the prospects of PISN detection for upcoming telescopes. Finally, we summarized the findings of previous studies of PISNe in 2D. We conclude that, given the current state of the field, it is possible that PISNe exist in both the local and distant universe. Given this possibility, and the expectation of more observational events, it is important to further explore the possible connection of PISNe to SLSNe. Furthermore, since it is unknown whether 3D simulations will affect model predictions of observational characteristics, it is important to also explore this question.

CHAPTER

3

PROGENITOR MODELS

3.1 Introduction

In this Chapter, we present the stellar evolution calculations and results that yielded the four VMS models (P150, P175, P200, and P250) used for our study. As discussed in Section 2.2, mass loss is a driving force in the evolution of VMS. Therefore, we pay close attention to this aspect in what follows. We also note that many of the PISN models in the literature are initialized as helium cores and are evolved without mass loss [Heg02; Kas11; Jer16]. Although uncertain, the inclusion of mass loss, especially for non-zero metallicity stars, results in more realistic observational properties. While many other PISN simulations use progenitors evolved beginning from the main sequence and with the inclusion of mass loss [Des13; Wha13; Koz14a; Cha15], only Whalen et al. [Wha14b] use `GENEC` progenitors.

3.2 Methods

To compute our PISN progenitors, we use the `GENEC` code [Eks12] and employ the same input physics as in Yusof et al. [Yus13]. One distinguishing characteristic of the `GENEC` code is its envelope treatment for massive stars which accounts for turbulent pressure and acoustic flux (see Ekström et al. [Eks12] for a complete code description). `GENEC` has adaptive resolution

in both space and time. These resolutions adapt to resolve important quantities such as temperature and hydrogen abundance. ~ 200 spatial zones are used during the main sequence and $\sim 300-800$ zones are used during the later, and more complex, phases of stellar evolution. The number of zones also strongly depends on the radial extent of the model (in our case this decreases with increasing ZAMS mass). After somewhere between 27,000 and 30,000 time steps, all models reached the stage at which the PI begins to develop (actual ages of $\lesssim 3$ Myr).

We treat mass loss by employing different mass loss prescriptions depending on the evolutionary phase (which is determined by the effective temperature and surface composition). We apply dependence on the initial metallicity to the prescription rates using the formula: $\dot{M}(Z) = \dot{M}(Z_{\odot}) \times (Z/Z_{\odot})^{\alpha}$, where α is also dependent on the evolutionary phase. The details including choices of temperature and surface composition cutoffs and the citations for the prescriptions can be found in Gilmer et al. [Gil17]. The models all enter Wolf-Rayet phases (of varying types) due to stripping of the outer layers.

3.3 Results

We present the final pre-SN characteristics of our four models in Table 3.1. As described in Section 1, the initial masses (given in the model names) effectively span the PISN mass range. All models are non-rotating and have initial metallicity Z = 0.001 (or ~ 0.07 $Z_{\odot}$). More importantly, the CO core masses span the PISN CO core mass range of 64 $M_{\odot} \lesssim M_{CO} \lesssim 133$ $M_{\odot}$ which is an excellent predictor of the explosion strength. The structural evolution is shown for all the models in Figure 3.1. From the figure it is clear that all four models maintain a very large convective core for the vast majority of their lives. Figure 3.2 shows the model tracks on the Hertzsprung-Russel (HR) diagram which reveals that the luminosities are all very high throughout the entire evolution of the models. These two characteristics are commensurate with expectations for VMS and are two contributing factors to the very high mass loss rates that the models exhibit. Figure 3.3 shows the time evolution of the mass loss rate (left) and the Eddington parameter (right), $\Gamma_{Edd} = L/L_{Edd} = \kappa L/(4\pi c G M)$, for each model. The peak mass loss rate approaches 10^{-1} solar masses per year and occurs at a time corresponding to when the models first reach T_{eff} of $\sim 10^4$ K. The sharp changes in the mass loss rate are indicative of times at which the mass loss prescription was switched. Towards the end of evolution of P150, there are many up and down oscillations due to feedback from the mass loss rate on the effective temperature which leads to a repetitious cycling between prescriptions.

Due to the strong mass loss, P250, in addition to losing its hydrogen-rich envelope, also lost most of its helium envelope. Therefore, it ends up being very similar to more metal-rich models computed in Yusof et al. [Yus13]. The absence of an extended envelope in this model

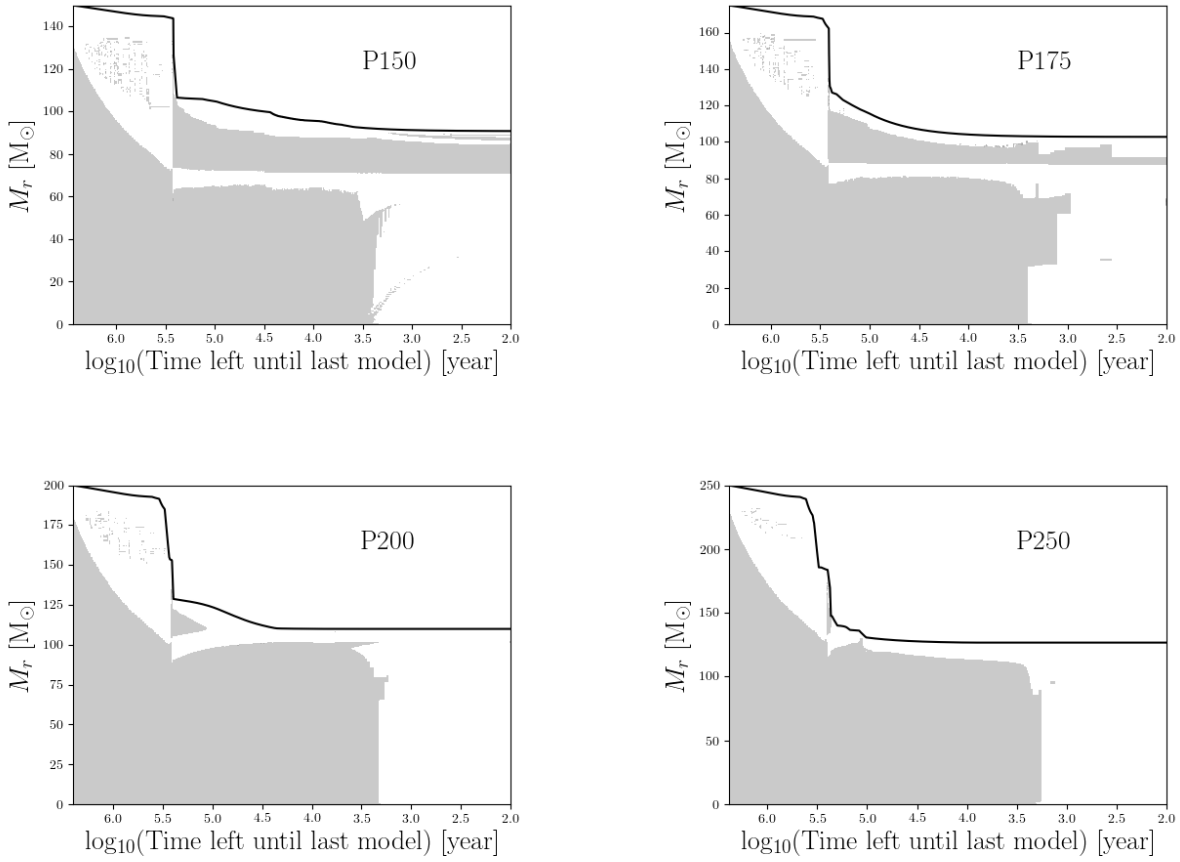

Figure 3.1 Structure evolution diagram for the VMS models as a function of the log of the time left until the last last time step. The gray zones represent the convective regions. The top solid line corresponds to the total mass.

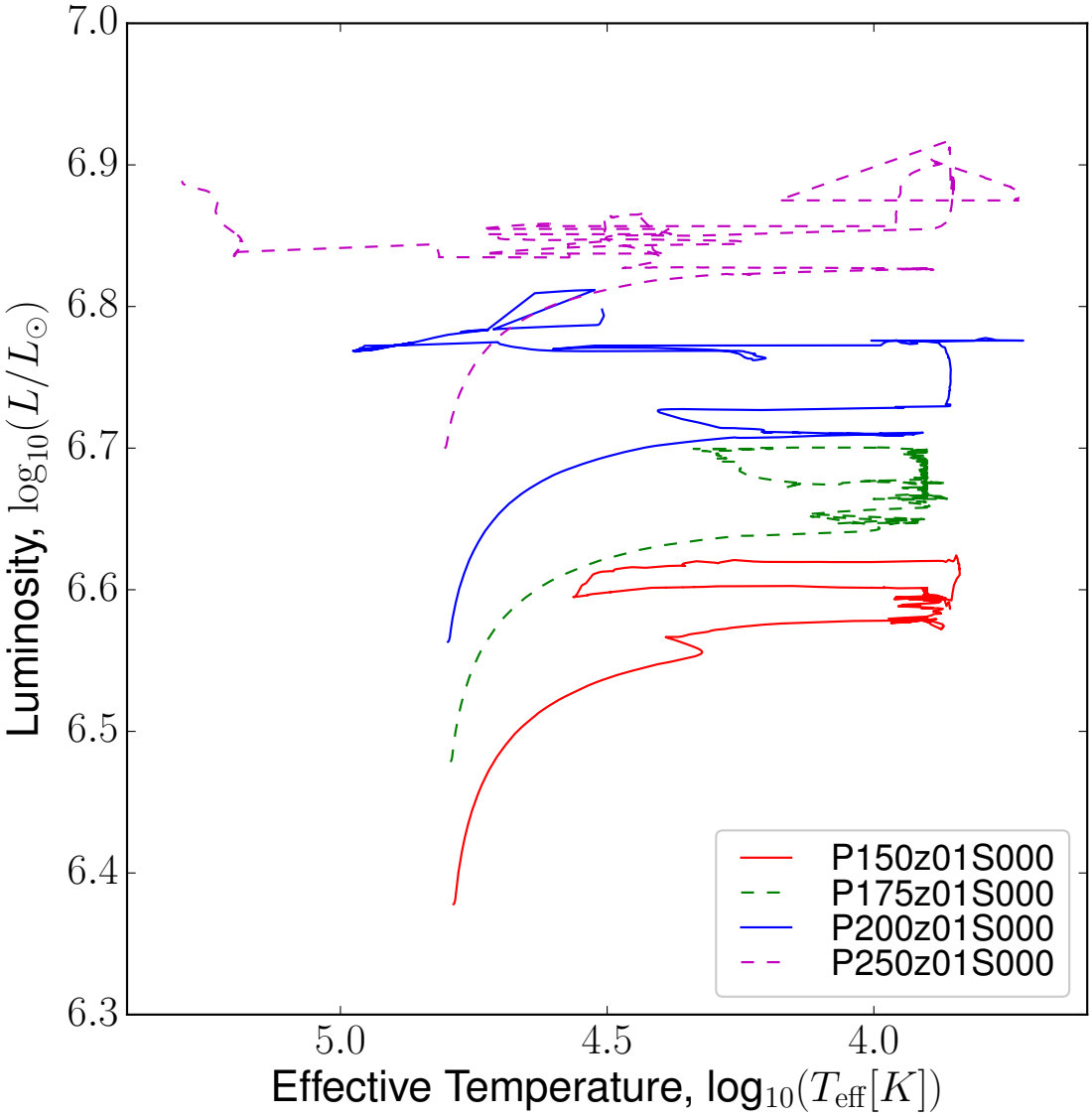

Figure 3.2 Evolutionary tracks in the HR diagram.

Table 3.1 Pre-SN properties for models P150, P175, P200, and P250. The CO mass core is defined as the mass coordinate at which the sum of the carbon and oxygen mass fractions falls below 0.5. The surface composition is quoted by mass.

Model	$M_{\rm tot}$ ($M_\odot$)	$M_{\rm CO}$ ($M_\odot$)	Radius ($R_\odot$)	Surface Composition
P150	90.8	65.7	1267	20% H; 80% He
P175	102.8	81.4	1107	18% H; 82% He
P200	109.9	100.9	80.1	6% H; 94% He
P250	126.7	126.7	2.4	34% He; 39% C; 27% O

will likely result in a LC with a short rise time, making it a good candidate for explaining some of the slowest-rising SLSNe [Koz17]. The lower mass models, which experienced less strong mass loss (due to their lower luminosities), all retain some hydrogen in their outer layers. Thus, they finish their evolution with cooler effective temperatures and larger radii. These models are more similar to VMS models of zero or very low metallicity [see Hir07; Eks08; Yos11; Yoo12; Cha12, and references therein]. We stress that mass loss prescriptions for VMS are uncertain, however. Finally, we did not apply enhanced mass loss for $\Gamma_{Edd} \geq 0.7$ as suggested by Gräfener et al. [Grä11]. The time evolution of the Eddington parameter is plotted on the right side of Figure 3.3. For all our models, $\Gamma_{\rm Edd}$ is low initially and rises (from ~ 0.5 to ~ 0.7) before the sharp peak, which coincides with the peak in mass loss rates. At this point, the Eddington factors for all models exceed 0.7, and for P250 it approaches the Eddington limit ($\Gamma_{\rm Edd} = 1$). Therefore, enhanced mass loss would have come into play and may have resulted in the stripping of all hydrogen for all models. For more details on mass loss in VMS, and VMS in general, see the recent book on VMS by Vink [Vin15].

We present the evolution of the central density and temperature for the models in Figure 3.4. The end of the tracks correspond to the final evolutionary states of the models before being mapped into `FLASH`. Note that the central region does not quite reach the PI region, but at these times a region of the core offset from the center occupies the unstable region (see Figure 4.2 in Section 4.2).

3.4 Conclusion

We have modeled the evolution of four PISN progenitors whose final CO core masses effectively span the target range of 64 $M_\odot \lesssim M_{\rm CO} \lesssim$ 133 $M_\odot$. As expected, the models evolve chemically homogeneously throughout most of their lives due to large convective cores. We discussed the implications of uncertain mass loss rates and how differing treatment may have affected

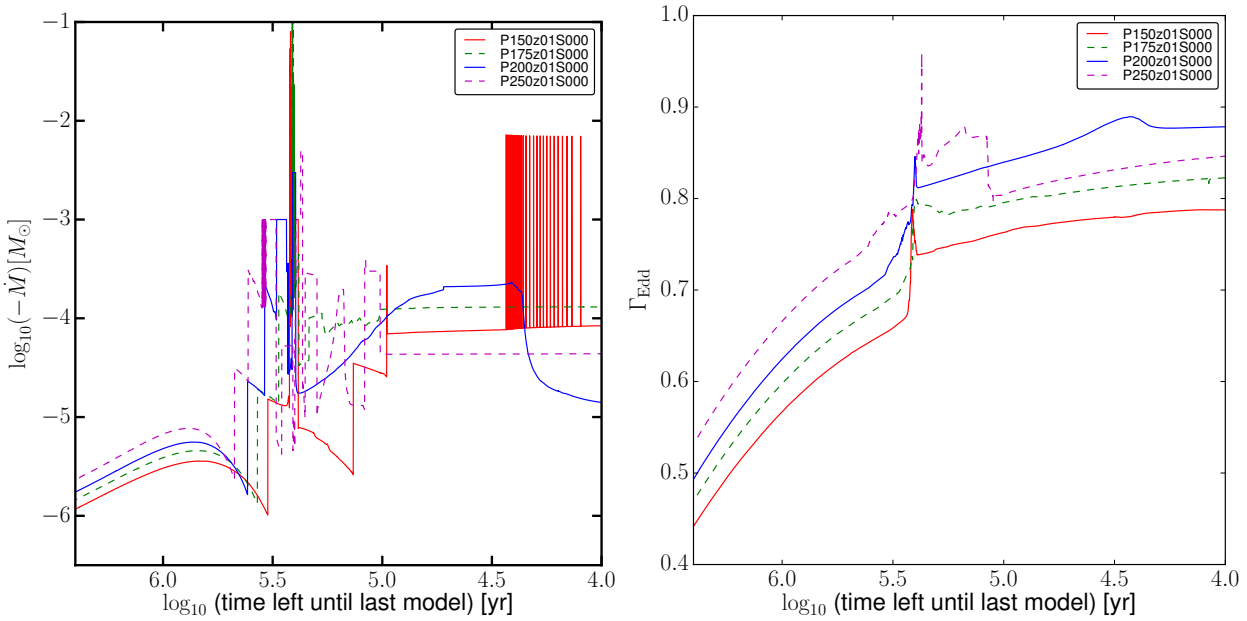

Figure 3.3 *L*eft: Evolution of the mass loss rate as a function of time left until last model (log scale) for the four VMS models. *R*ight: Evolution of the Eddington parameter, Γ_{edd}. These plots are zooming in the early stages where most of the mass loss occurs. The curves do not change significantly between $\log_{10}$(time left)= 4 and the end of the evolution.

our models. The models all approach the PI region in T_c-ρ_c space, as their masses predict. Finally, the models finish with relatively shallow envelopes. P250, which is basically just a very massive CO core, is $\sim$ 100 times more compact than 250M (a model from Kozyreva et al. [Koz14a; Koz14b] of the same initial mass and metallicity). The most similar models in the literature are the other GENEC PISN progenitors of Whalen et al. [Wha13]. However, P250 is more compact than their similarly massive bare helium core, h200. The effects that these envelope properties may have on observations will be interesting to explore.

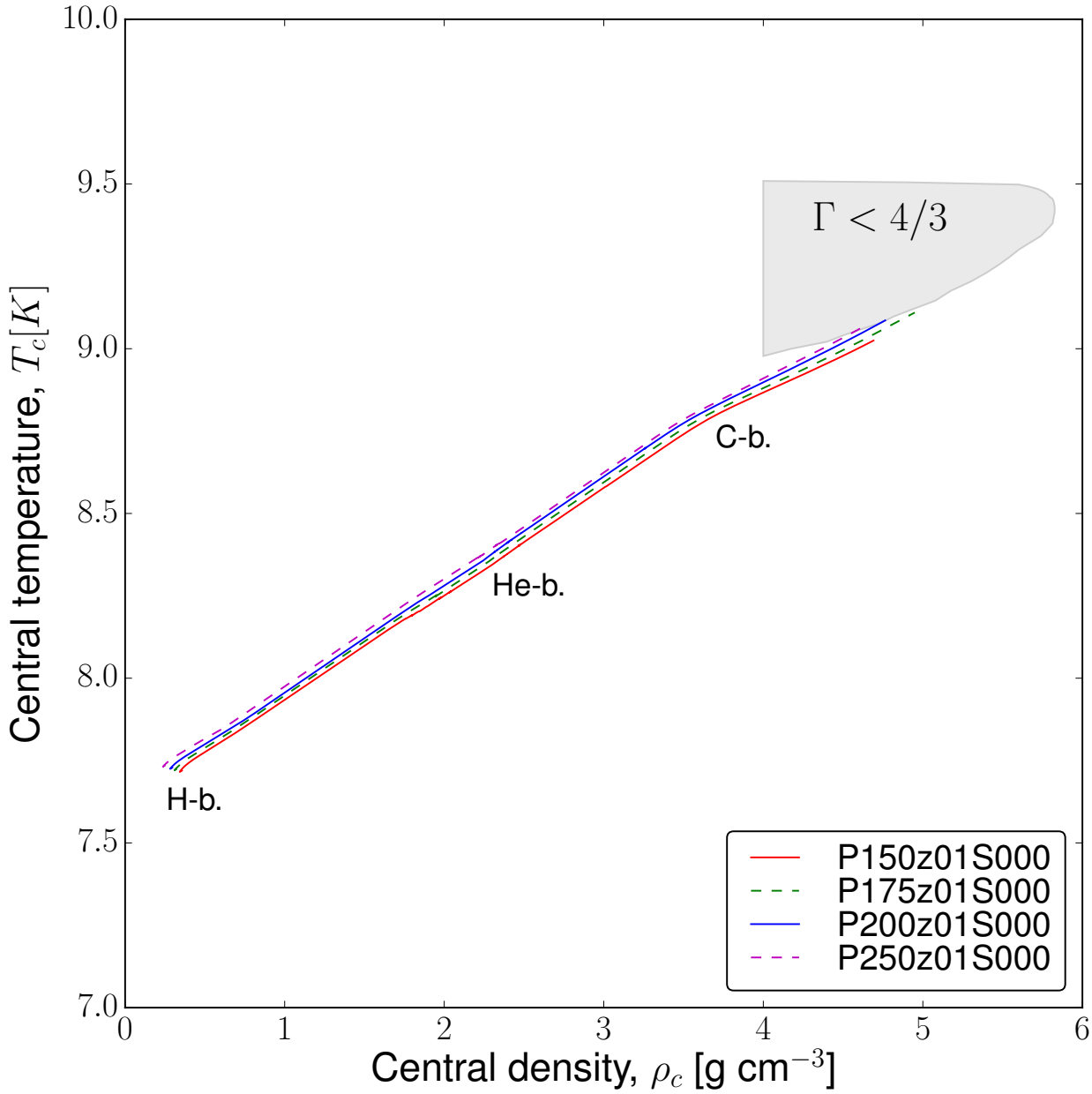

Figure 3.4 Evolution of the central temperature T_c versus central density ρ_c for the VMS models. The gray shaded area is the PI region ($\Gamma < 4/3$, where Γ is the adiabatic index).

CHAPTER

4

PAIR-INSTABILITY SUPERNOVA EXPLOSIONS IN 1D

4.1 Introduction

In this chapter, I will describe the one-dimensional explosion simulations that use as inputs the VMS models that were the subject of the previous chapter. The purpose of this study is to learn how the bulk explosion properties (including the main isotopic yields and explosion energies) change throughout the PISN mass range for such intermediate metallicity models ($Z = 0.001$). We will compare these findings to others from the literature. This knowledge will serve as a basis for further study on explosions in multi-D (presented in Chapter 5) and the observational signatures of PISN explosions (presented in Chapter 6).

4.2 Methods

To simulate the contraction and explosion phases of PISNe, we use the hydrodynamics code `FLASH` (version 4.3; Fryxell et al. [Fry00] and Dubey et al. [Dub09]). We map the stellar cores from the models described in Table 3.1 during core carbon burning, which corresponds to the end of the evolutionary tracks shown in Figure 3.4. The precise choice of evolutionary stage

for the mapping is critical to generating an explosion with minimum error in stellar evolution. GENEC does not include the contribution to the pressure from electron-positron pairs so the mapping must be done before this contribution becomes too great. Conversely, FLASH is not a stellar evolution code so the input model must be sufficiently evolved for the final contraction to occur. We were able to achieve the latter condition in FLASH for model time steps in which the initial pair pressure (in the worst case) barely exceeded 1% of the total pressure in the core (see Figure 4.1).

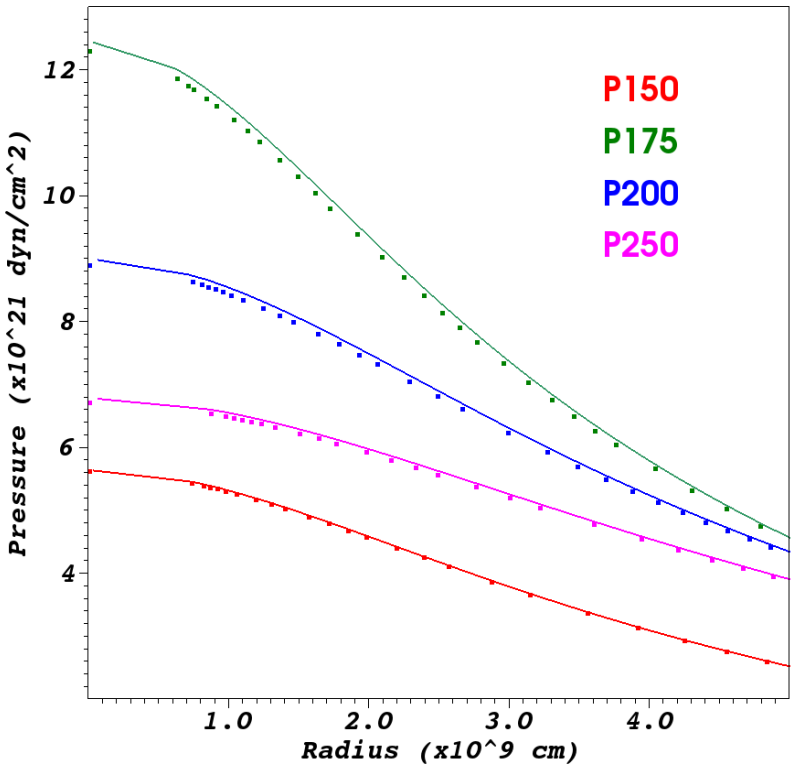

Figure 4.1 The pressure profiles in the core of models P150, P175, P200, and P250 at the end of evolution with GENEC (points) and at the beginning of evolution with FLASH (lines).

Figure 4.2 shows the profiles of the adiabatic index for the GENEC model mapped into FLASH. As seen in Figure 4.2, the instability develops first off-center and not in the very center. This is due to neutrino cooling being stronger in the very center during the contraction of the core after helium burning. With the exception of P150, the mapping to FLASH was done at the point during core carbon burning at which the cores have become slightly unstable due

to the PI. P150 constitutes a special case in which the GENEC model crashed before reaching the instability (see Figure 4.2). The difficulty in evolving this particular model is due to the envelope of the model expanding to large radii following the core contraction at the end of core helium burning, where as the more massive models (with little or no hydrogen-rich envelope) remain compact at the end of their evolution.

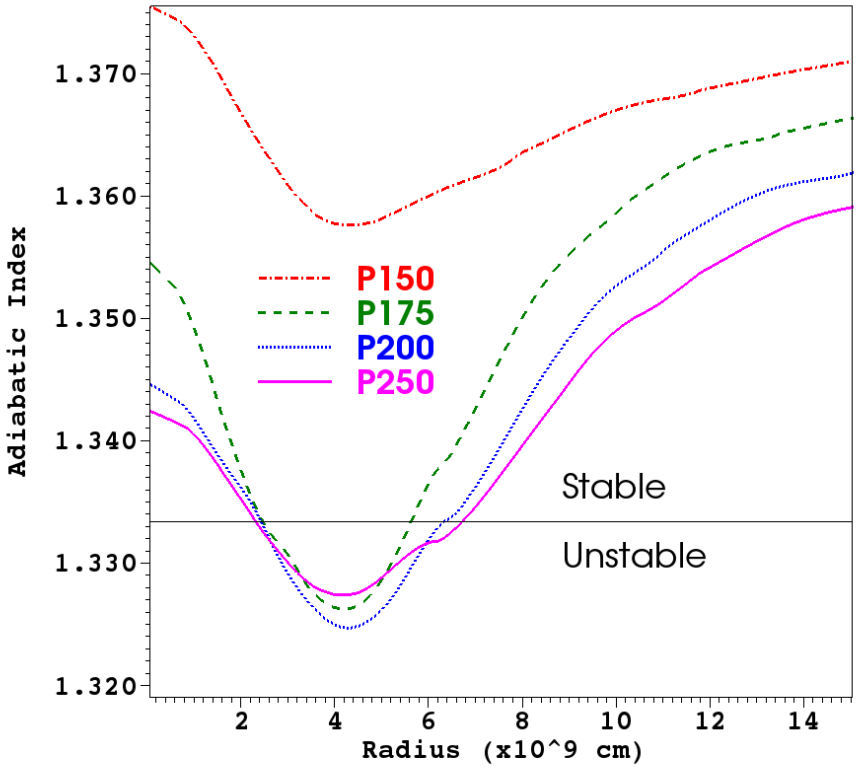

Figure 4.2 The adiabatic index in the core of models P150, P175, P200, and P250 at the time of mapping from GENEC to FLASH.

For models P175, P200, and P250, only the inner 'cores' of radii 3.334×10^{10} cm (P175), 4.167×10^{10} cm (P200), and 5.000×10^{10} cm (P250) respectively, comprising the CO cores plus small parts of the envelopes, were mapped into FLASH. For brevity, we will call these inner spheres the 'cores'. The radii of the 'cores' ($R_{\rm core}$) were chosen so that the ratio $R_{\rm core}/R_{\rm CO}$ was about 1.3. We mapped the initial models using the same scheme as in Chatzopoulos et al. [Cha15] which involves a parabolic interpolation of the model data onto an initially uniform grid.

We use the new directionally-unsplit hydrodynamics solver (Lee & Deane 2009) included in FLASH. The fact that the solver is directionally-unsplit is, of course, irrelevant for 1D simulations but there are other characteristics of the solver that are important here. The solution accuracy, in both space and time, is second-order for smooth flows and first-order for shock flows. The solver has many options for numerical implementations which are set using various runtime parameters. We employ the third-order spatially accurate piece-wise parabolic method (PPM) for data reconstruction in the normal direction. We use the HLL (Harten, Lax, van Leer) Riemann solver and the minmod slope limiter which are suitable for supernova hydrodynamics. We also include artificial viscosity with the default coefficient to improve numerical stability near discontinuities.

We couple the hydrodynamics with the Aprox19 nuclear burning network [Tim00] (also included in FLASH). The Aprox19 network follows nineteen nuclear species including all the alpha nuclei up to Nickel-56, Helium-3, Nitrogen-14, Iron-54, as well as free protons and neutrons. This is sufficient for accurately computing the energy added due to nuclear burning and the bulk nucleosynthetic yields. Detailed nucleosynthesis would require a much larger network (about 100 isotopes) and could be computed as a post-processing step from thermodynamic trajectories of passive tracer particles.

We employ the Helmholtz equation of state (EOS) [Tim00], also included in FLASH, which is needed to accurately model the mildly relativistic and degenerate electrons and positrons, which are treated as a non-interacting Fermi gas. This EOS also includes radiative effects which are necessary since radiation is the dominant component of the pressure at this stage of evolution. A blackbody spectrum is assumed as well as local thermodynamic equilibrium. The nuclei are treated as an ideal gas with $\gamma = 5/3$.

Self-gravity was computed with the new Multipole solver in FLASH [Cou13]. The new solver makes two main improvements over previous solvers. The first alleviates the error that comes from calculating the gravitational potential at the same point where mass is effectively situated, that is, at the center of the computational cell. The new solver computes potentials at cell faces in order to avoid convergence failures. The second improvement is the choice of the optimal expansion center, which is the square-density-weighted mean location. Such a choice reduces the multipole cutoff required for a given desired accuracy, thereby speeding up and/or reducing error in the calculation.

In general, the multipole expansion method of solving Poisson's equation is used for nearly-spherical mass distributions (including CCSNe). Thus, it is the natural to use such a solver for PISNe where, due to the smaller deviations from spherical symmetry, the monopole term is even more strongly dominant than in the CCSN case. Furthermore, while full or approximate general relativity can be important in CCSNe, but is still not always included due to the enormous

computational cost, the densities reached in PISNe are several orders of magnitude lower than those reached in CCSNe. Based on these two points, we are confident that handling self-gravity with this method approximates the effects to a high level of accuracy.

We use the block-structured grid implementation Paramesh4dev [Mac99] (which includes Adaptive Mesh Refinement; AMR). This implementation is a type of block-structured AMR where only blocks (sets of computational cells) can be refined/derefined. The blocks exist at different refinement levels on a tree data structure, where the root of the tree contains the largest blocks. After refinement, child blocks occupy together the space of their parent. Guard cell filling is done by copying information from neighboring blocks, or, in the case where the neighboring blocks are at lower/higher refinement levels, interpolation/averaging. When block edges coincide with domain boundaries, guard cells are filled using an external boundary routine. Blocks are marked for refinement/derefinement according to local gradients of user-specified refinement variables. Paramesh makes use of Löhner's error estimator [Löh87] for this task and the cutoff values for refinement/derefinement are user-specified.

The grids of our simulations were set to an initial minimum resolution of 1.3×10^8 cm with the freedom to refine once to 6.5×10^7 cm. We employ the 'reflect' ('diode') boundary condition for the inner (outer) boundary. The minimum resolution specified is higher than would normally be required for a PISN simulation. Here, however, we had noticed that mass would slowly flow in through the outer zone in FLASH during the time leading up to the collapse (even though the 'diode' boundary condition is meant to prevent this). Since we had to evolve the star in FLASH for a considerable amount of time before the final contraction occurred, a high minimum resolution was used to slow the spurious influx of matter through the outer boundary. This limited the total mass added during the simulation to only a few solar masses (which roughly translates to a few percent of the total mass) before the final contraction occurred.

The criteria for refinement were satisfied when temperature and/or gradients exceeded values that were proportional to the refinement cutoff parameters. These, as well as the derefinement cutoff parameters, were set to half of their default values in FLASH which allowed the maximum refinement level to be achieved in the inner cores during the explosive burning phase. This was important for determining the energetics and nucleosynthetic yields of the explosion. During explosive burning, the shock wave is launched from just outside the exploding core. The simulation is halted just before the shock wave exits the domain (at this point nuclear burning rates are negligible).

For model P150, we had to use a slightly different procedure due to the earlier evolutionary stage at the end of the GENEC simulations. We used the same resolution and refinement settings as we did for the rest of the models. The difference is an extra step in between the stellar evolution and the explosion simulation where we use FLASH, but with a different hydrodynamics

implementation, to prime the model for contraction. We took the final P150 time step from the stellar evolution (shown in Figure 4.2) and mapped the inner 1.67×10^{11} cm (including the carbon-oxygen core plus part of the helium shell) into FLASH to evolve towards the instability using the directionally-split hydrodynamics solver. This solver was better suited for the slow initial approach to the PI (and is actually the default hydro solver for this version of FLASH). We then re-mapped the unstable core into FLASH, this time evolving with the new unsplit hydrodynamics solver as for the other three models to follow the contraction and explosion. If the transition is made too early, the core will not contract. If the transition is made too late, the small numerical effects from switching solvers do not have time to dissipate before the contraction. Thus, we transition at the earliest time that yields a contraction and a subsequent explosion. This corresponds to a time when the minimum adiabatic index in the core is 1.302. The subsequent simulation then takes 650.1 s to reach maximum compression, allowing enough time for the core to relax out the numerical effects from the transition.

In order to gauge the effect on our results from using the directionally-split hydrodynamics solver, we perform simulations of all four models using this solver. Except for the choice of hydrodynamics solver, the simulations of the three more massive models are, identical in every way to those described above. For P150, we use only the directionally-split hydrodynamics solver, and hence do not have to perform the extra mapping step as before. We present the nickel and silicon yields (these are good indicators of all main results presented later) of these simulations alongside their unsplit hydrodynamics solver counterparts in Table 4.1. The table shows that the discrepancies in the yields between the two solvers increase with increasing initial mass (and also final mass). For the two lower mass models, P150 and P175, the results agree very well. This means that, in terms of the main results, the two solvers are nearly interchangeable at the low end of the PISN mass range. There is also the concern of the additional mapping step required for model P150. Here, the uncertainties are more difficult to gauge. However, we stress that the carbon-oxygen core, the mass of which is an excellent predictor of the explosion properties, was fully formed during the stellar evolution with GENEC. In addition, the contraction and explosion phases were fully simulated using the unsplit hydrodynamics solver, which is consistent with the three more massive models.

4.3 Results

We present explosion properties of all four models considered here in Table 4.2. The Table also includes yields of Ni, Si, and O as calculated within FLASH. Between the lowest mass model (P150) and the highest mass model (P250) the nickel yield for the 1D simulations increases by more than four orders of magnitude. This is a consequence of the steep dependence on

Table 4.1 Nickel and Silicon yields of simulations using the directionally-split (unsplit) hydrodynamics solver for P150, P175, P200, and P250 at the fiducial resolution (6.5×10^7 cm)

Model	$M_{\rm Ni}$ ($M_\odot$)		$M_{\rm Si}$ ($M_\odot$)	
	split	unsplit	split	unsplit
P150	3.11×10^{-3}	2.86×10^{-3}	5.91	5.85
P175	2.94×10^{-1}	3.16×10^{-1}	12.7	12.9
P200	14.5	12.1	21.8	22.4
P250	40.9	34.3	21.5	24.5

density and temperature of the associated nuclear reactions together with the dependence of the strength of the contraction on the mass of the CO core. The dependence on CO core mass of the results is in good agreement with previous work [Heg02; Kas11; Des13; Wha13; Wha14b; Koz14a; Cha15] (see Figure 4.3).

Table 4.2 1D explosion properties for P150, P175, P200, and P250 at the fiducial resolution (6.5×10^7 cm)

Model	$M_{\rm CO}$ ($M_\odot$)	$E_{\rm exp}$ (B)	$\rho_{\rm c}$ (10^6 g/cm^3)	$T_{\rm c}$ (10^9 K)	$M_{\rm Ni}$ ($M_\odot$)	$M_{\rm Si}$ ($M_\odot$)	$M_{\rm O}$ ($M_\odot$)
P150	65.7	5.58	1.42	3.41	2.86×10^{-3}	5.85	48.5
P175	81.4	17.7	2.27	3.92	3.16×10^{-1}	12.9	51.3
P200	100.9	49.4	3.92	4.89	1.21×10^{1}	22.4	42.2
P250	126.7	82.1	7.03	5.83	3.43×10^{1}	24.5	35.9

Silicon is produced from primarily oxygen (and some carbon). Then, if the temperatures and densities get high enough (as in P200 and P250), nickel is produced in substantial quantities primarily from fusion of silicon. To first order, the explosion converts some number of solar masses of oxygen into silicon and nickel. Thus, the final oxygen masses are substantially lower than their pre-explosion values while both the silicon and nickel yields are substantially higher than their pre-explosion values. Note however that a substantial amount of oxygen remains unburnt in each case and thus constitutes a large fraction of the ejected mass.

Figure 4.4 shows the compositional profiles of the ejecta after evolution in FLASH is complete. The wide range in nickel yield between the models is evident from the figure as the higher mass models reach core conditions sufficient for explosive silicon burning in addition to the explosive oxygen burning which is achieved in all the models. Also note how the helium appears in the core for the higher mass models reflecting the dissociation of newly-produced nickel into helium that occurs due to increasingly high core temperatures. This is the mechanism by which cores of higher mass will collapse directly to black holes. The unburnt oxygen is confined

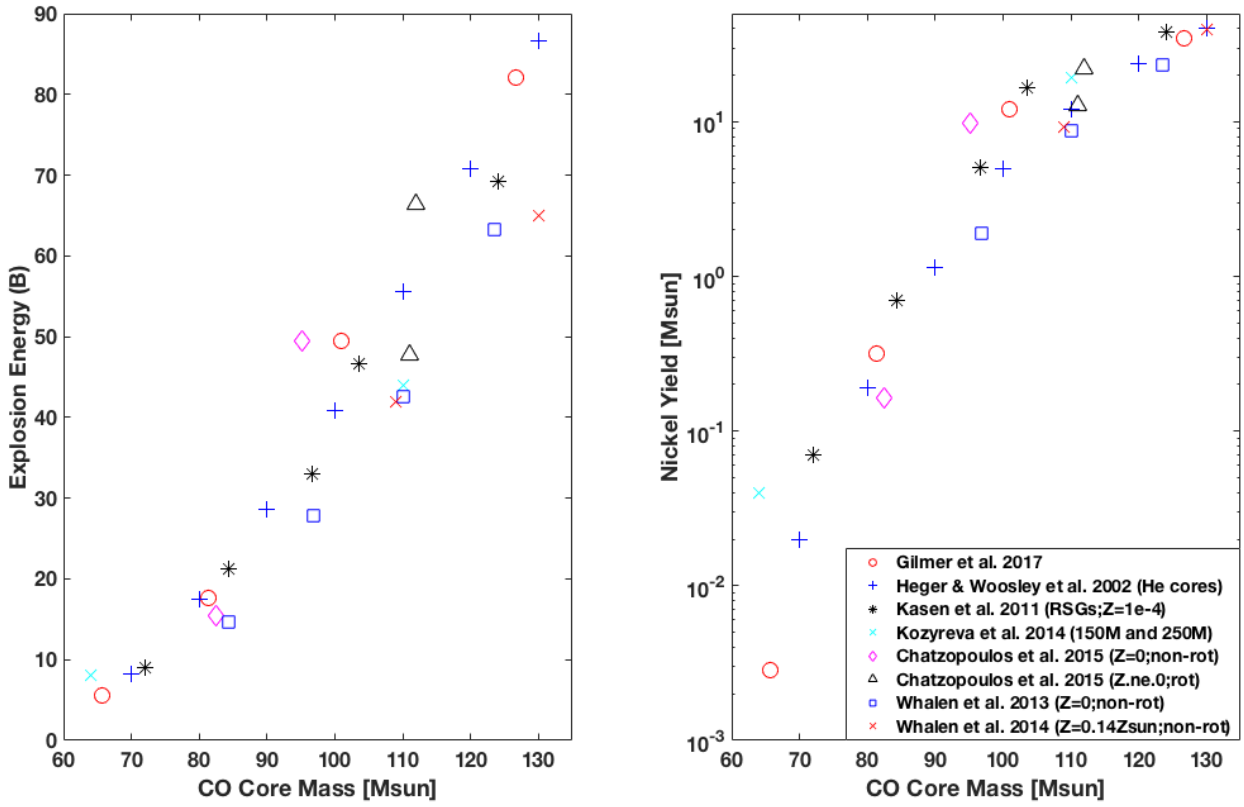

Figure 4.3 Explosion energies (left) and nickel yields on a log-scale (right) plotted versus carbon-oxygen core mass for our models (red circles) and for various other works cited above (see legend, which also includes rotation and metallicity information).

to a shell in between two regions where nucleosynthesis occurred. The region interior to the unburnt oxygen shell experiences the bulk of the nuclear burning. However, there is also a small region (in terms of mass coordinate) outside of this shell in which oxygen captures alpha particles from the inner edge of the stellar envelope. Such burning produces mainly silicon and is triggered by shock heating.

4.4 Conclusion

In this Chapter, we described the basic computational setup for our explosion simulations with explanations for choices of physical ingredients and model parameters. Much of this setup will carry over to our multidimensional study in the next chapter (Chapter 5). Using this setup, we have successfully simulated PISN explosions for all four models and have found general agreement with other results from the literature. Our main results are yet to come in our findings from the multidimensional study (Chapter 5) and in our calculations of synthetic

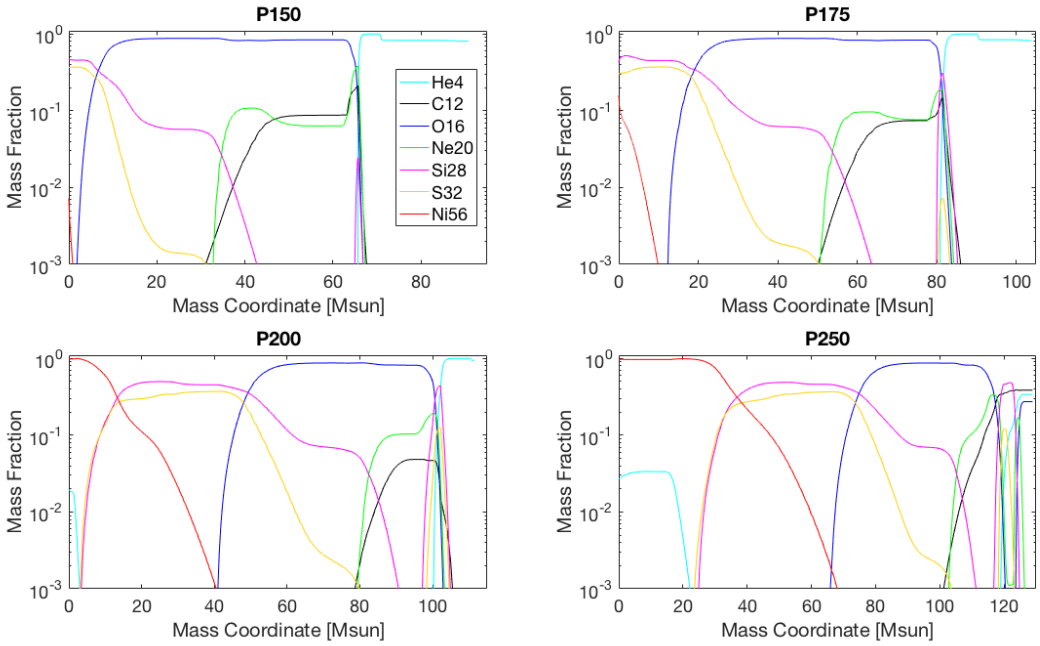

Figure 4.4 Mass fraction profiles for the 1D simulations of P150 (top left), P175 (top right), P200 (bottom left), and P250 (bottom right) from Table 4.2.

observations (Chapter 6) where the progenitor characteristics, in particular, come into play.

CHAPTER

5

PAIR-INSTABILITY SUPERNOVA EXPLOSIONS IN MULTI-D

5.1 Introduction

In this chapter, I will detail the method of extension to multiple dimensions of the study of PISN explosions in 1D from the previous chapter. I will then present the results that came out of this extension and discuss their consequences. A motivation of this study is the fact that the real world has three spatial dimensions (at least!) and explosive astrophysical events are rarely spherically symmetric. Diversions from spherical and axial symmetry are required to explain a plethora of similar astrophysical processes including core-collapse supernovae, thermonuclear (Type Ia) supernovae, and gamma-ray bursts, as well as anything that produces a gravitational wave signal. Given these examples, it is certainly worthwhile to remove the restrictions of symmetry by simulating in multi-D.

Prior to this study, other groups had investigated PISN explosions in 2D [Cha14; Che14a] finding that the deviations from spherical symmetry are remarkably small, at least in the absence of strong rotation during the explosion. It was found that the added degrees of freedom did not considerably influence the contraction and burning phases. Nevertheless, Rayleigh-Taylor instabilities were found to grow at several compositional interfaces during the ejecta

expansion phase. Since it is generally agreed that RT instabilities grow faster in 3D than in 2D, at least initially [Kuc14], the absence of any published 3D PISN explosion results was a additional strong motivator for this study. Thus, we expected to find stronger mixing in 3D than in 2D (an expectation further supported by the result by Calder et al. [Cal02] in which, for single-mode perturbations, Rayleigh-Taylor instabilities grew considerably faster in 3D than in 2D in FLASH).

Further motivation for this study is provided by recent observations of certain slowly-evolving SLSNe. These events exhibit light curve decline rates consistent with an event powered by the radioactive decay of a large quantity of Nickel-56, which high-mass PISNe are expected to produce. However, the light curves of previous PISN models fail to reproduce the quick rise to peak luminosity seen in these events. Additionally, the models have difficulty achieving the high photospheric temperatures and velocities measured. Both discrepancies between model and observation could be alleviated by the outward mixing of the radioactive Nickel-56 in the PISN ejecta [Koz15].

5.2 Methods

First, we need to choose a time to begin our multidimensional calculations. In order to capture any instabilities that may be seeded at early times (as in Chen et al. [Che14a]) we take profiles from the 1D simulations at ~ 20 s prior to maximum compression. Then, we initiate 1D, 2D, and 3D simulations for all the models starting from these initial profiles. We run 1D simulations because, as we will show, the multidimensional simulations have smaller domain sizes. Therefore, to better isolate the dimensional effects, we compare to a 1D simulation with a similar domain size. Simulating with exactly the same domain size for all three dimensions is impossible due to our use of differing geometries. We used the recommended geometry settings in FLASH for each dimensionality: "spherical" for 1D, "cylindrical" for 2D, and "Cartesian" geometry for 3D. Since we were mapping a spherical grid onto non-spherical geometries in the 2D and 3D cases, a slightly smaller domain was evolved (a cube (3D) or half of a square (2D) that could fit inside a sphere (3D) or semicircle (2D) of radius equal to the domain size of the 1D simulation). It was important that the original 1D simulations included a small part of the envelope in their 'cores' so that the domains in 2D and 3D could still contain the entire CO cores. The dimensions of our new grids are in 1D: $0 < r <$ xmax, in 2D: $0 < r <$ xmax, $-$xmax $< z <$ xmax, and in 3D: $-$xmax $< x, y, z <$ xmax, where, for each model in 3D, xmax had to be less than $1/\sqrt{3}$ times the radius of the original 1D simulation. This was necessary so that the initial state of the 3D cube could be completely specified by the spherical input model. Similarly, for 2D, each model's xmax had to be less than $1/\sqrt{2}$ times the radius of the original 1D simulation so that the initial

state of the 2D half square could be completely specified by the spherical input model. Values satisfying these criteria are given in Table 5.1.

Table 5.1 Values of xmax for the original 1D simulations and for the set of multidimensional simulations for each model.

xmax (10^{10} cm)	P150	P175	P200	P250
original 1D	16.70	3.334	4.167	5.000
Multi-D	2.500	1.670	2.083	2.500

Initially we ran simulations using the AMR settings of the 1D study described in Section 4.2 (except we relaxed the minimum refinement level by two levels to a resolution of 5.2×10^8 cm because the simulation time scales were short enough so that the spurious mass inflow was negligible). We noticed, however, that when interfaces between compositional shells crossed jumps in refinement, spurious mixing followed. Figure 5.1 illustrates this problem occurring in a 2D simulation. In the left panel, a newly produced Silicon-rich shell of material approaches a drop in refinement at a radius of about 3×10^9 cm. The resolutions on the grid can be understood through the sizes of the blocks which are depicted as the black outlines of squares, each containing 16x16 computational cells. One can already see the shape of the outer boundary of this Silicon-rich shell being affected near block vertices located on refinement boundaries. These deformations act as seeds that grow via the RT instability. The right panel of Figure 5.1 shows the extent to which these perturbations grow in 13s. The mixing seen here is significantly greater than what we see in 2D when using a fixed grid (see the left panel of Figure 5.3 in Section 5.3). With a fixed grid, we also see RT instability growth, although it is significantly slower due to the absence of this effect, which is certainly not physical. For this reason, we elected to use a fixed grid in our multidimensional simulations.

This fixed grid consisted of nested cubes (3D) or half squares (2D) of different, but fixed, resolution settings. In 3D, the innermost cube (with edge length of 1.0×10^{10} cm) had the maximum resolution used (3.25×10^7 cm). This innermost cube was surrounded by a second, larger cube (edge length of 1.5×10^{10} cm) which has the next lower refinement level (one factor of two) in the volume not occupied by the innermost cube. The second cube is again surrounded by another (third) cube (edge length of xmax) which has again the next lower refinement level in the volume not occupied by the second cube. In 2D, we used a similar hierarchy of half squares in which the longer edges of the half squares corresponded to the cube edge lengths given above. We use the 'diode' boundary condition for all boundaries in 3D (which are all outer boundaries) and for all boundaries in 2D except the inner boundary (at the left side of the

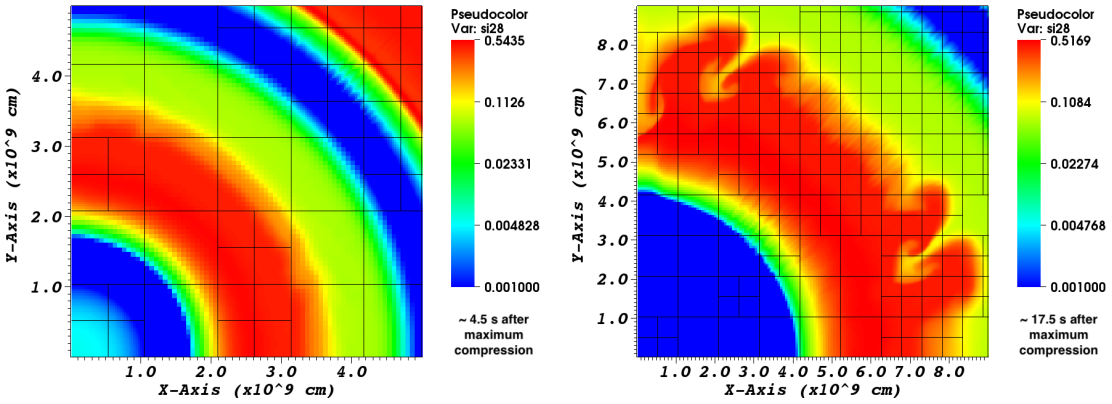

Figure 5.1 Pseudocolor of the ^{28}Si mass fraction on a log scale for a 2D simulation with AMR at 4.5 s (left) and 17.5 s (right) after maximum compression. The view is centered at the Si-O interface. This simulation involved five levels of refinement with minimum and maximum resolutions of 5.2×10^8 cm and 3.25×10^7 cm, respectively (although only the highest two refinement levels are populated during this time and region of interest). The boxes correspond to AMR blocks of 16x16 cells each. Also note the physical scale increases from left to right as the layer is expanding outward in space.

half square) for which we use 'reflect'. We chose the aforementioned cube sizes to ensure that the compositional boundaries all remain in the inner cube throughout each simulation. We ran each simulation until the shock reached the edge of the grid, at which point all significant energy generation from nuclear burning had ceased. All other FLASH settings are the same as in the 1D study.

To facilitate the comparison of our multidimensional results with our 1D results, we further processed the 3D data by computing angular averages for all the variables. The angular average is a two-step process. First, the state variables are mass-averaged over a 'block' (4^n cells, where n is the number of dimensions). Then, we perform another mass-weighted average on to a coarser radial grid in which the bin widths are 1.5×10^8 cm. During this second average, the 5^{th} and 95^{th} percentile values for each variable in each bin are also computed. This last step allows us to see how wide the range of values for a particular variable can be within a single radial bin and is used for the shaded regions in Figure 5.2 in the following subsection 5.3.

5.3 Results

The results of the simulations described in the previous section are included in Tables 5.2–5.5. The main trend evident from the tables is that, for all models considered, the explosions lose strength with increasing dimensionality. At the fiducial resolution (6.5×10^7 cm), the differences are small, but the trend is clear. Since there is very little asphericity during the contraction

and burning phases, and thus we expect the dynamics to be unaffected by the number of dimensions, we attribute the trend to differences in the effective radial resolution. In 1D, the resolution is literally a radial resolution, whereas in 2D and 3D, the computational cells are shaped differently (as squares and cubes of edge length equal to the radial resolution in 1D). These squares and cubes have orientations with respect to the radial direction that depend on their position in space. The effective radial resolution thus has an angular dependence and only approaches the constant radial resolution in 1D when the cell centroids lie near the axes. This leads to the expectation that a higher resolution is needed to achieve convergence in 2D and 3D.

Table 5.2 1D, 2D, and 3D explosion properties for model P150 at the fiducial maximum resolution of 6.5×10^7 cm

P150	E_{exp} (B)	ρ_c (10^6 g/cm^3)	T_c (10^9 K)	M_{Ni} ($M_\odot$)	M_{Si} ($M_\odot$)	M_O ($M_\odot$)
1D	5.81	1.42	3.41	3.23×10^{-3}	5.81	48.3
2D	5.66	1.40	3.40	2.77×10^{-3}	5.66	48.5
3D	5.68	1.39	3.39	2.59×10^{-3}	5.59	48.5

Table 5.3 1D, 2D, and 3D explosion properties for model P175 at the fiducial maximum resolution of 6.5×10^7 cm

P175	E_{exp} (B)	ρ_c (10^6 g/cm^3)	T_c (10^9 K)	M_{Ni} ($M_\odot$)	M_{Si} ($M_\odot$)	M_O ($M_\odot$)
1D	17.4	2.27	3.92	3.21×10^{-1}	12.8	51.3
2D	17.4	2.23	3.90	3.07×10^{-1}	12.8	51.4
3D	17.3	2.21	3.89	3.00×10^{-1}	12.8	51.5

Table 5.4 1D, 2D, and 3D explosion properties for model P200 at the fiducial maximum resolution of 6.5×10^7 cm

P200	E_{exp} (B)	ρ_c (10^6 g/cm^3)	T_c (10^9 K)	M_{Ni} ($M_\odot$)	M_{Si} ($M_\odot$)	M_O ($M_\odot$)
1D	48.7	3.92	4.89	1.18×10^{1}	22.4	42.6
2D	49.0	3.84	4.86	1.18×10^{1}	22.4	42.5
3D	48.6	3.79	4.85	1.16×10^{1}	22.4	42.6

Table 5.5 1D, 2D, and 3D explosion properties for model 250 at the fiducial maximum resolution of 6.5×10^7 cm

P250	E_{exp} (B)	ρ_c (10^6 g/cm^3)	T_c (10^9 K)	M_{Ni} ($M_\odot$)	M_{Si} ($M_\odot$)	M_O ($M_\odot$)
1D	82.5	7.15	5.85	34.6	24.4	35.8
2D	82.2	6.84	5.79	34.0	24.5	36.1
3D	81.7	6.64	5.75	33.5	24.6	36.4

To test this, we increased the resolution everywhere in the grid by a factor of two and ran the simulation again in 1D, 2D, and 3D. Because of limitations in computing time, we restrict ourselves to the most massive model, P250. Table 5.6 shows the explosion properties in 1D, 2D, and 3D at the new resolution of 3.25×10^7 cm. At this resolution we are fully converged in explosion energy, silicon yield, and nickel yield between the 1D, 2D, and 3D simulations. The CPU time for the 3D simulation was $\sim 50,000$ hours.

We calculate explosion energies similarly to Chatzopoulos et al. [Cha15] (see their Table 1):

$$E_{\rm exp} = E_{\rm tot,f} - E_{\rm tot,i} + E_{\rm tot,p}, \tag{5.1}$$

where the difference between $E_{\rm tot,f}$ and $E_{\rm tot,i}$ is in essence the energy released by nuclear burning and $E_{\rm tot,p}$ is the initial negative binding energy of the progenitor model. The total energies include contributions from the kinetic, internal, and gravitational potential energies, where the internal energy receives all energy released by nuclear reactions.

Table 5.6 1D, 2D, and 3D explosion properties for model P250 at high maximum resolution (3.25×10^7 cm)

P250	E_{exp} (B)	ρ_c (10^6 g/cm^3)	T_c (10^9 K)	M_{Ni} ($M_\odot$)	M_{Si} ($M_\odot$)	M_O ($M_\odot$)
1D	81.9	6.90	5.80	34.0	24.5	36.1
2D	81.9	6.85	5.79	34.0	24.5	36.1
3D	81.8	6.77	5.77	33.8	24.6	36.2

We now turn our attention to the multidimensional effect of mixing in the supernova ejecta. The mixing is caused by the growth of RT instabilities at compositional boundaries (discussed in Section 2.6). In our simulations, mixing sets in after maximum compression in the expanding ejecta. The instabilities grow for about 15s at which point the shock reaches the edge of the grid

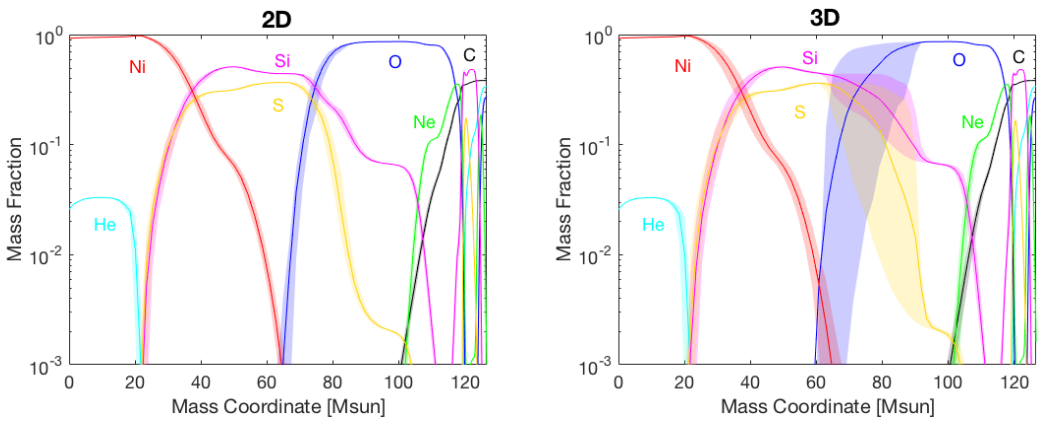

Figure 5.2 Angular-averaged mass fraction profiles for the high resolution (3.25×10^7 cm) simulations in 2D (left) and 3D (right).

and our simulations are halted. Figure 5.2 shows the 2D (Left) and 3D (Right) angular averaged profiles at the end of the simulation for model P250 at the increased resolution. The shaded vertical width for each nuclear species is computed for each bin in the angular averaging scheme described in Section 5.2 from the distribution of mass fractions involved in the bin average. The lower (upper) edge of the shaded region corresponds to the mass fraction that is greater than 5% (95%) of the values occurring in the bin average. Thus, the vertical width can be thought of as a measure of the degree of asphericity for each mass coordinate. Comparing the left and right sides of the figure shows that mixing is stronger in 3D than in 2D. This is evident from the larger shaded areas as well as the shallower line gradients near compositional interfaces in the 3D case. This result is not so surprising as it is generally agreed that the RT instability grows faster in 3D than in 2D, at least initially [Kuc14]. Furthermore, Calder et al. [Cal02] find that this is true in FLASH for single-mode perturbations. Still, the increase in mixing seen when comparing our 3D to our 2D simulations is quite striking, especially between the silicon-rich and oxygen-rich layers of the ejecta.

We also note weak mixing at the Ni-Si interface, the effect of which is much too small to have an appreciable effect on the LC rise time (see Section 6 and Figure 6.11). It should be noted that the multidimensional phases of the simulations only followed the evolution until just before the shock exits the grid along the axes (when the shock radius passes 2.5×10^{10} cm) while the total radius of the model is 1.67×10^{11} cm. Thus, the amount of mixing seen should be regarded as a lower limit to the amount we would expect from the simulation at shock breakout.

In addition to the strength, the character of the mixing differs between 2D and 3D at the Si-O interface. Figure 5.3 shows the ^{28}Si mass fraction color coded on a log-scale for the 2D (*left*) and a slice of the 3D (*right*) simulations at the end of the simulation (the same data that

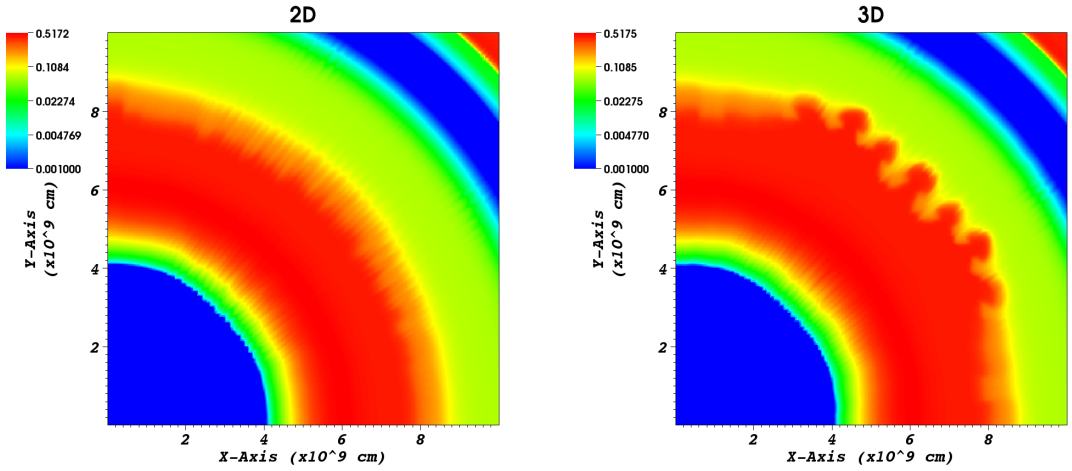

Figure 5.3 Pseudocolor of the ^{28}Si mass fraction on a log scale for the high resolution (3.25×10^7 cm) simulations in 2D (left) and 3D (right) centered at the Si-O interface.

was used to generate the ^{28}Si data for Figure 5.2). Each panel is centered on the most unstable layer (the Si-O interface). Also visible in the top-right corner of each panel is the inner edge of the outer silicon shell produced via shock burning (see Section 4.3). Examining the left panel of Figure 5.3 we note that, in 2D, very thin RT fingers exist on both the inside (the Ni-Si interface) and outside (the Si-O interface) of the Si-rich shell. Focusing now on the right panel, we see that the 3D simulation exhibits similar behavior to the 2D simulation at the Ni-Si interface but very different behavior at the Si-O interface where we see RT plumes whose growth results in much stronger mixing.

Also evident from Figure 5.3 is the angular dependence of the RT features. There is a distinct lack of RT plumes directed along the axes. The Cartesian grid has certainly imposed some numerical artifacts on the data. If mixing at this interface occurs in nature, as we expect, there would be no such angular dependence. However, it is unclear if there is an artificial suppression of RT mixing along the axes or if RT mixing is enhanced off axis. Simulations using a spherical geometry may help to shed light on this issue. Additionally, there is evident substructure in the RT plumes. We provide Figure 5.4 for a closer look at the plume at 45° in the right panel of Figure 5.3. At this scale one can even make out the computational cells. Even finer features may develop in a similar simulation with higher resolution that could further change the character (and perhaps also the strength) of the mixing. We leave this prospect for future work.

The contrasting character of the RT mixing between 2D and 3D is also evident from the densities at the Si-O interface. Figure 5.5 gives a zoomed-in view (the same view as in Figure 5.4) but with density color coded on a log-scale for the 2D (*left*) and the same slice of the 3D (*right*)

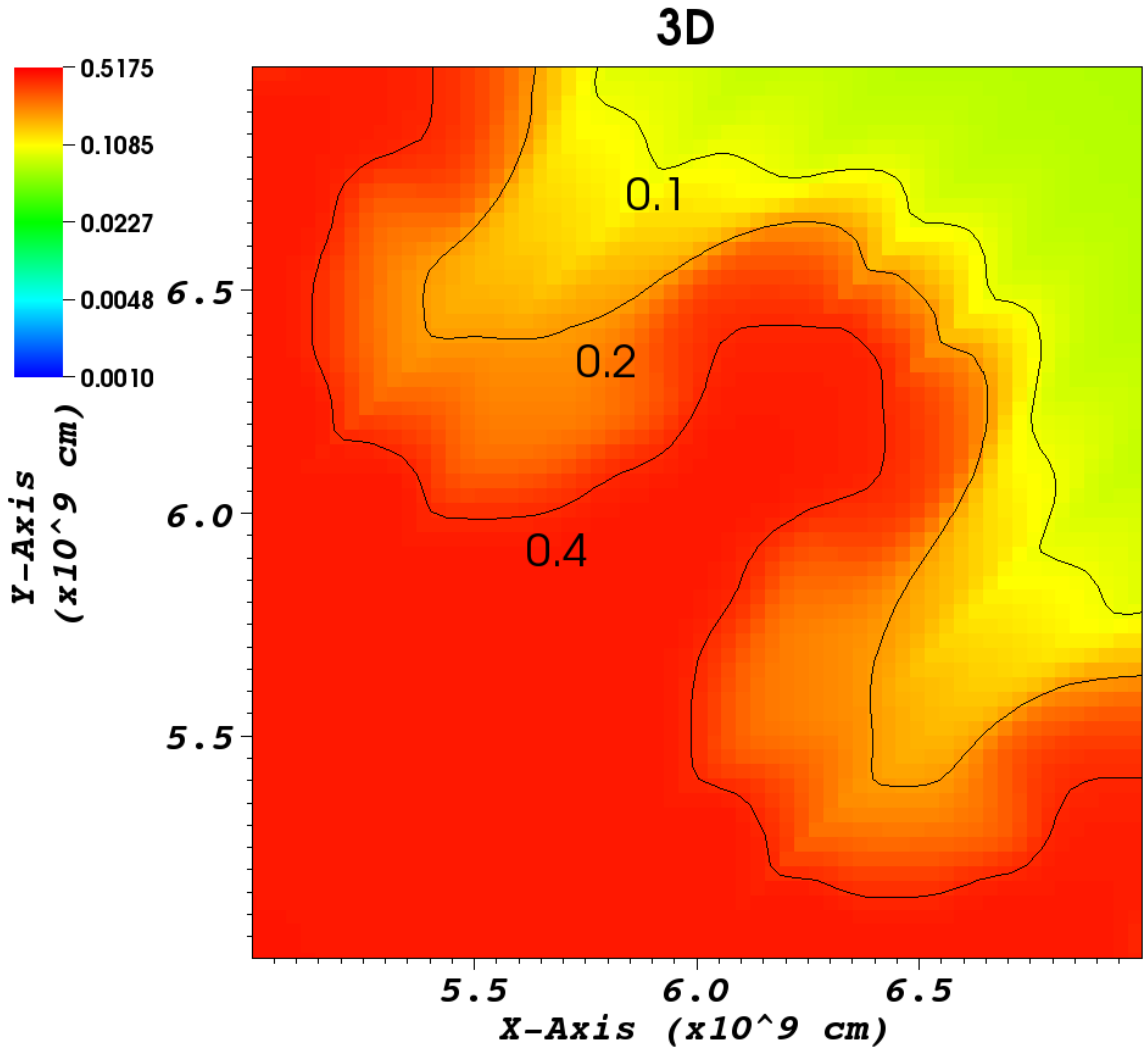

Figure 5.4 25 × magnification of the RT plume at 45° from the right panel of Figure 5.3. Overlayed are contours for three values of the ^{28}Si mass fraction.

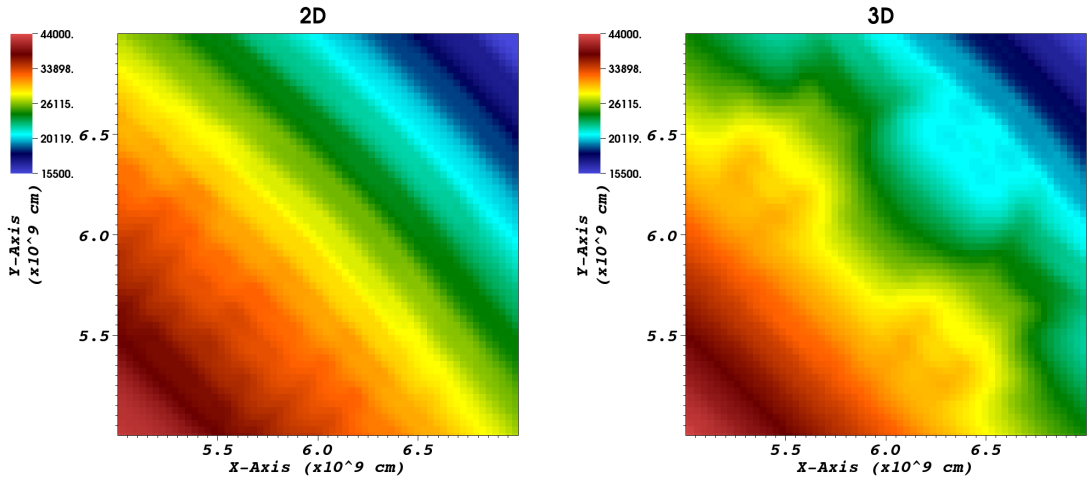

Figure 5.5 Pseudocolor of density on a log-scale for the high resolution (3.25×10^7 cm) simulations in 2D (left) and 3D (right). Note the smaller scale compared to Figure 5.3.

simulations. We see similar thin fingers and plumes in 2D and 3D, respectively. Note that the underdense regions correspond to the outgoing ^{28}Si fingers and plumes. The overdensities of these features are on the order of half of a percent in 2D and 5% in 3D. Unlike our result that the mixing is stronger in 3D than in 2D, the larger angular scale of the RT features in 3D compared to 2D is quite surprising and needs further investigation.

5.4 Conclusion

In this Chapter we have presented the first published results from 3D PISN simulations (from Gilmer et al. [Gil17]). We have achieved convergence in the main explosion properties between 1D, 2D, and 3D. Such convergence is consistent with our findings that mixing sets in after the explosive burning phase and therefore does not affect the main explosion properties. This conclusion is consistent with that of Chen et al. [Che14a]. Also consistent with other works [Che11; Jog11; Cha14; Che14a; Che15a] is our result that, in 2D, mixing is strongest significantly far from the core (i.e. mixing of nickel is minimal and mixing near the oxygen layer is stronger). Specifically in our case we found the strongest mixing at the inner edge of the oxygen shell (or the Si-O interface). Our 3D results show that the strongest mixing occurs in the same regions, but also that mixing everywhere is stronger in 3D than in 2D. This is consistent with the idea that RT instability growth rates increase from 2D to 3D [Kuc14]. In the next chapter (Chapter 6), we will explore the effects that our dimensionality may have on the observables of PISNe. While outward mixing of nickel is minimal, and thus the LC rise time is unlikely to be shorter

for 3D than for 1D, the mixing at the Si-O interface may be important for spectra.

CHAPTER

6

OBSERVATIONAL SIGNATURES OF PAIR-INSTABILITY SUPERNOVAE

6.1 Introduction

We now move on to discuss the computation of various observables from the simulation results of the previous two chapters. Historically, supernovae have been studied via their electromagnetic signals as this has, for the most part, been the only detectable signal. A wealth of information is available from such signals which includes the time-variability and amount of light emitted toward the detector as well as spectral information which constrains the composition, velocity, and temperature of the emitting material. Such information has often been used to constrain the explosion mechanism and history of the progenitor system. Here, we take the reverse approach and construct synthetic bolometric and multi-band light curves, color temperatures, and photospheric velocities for our models of PISNe, a SN type for which there are no confirmed detections. Our goal is to inform the interpretation of previous and future SN observations.

We extend our goal to include the interpretation of neutrino signals since we have now entered the era of "multi-messenger astronomy". In this exciting era there are many currently operating and planned observatories designed to detect signals consisting of things other than

light that are emitted from various astronomical sources. These non-light sources, for which directional information can be extracted, include neutrinos and gravitational waves. These efforts have already led to many theoretical confirmations as well as discoveries of new physics, such as neutrino oscillation phenomena.

CCSNe have long been thought to produce abundant neutrinos owing to the electron captures during the formation of the proto-neutron star and the subsequent neutrino pair production which cools it. This idea has been confirmed with the detection of neutrinos from SN 1987A by the Kamiokande II water Cherenkov detector [Hir87]. Likewise, Type Ia SNe (caused by the thermonuclear explosions of white dwarfs) are expected to produce neutrino pairs in large amounts due to the high temperatures reached, and calculations of predicted neutrino signals were done for two proposed explosion mechanisms. They are the deflagration-to-detonation scenario [Wri16] and the gravitationally confined detonation scenario [Wri17a]. In both cases, the neutrino signals were deemed detectable by the planned Hyper-Kamiokande out to a few kiloparsecs. Based on these results, one expects similar results from PISNe as they are also thermonuclear explosions.

CCSNe are also expected to produce strong gravitational wave signals due to the formation of the proto-neutron star and large turbulent motions. However, we do not expect such a strong gravitational wave signal from a PISNe. Even though the progenitor stars of PISNe are required to be very massive, the peak densities reached are about eight orders of magnitude lower than those reached in the proto-neutron star of a CCSN. Furthermore, PISNe are expected to explode without the large asymmetries that are ubiquitous in CCSNe, and our multidimensional models are consistent with this picture. For these reasons, we do not compute gravitational waveforms for our 3D models. One should mention, however, that the accretion disk surrounding a newly-formed direct-collapse black hole via the PI may produce a strong gravitational wave signal [Fry01].

This Chapter is organized as follows. In Section 6.2 we describe our method and results for computing light curves (and other electromagnetic observables) as well as some general implications of our results. We also assess the viability of a PISN interpretation of SLSN PTF12dam using our two most massive PISN models, P200 and P250. Finally, we assess the effects of mixing in our 3D explosion simulations on the bolometric light curve. Section 6.3 describes the PISN data to process as well as the neutrino emission, oscillation, and detector rate calculations. We conclude this subsection with some implications for possible future detections and calculations. In Section 6.4 we discuss the status of a current project on calculating spectra using our 3D model data with the goal of characterizing the effects on line formation of mixing at the silicon-oxygen interface. We then outline the steps that need to be taken to accomplish this goal. Finally, we summarize this Chapter in Section 6.5.

6.2 Light Curves with STELLA

For the purpose of comparing to current and future observations, we computed synthetic LCs for all our models. For accurate light curves, it was necessary to include the entire star in the simulations. On the timescale of our hydrodynamic simulations (several $\times 10^4$ s) we did not expect the envelope to change during the collapse of the core, so we re-appended the pristine envelope from the stellar evolution simulation to the exploding 'core' for each model. During the hydrodynamic simulation, the outer edge of the 'core' decreased in density and temperature causing a discontinuity between the final 'core' profile and the envelope profile. However, we needed to join the two profiles in a smooth manner while still preserving the outer envelope structure which is of the greatest importance to the light curve.

For the 1D simulations, we chose two points between which the density and temperature would be linearly interpolated in the $\log(\rho)$-radius or $\log(T)$-radius plane. For this modified region, the composition is uniform so the mass fractions are all set according to this uniform composition. One point was chosen to be in front of the shock. The other point was chosen at a point in the envelope and had to fulfill two criteria: (i) the local slope at this point has to be comparable to the slope of the connecting line and (ii) it has to be far enough from the surface so that the structure of the outer envelope was preserved. This method is illustrated using the density profile of P250 as an example in Figure 6.1. The mass and internal energy lost in this process is comparable to, but slightly lower than, the mass (and accompanied internal energy) that got added through the outer boundary prior to contraction reversal in the FLASH simulations. The total mass (energy) changes by less than 3% (2%) by this procedure.

In addition to the method described above, we investigated two additional limiting cases. For this test we used a slightly earlier time step than described above because it was necessary in order to apply the first method. Method A involved flattening the density and temperature profiles in the region between the shock and the edge of the core to match the values at the inner edge of the envelope. This method added a small amount of material ($\sim 1 M_\odot$) and a small amount of internal energy ahead of the shock. Method B was as described in the paragraph above, except that the exploding core remained untouched. Instead, the density and temperature in the inner region of the envelope were replaced by a straight line connecting the outermost point in the core to the same fixed point in the envelope from before. This method caused a loss of a similarly small amount of material (again, $\sim 1 M_\odot$) and internal energy ahead of the shock as method A. For both methods, the resulting profiles were mapped back into FLASH for further evolution and then mapped into STELLA [Bli06] using the standard procedure described below to compute light curves. The resulting light curves were almost identical, indicating that both methods are suitable for this study (see Figure 6.2). Our standard

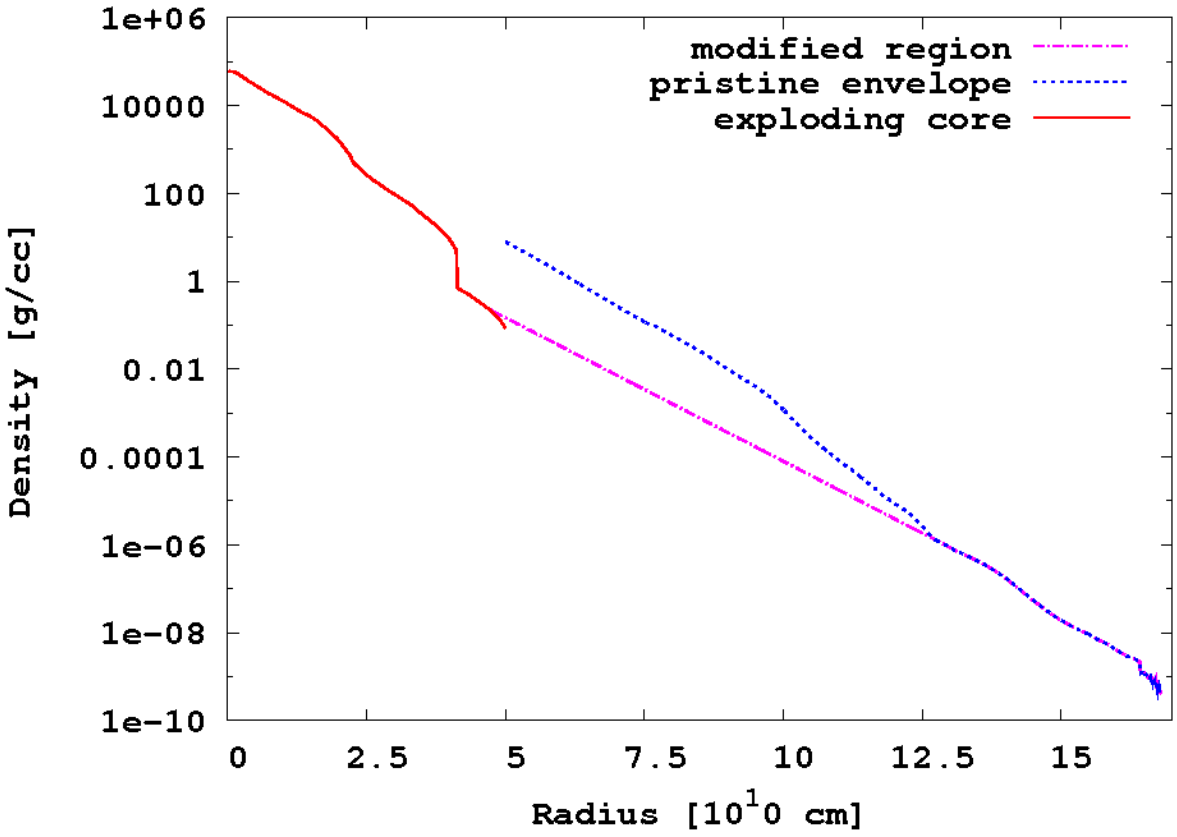

Figure 6.1 Density profile including the exploding core (red solid line), the pristine envelope (blue dotted line), and the modified region in between (magenta dashed line).

method for re-appending the envelope represents an intermediate method between method A and B, in which matter and energy are removed ahead of the shock (shown by the red line in Figure 6.1).

In 3D, the simulations were computationally too expensive to include the entire star. In this case, we conjoined an angular average of the 'core' with the pristine envelope using the same method as in the case of the 1D simulations. The only difference is that the angular-averaged 'core' profile from the 3D simulation represents a sphere of 2.5×10^{10} cm, whereas the pristine envelope begins at 5×10^{10} cm due to mapping from a sphere (on a spherical 1D grid to a Cartesian cube in 3D, as described in Section 5.2). We artificially set the densities and temperatures as described above (linear slope in the $\log(\rho) - r$ and $\log(T) - r$ plane, respectively). The velocities in this region are set to zero as during stellar evolution. For the composition we choose the composition of the envelope (which is almost perfectly uniform throughout the envelope). While this step erases information of this intermediate region, it

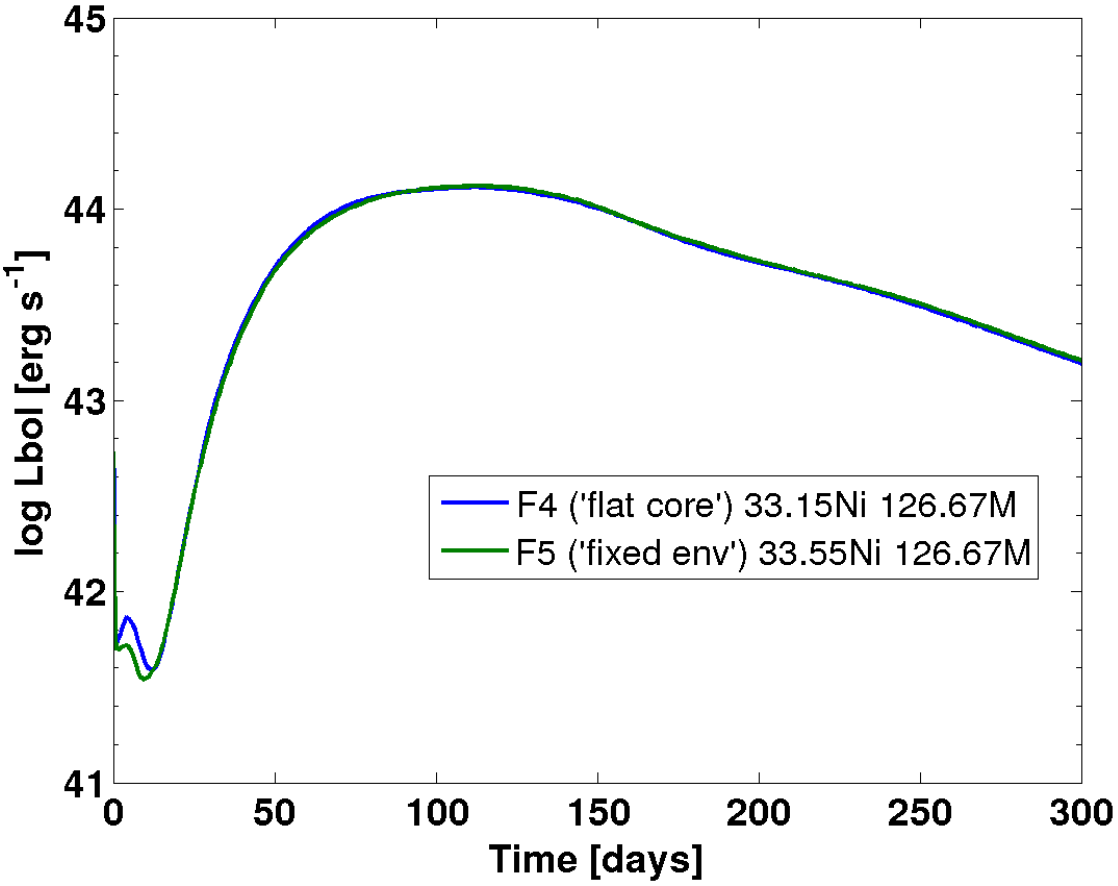

Figure 6.2 Light curves of P250 calculated after using the two extreme methods (method A and method B) for appending the envelope described in the text.

preserves the information from the multi-dimensional simulation of the 'core', such as the amount of outward mixing of nickel.

After re-appending the stellar envelope, the entire star was further evolved in FLASH before mapping to the radiation-hydrodyanmics code STELLA to compute light curves. For this, we use a maximum resolution of 6.5×10^7 cm and relax the refinement criteria back to their default values. We also allow a lower minimum resolution of 5.2×10^8 cm (which is lower than in the simulations of the 'cores' only) since the low densities at the outer edge of the envelopes effectively remove the problem of mass inflow at the outer boundary of the computational domain. As before, we employ the 'reflect' ('diode') boundary condition for the inner (outer) boundary. The light curve calculations with STELLA described in the next paragraph use these final profiles.

We simulate the post-explosion evolution and construct synthetic LCs using the 1D radiation-

hydrodynamics code STELLA. We note that STELLA includes the hydrodynamic coupling between matter and radiation, allowing momentum to be imparted from the radiation field to affect the ejecta structure (more details of this code can be found in Blinnikov et al. [Bli98], Blinnikov et al. [Bli00], and Kozyreva et al. [Koz17]). Inclusion of this physics allows the gamma rays emerging from the decay of ^{56}Ni to push on the surrounding material. This leads to what is known as the "nickel-bubble effect" which has been explored by Noebauer et al. [Noe12] and Kozyreva et al. [Koz17] (see Figure 13 in Kozyreva et al. [Koz17] to see this effect in the context of PISNe). For PISNe, the "nickel-bubble effect" strongly influences the ejecta structure but affects the LC shape only slightly. What is more consequential for the LC shape in STELLA, however, is the included opacity table which predicts a shorter rise time than other radiation transport codes that have been used to calculate PISN LCs [Koz17].

We map the profiles from the FLASH simulations described in the previous paragraph after the shock had traversed half of the stellar radius for models P150 and P175, and just before shock breakout for models P200 and P250. The latter two models, due to their large explosion energies, developed very rapidly-moving shocks. Since the radiative transfer treatment of STELLA does not include corrections from special relativity, we truncated the models at $\sim 30\%$ of the speed of light. We calculate, following the above procedure, bolometric and broad-band LCs for all four models. Additionally, we calculate a bolometric LC that used the angular-averaged profile of the high-resolution 3D fixed-grid simulation of model P250.

Our PISN LCs are characterized by extremely luminous shock breakout (SBO) signals (a SBO is the first light from the SN escaping the star when the shock wave crosses the stellar surface). The peak luminosity of a SBO signal is mainly a function of explosion energy [Mat99] which is very high for our PISN simulations (see Table 4.2). The duration of the SBO signal is mainly dependent on the stellar radius [Mat99] which decreases with increasing mass (and explosion energy) for our models. Thus for our models, we expect a trend of increasing luminosity and decreasing duration of the SBO signal with increasing progenitor mass. Our SBO signals are presented in Figure 6.3[1]. From the figure it is clear that the general trend in luminosity is satisfied with the exception of P250, whose peak SBO luminosity is actually less than that of P150. This is due to the aforementioned truncation at 30% of the speed of light which, for this model, caused the shock to be almost exactly at the edge of the star for the start of the STELLA simulation. Thus, in reality, we expect SBO from such a PISN to be more luminous than the SBO calculated for P200. While we miss an accurate peak luminosity for SBO, the truncation does not affect the main LC. The trend expected from the stellar radii is confirmed, however (see Table 3.1, and note that both the stellar radii and the SBO durations are very similar for

[1]We estimate the duration of the shock breakout event the same way as in [Kas11], i.e. the full width at half-maximum.

P150 and P175).

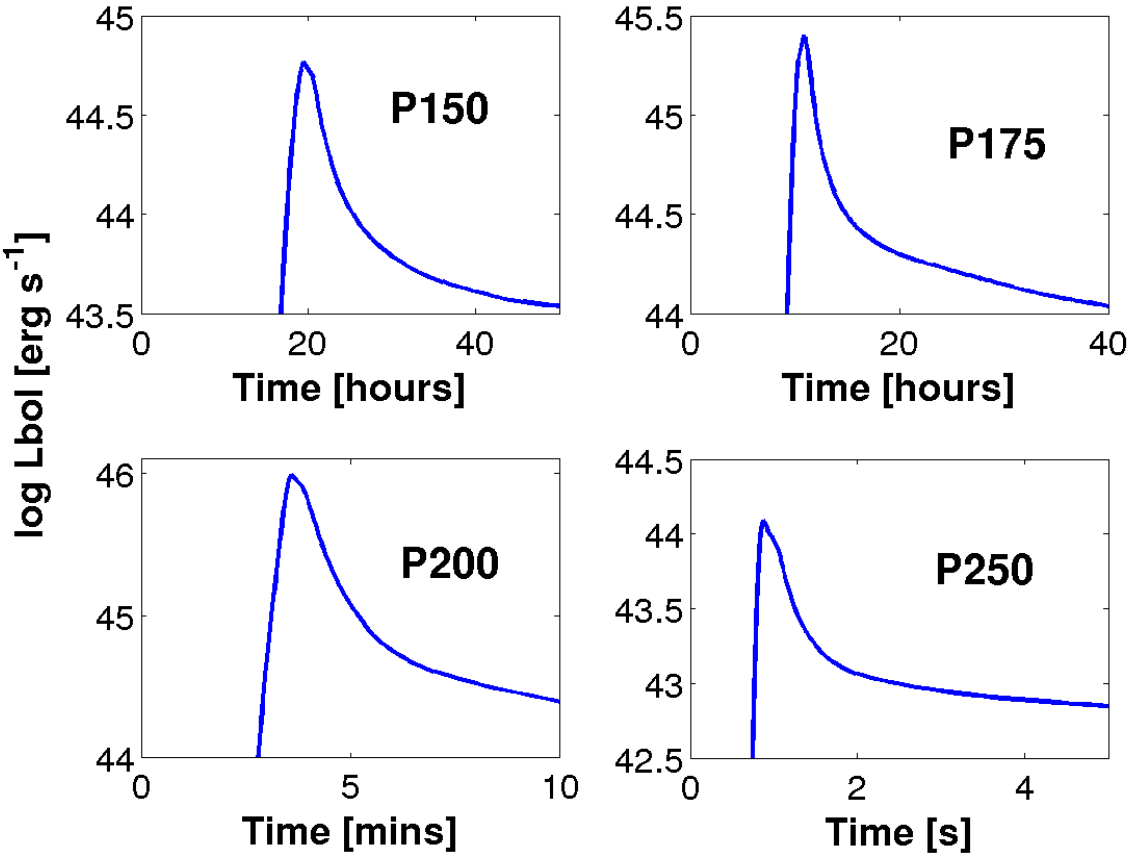

Figure 6.3 Shock breakouts of our PISN models.

SBO signals are notoriously difficult to detect and may even require some luck [Sod08; Gar16]. It would be rare indeed to detect a SBO from a rare type of SN like a PISN. However, such a detection would have the potential to identify a PISN (more on this to come). For this reason, we comment on some cosmological considerations.

For the massive and compact P250, the SBO signal lasts for only half of a second. However, if the PISN occurs far away (which is consistent with the Z=0.001 metallicity of our models), the duration of the signal is significantly increased by cosmological time dilation (to ~ 5 s for a such a PISN at redshift z=10). Additionally, the signal will be shifted to longer wavelengths via cosmological redshift (from the ultraviolet to the optical and infrared bands at z=10). The duration of the SBO signal from P200 is a bit longer at ~ 0.7 min (~ 7 min at z=10). These timescales, even for a distant supernova, are too short to realistically hope for a detection.

Models P150 and P175, however, have much longer SBO durations: 4.2 h for P150 and 1.7 h for P175. At z=10 these durations become on the order of a day, meaning detection with upcoming survey telescopes are feasible (LSST's "baseline cadence" ensures a covering of the available sky in about three nights [Mar17]). Finally, for completeness, we quote the SBO color temperatures for our models: 7.8×10^5 K (67 eV) for P150 and P175, 6.5×10^6 K (560 eV) for P200, and 2.2×10^6 K (200 eV) for P250 (like the peak luminosity of the SBO signal, in reality, we expect a hotter color temperature for this model than that of P200).

Next, we present our main results in this Chapter, the bolometric LCs for all four models[2] shown in Figure 6.4. From the figure, it is clear that the peak luminosities depend strongly on the ejected nickel masses which we include in the figure. We also include a line delineating the boundary between ordinary SNe and SLSNe which shows that, of all four models, only P250 would be considered a SLSN if observed. Based on this fact, we estimate that only PISN models with CO cores above about 110 $M_\odot$ (or producing more than about 15 $M_\odot$ of ^{56}Ni) will be observed to be SLSNe. The LC for P200 would be seen as a luminous SN, while P175 exhibits a peak luminosity typical of type II SNe. P150, however, does not have a Ni-powered maximum due to its extremely low yield of ^{56}Ni. We note one property of our PISN LCs is their long duration which we attribute to the high ejecta mass (this property is common to all PISN model LCs). Also, the peak phase very nearly resembles the plateau phase of a type IIP SN. One way in which our LCs deviate from others in the literature is their relatively short rise times. For our three models that have clear peaks, the rise times are about 110 days (about 50 days shorter than previously published PISN LCs [Kas11; Des13]). This is a consequence of both the relative compactness of our progenitors and the relatively low opacities predicted by STELLA. This is discussed in detail in Kozyreva et al. [Koz17]. Our P250 model is totally hydrogen-free, while P200 is nearly hydrogen-free. This would cause them to appear like Type Ic SNe, as the photosphere is located even below the helium-rich layers. The early phase of the P150 LC (where it is brighter than the other models) is exhibits hydrogen recombination. Later on, the photosphere recedes into the oxygen-rich layers while the luminosity drops.

We note that the peak luminosities of the main LCs for are lower than the peak SBO luminosities for all models (except P250, but recall that its SBO peak luminosity is underestimated). The contrast is particularly stark for the lower mass models, P150 and P175. While these two models have ejected nickel masses comparable to (P175) or significantly lower than (P150) those expected in CCSNe, their shock break-out luminosities are much higher due to their explosion energies being many times higher. For these models, detection of the SBO could distinguish a PISN from an ordinary CCSN (P175) or a subluminous CCSN (P150).

While STELLA does not have the capability to produce synthetic spectra, it can calculate

[2]The light curve data are available via `http://www.astro.keele.ac.uk/~kozyreva/LCindex.html`.

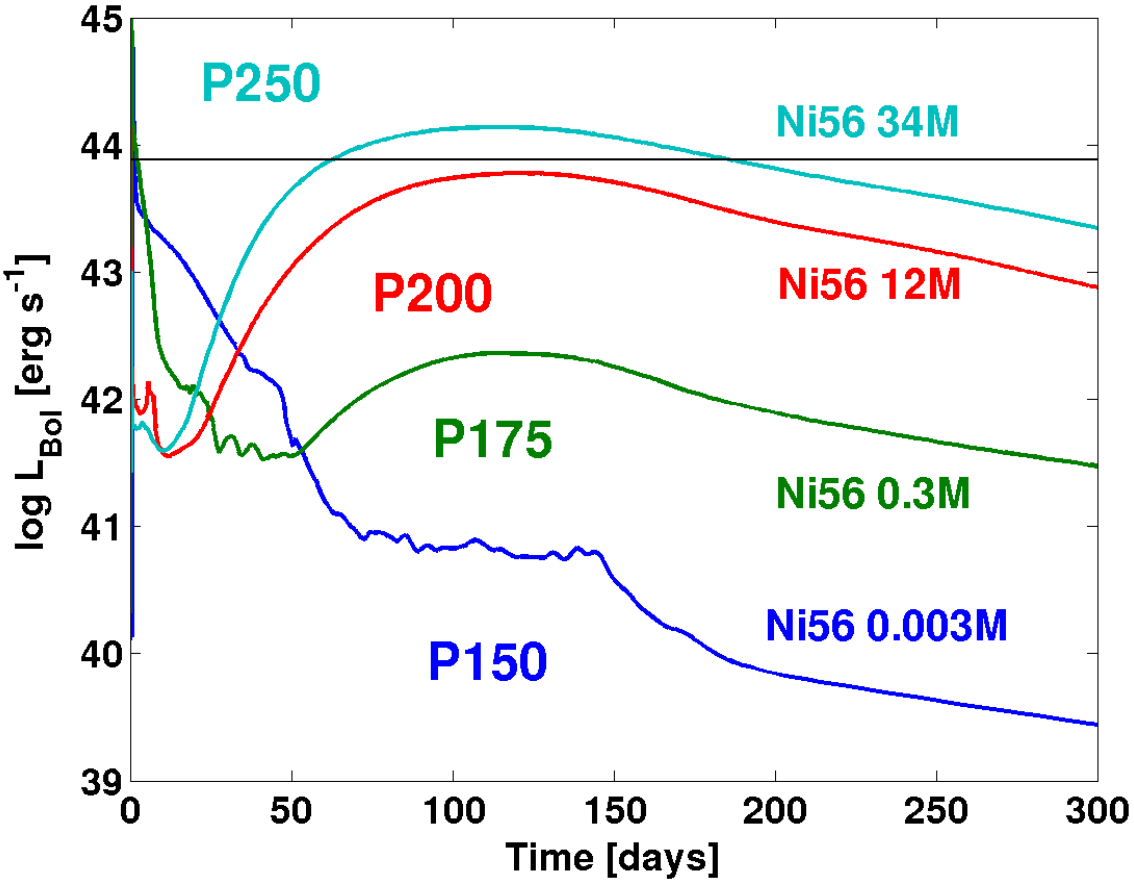

Figure 6.4 Bolometric light curves for P150, P175, P200, and P250 PISN models. The horizontal line at log L=43.9 erg s^{-1} corresponds to the SLSN criterion.

various broad-band LCs. We present these in Figure 6.5 for our models using the *U*, *B*, *V*, and *R* bands. As mentioned above, P150 does not exhibit a Ni-powered maximum. In this way it is like the 150 $M_\odot$ red supergiant model 150M from Kozyreva et al. [Koz14b]. Both LCs have a recombination phase instead although, due to P150 containing less hydrogen, the phase lasts for only half as long for P150. The peak magnitude for this phase of P150's LC is still high (like that of 150M) reaching –19 mags in the *U* band (–18 mags in *B*, *V*, and *R*). These peak magnitudes are comparable to plateau magnitudes of bright type IIP SNe [Sch94]. P175 has an even shorter recombination phase which would still motivate a type II SN classification if discovered during this phase. If instead P175 was discovered near its Ni-powered maximum, it would likely be classified as a type Ib SN. Finally, it is worth noting that our most massive and luminous models (P200 and P250) are brighter in the *U* band than in the *B* and *V* bands.

We previously mentioned that our models have significantly shorter rise times than other published PISN models. This is illustrated in Figure 6.6 where we compare the superluminous

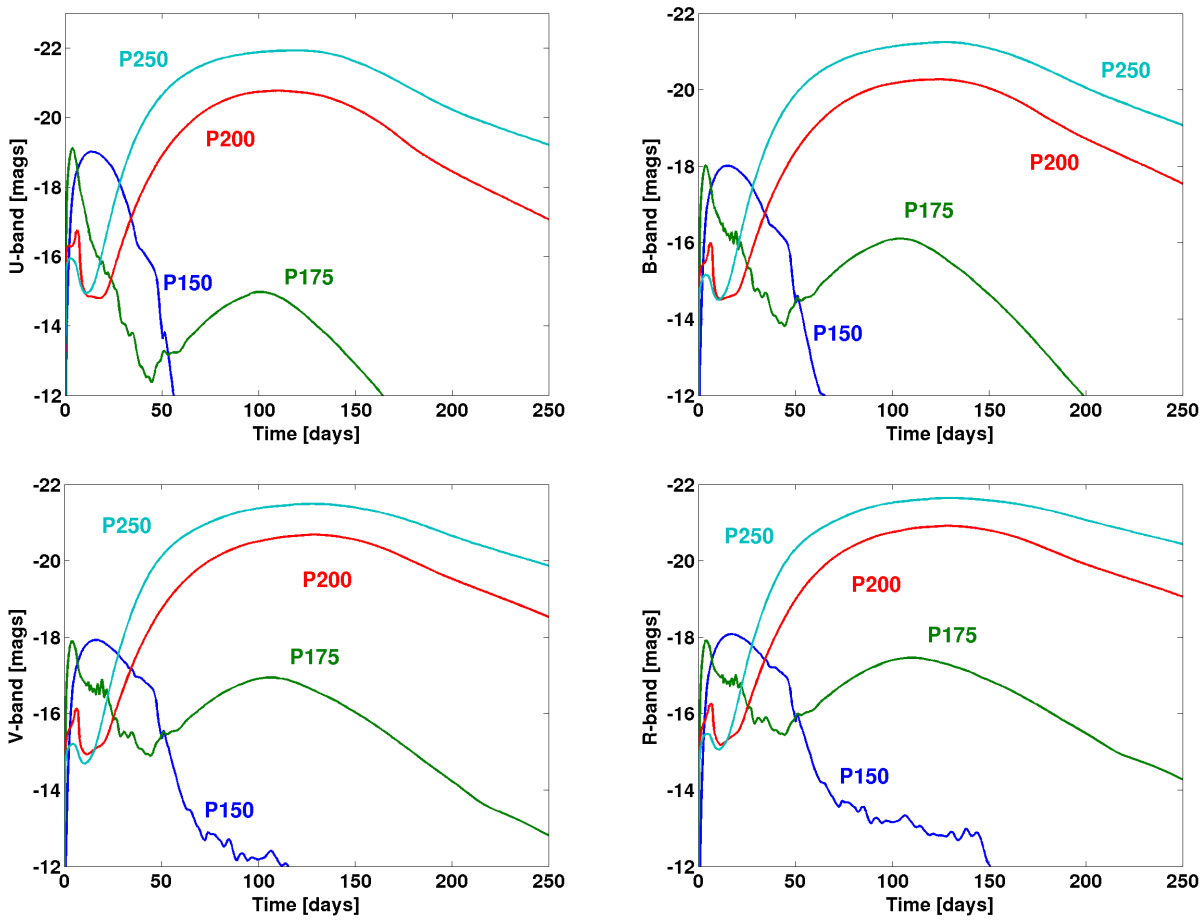

Figure 6.5 Light curves for P150, P175, P200, and P250 PISN models in U (top left), B (top right), V (bottom left), and R (bottom right) broad bands.

bolometric P250 LC with two different models of comparable CO core masses. One, 250M [Koz14b], is a hydrogen-rich red supergiant (a more massive analog to the 150M model mentioned in the last paragraph). The other, He130 [Kas11], was initiated as a 130 $M_\odot$ helium core. These two other models have longer rise times mainly because they were more extended in radius at the time of explosion. In this case, all were calculated with STELLA, removing any code-related differences like opacities.

The naturally fast-rising LCs arising from our self-consistently modeled compact PISN progenitors make them better suited for comparison with observations of SLSNe. We present such a comparison for the well-observed SLSN PTF12dam [Nic13; Che15b] in Figure 6.7. We shift the observed data by 100 d so that the peak approximately coincides with that of the synthetic LC of P250. There is a resemblance in LC shape near peak light between our models and SLSN PTF12dam. However, the observed LC peak is noticeably sharper. We complement this comparison with a comparison of broad-band LCs in Figure 6.8 which reveals that the

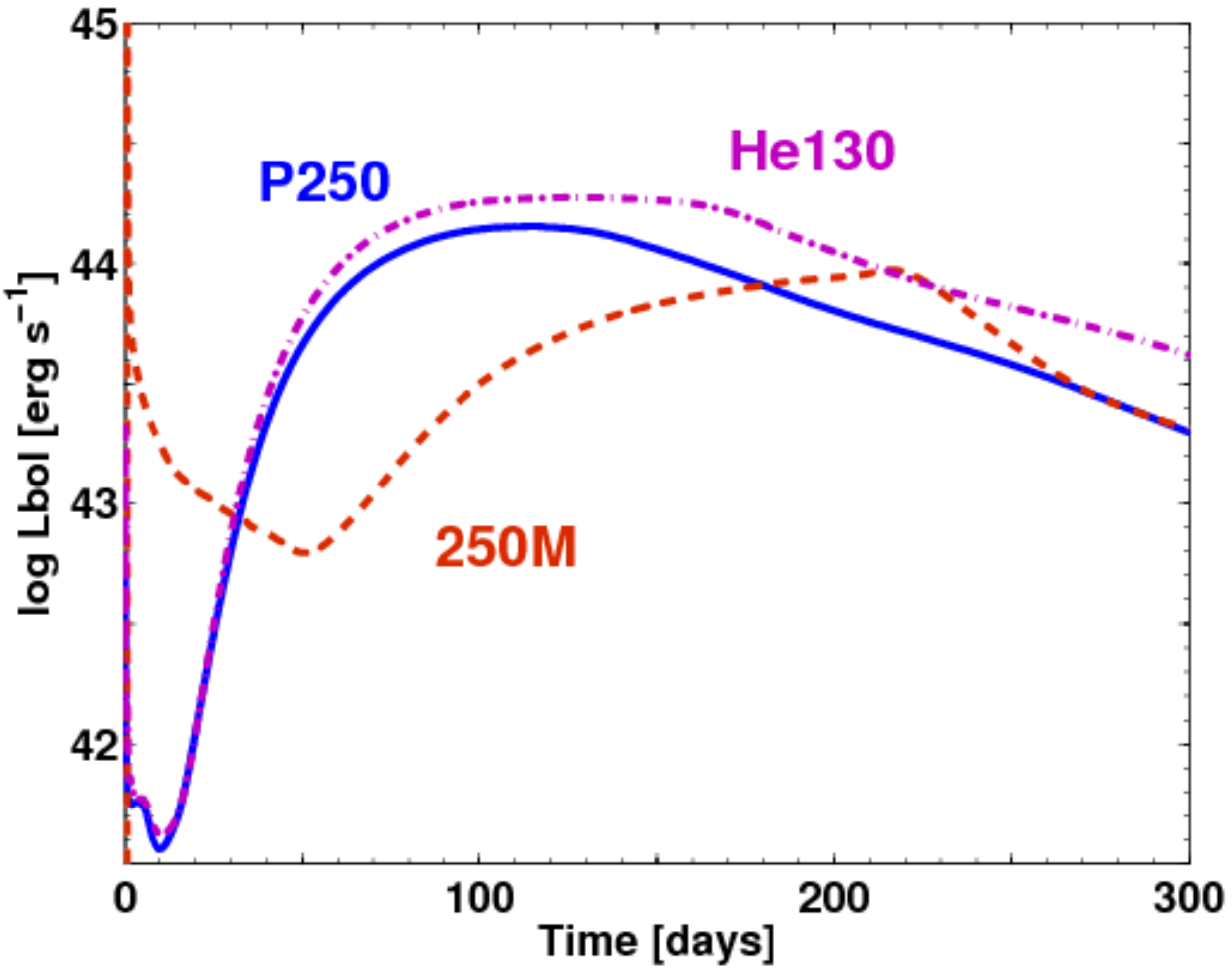

Figure 6.6 Bolometric LCs for the model P250 (solid), He130 (dash-dotted; Kasen et al. [Kas11]) and the hydrogen-rich model 250M (dashed; Kozyreva et al. [Koz14b]). All LCs are calculated with STELLA. This is Figure 4 from Kozyreva et al. [Koz17].

measurements at peak light are considerably brighter at short wavelengths and dimmer in the *r* band than the models (although the peak matches well in the *i* and *z* bands).

In Figure 6.9 we compare the color temperature evolution of our models with that of PTF12dam [Nic13]. Color temperatures for our models are estimated using the least-squares method. Although the observed color temperature is higher at maximum light than those of our models, our models reach higher values than those reached by other previously-published PISN models. The agreement between our models and the observations becomes better for the post-peak phase and then worse again for the last observation. In Figure 6.10 we compare photospheric velocities with those of PTF12dam [Nic13]. The P250 model matches the observations in this category very well (although they are limited to the epoch very near peak light). Based on these comparisons we conclude that, although some features of the observations

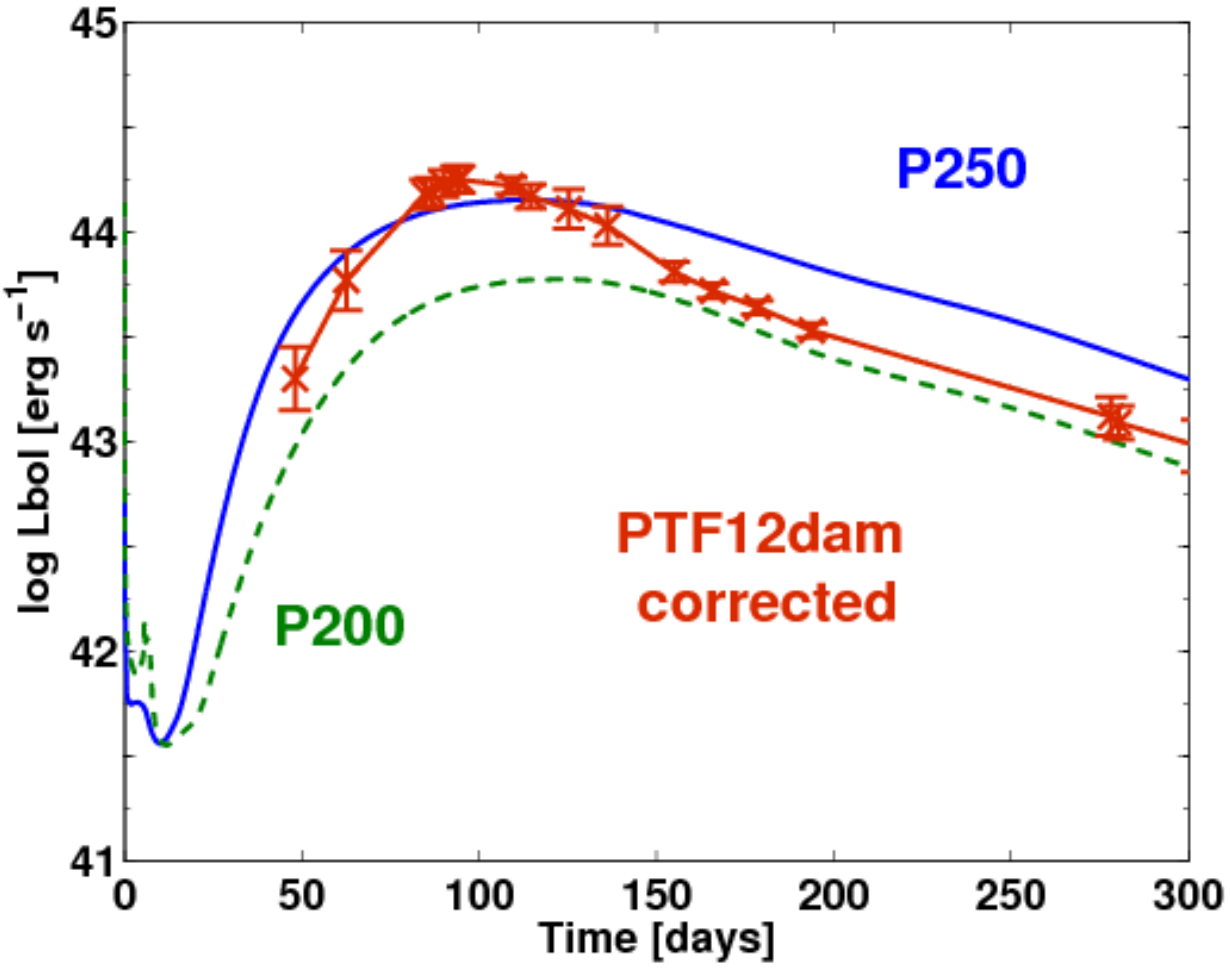

Figure 6.7 Bolometric LCs for the P200 (dashed) and P250 (solid) PISN models and SLSN PTF12dam (crosses). This is Figure 5 from Kozyreva et al. [Koz17].

remain unexplained, the PISN model is still viable for PTF12dam.

Our exploration into the multidimensional treatment of PISN explosions was largely motivated by the remaining discrepancies between our synthetic observations and the actual observations of PTF12dam. This, together with results from Kozyreva & Blinnikov [Koz15] which show dramatic effects on LC evolution from the artificial mixing of ^{56}Ni in the PISN ejecta, prompted us to explore natural mixing of ^{56}Ni in PISN explosions. Unfortunately, our 3D results revealed very minimal outward mixing of ^{56}Ni (see Figure 5.2). Nonetheless, we calculated a bolometric LC using the angular-averaged profile from the 3D calculation and this is presented in Figure 6.11. We include the LC calculated from the 1D simulation for comparison and find no significant differences in the LC shape. We stress that we only followed the evolution in 3D for $\sim$ 34 s (or until the shock had traversed about one seventh of the stellar radius). Allowing more time for instabilities to grow may lead to more substantial mixing of ^{56}Ni. Furthermore, if

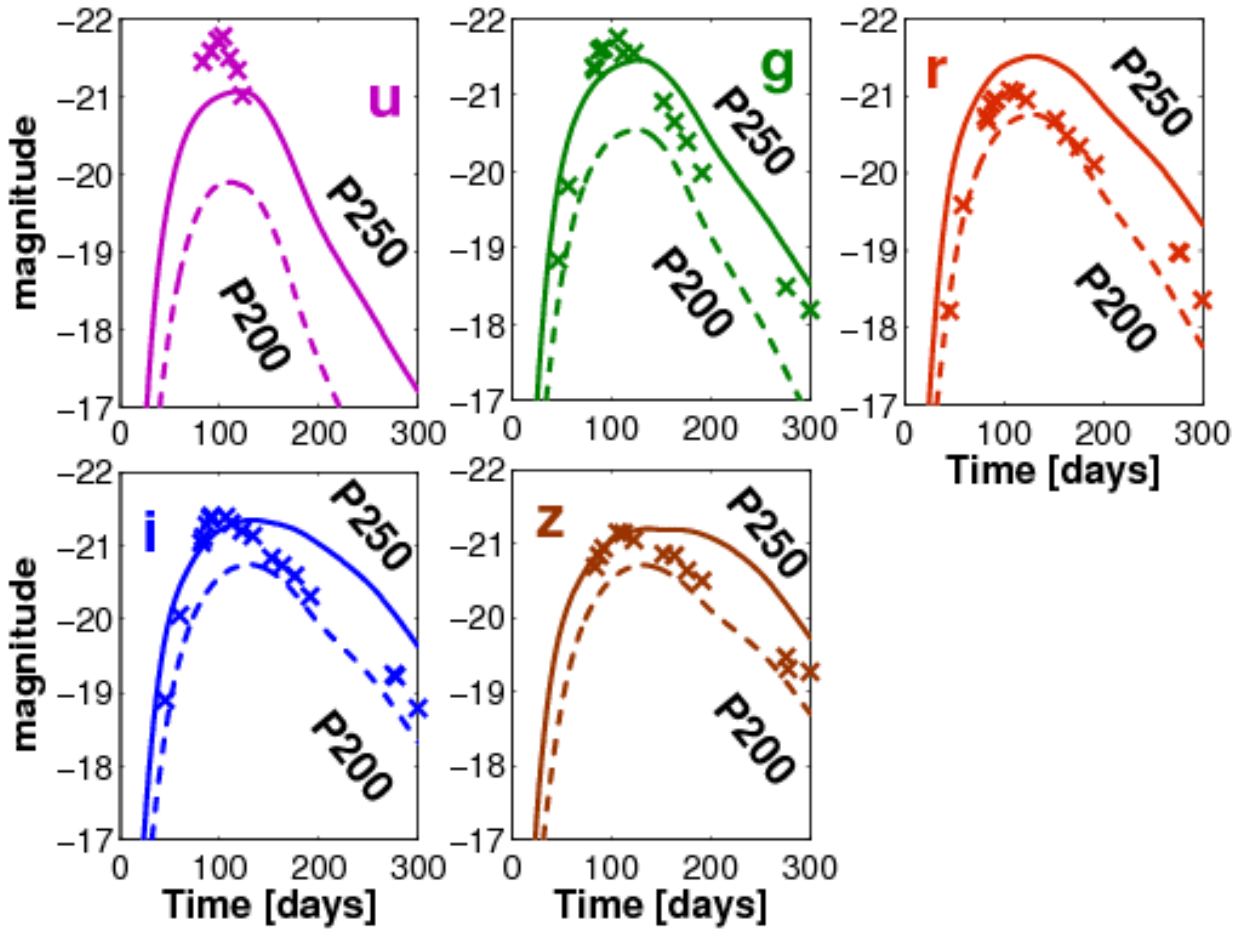

Figure 6.8 P200 (dashed) and P250 (solid) versus SLSN PTF12dam (crosses) in the *ugriz* bands. This is Figure 6 from Kozyreva et al. [Koz17].

rotation were included during the contraction and explosion phases (as in the "2.5-D" simulations by Chatzopoulos et al. [Cha14]), stronger asymmetries in the ^{56}Ni distribution would likely result.

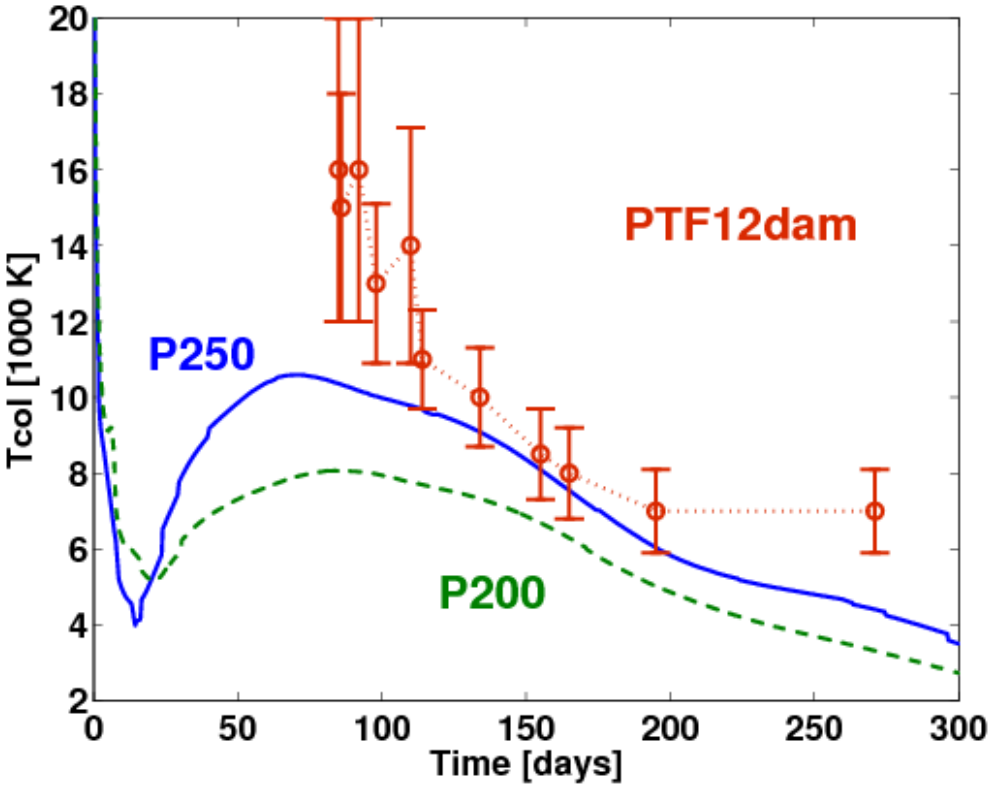

Figure 6.9 Color temperature evolution for the P200 (dashed) and P250 (solid) PISN models and that of SLSN PTF12dam (open circles). This is Figure 7 from Kozyreva et al. [Koz17].

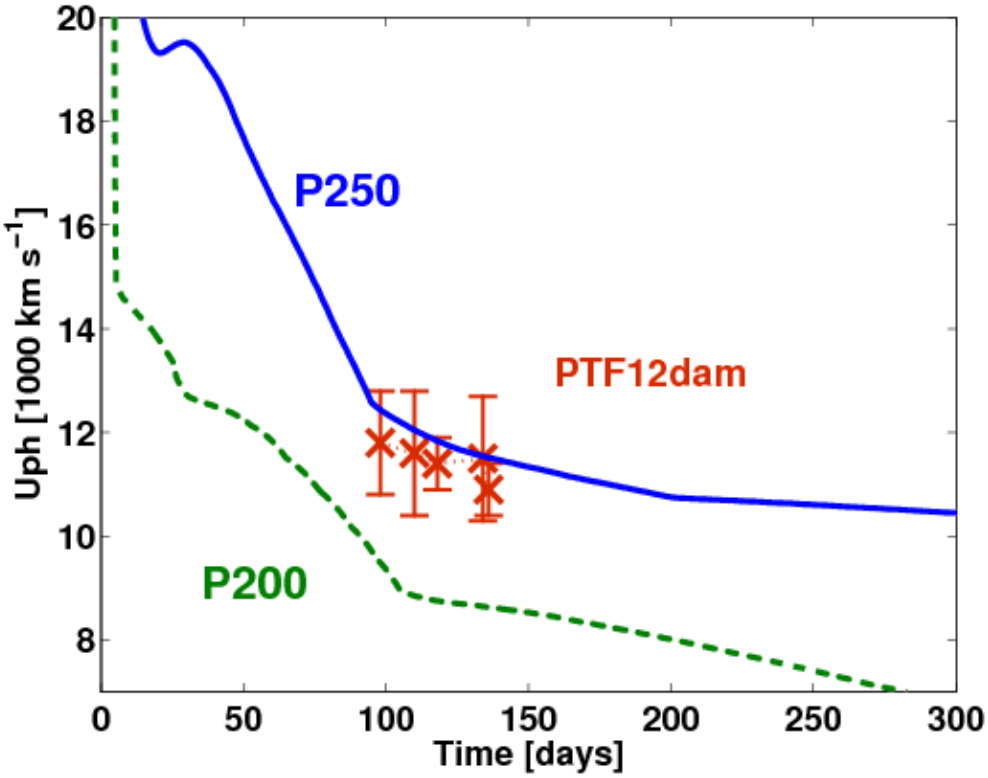

Figure 6.10 Photospheric velocity evolution for the P200 (dashed) and P250 (solid) PISN models versus PTF12dam (crosses). This is Figure 8 from Kozyreva et al. [Koz17].

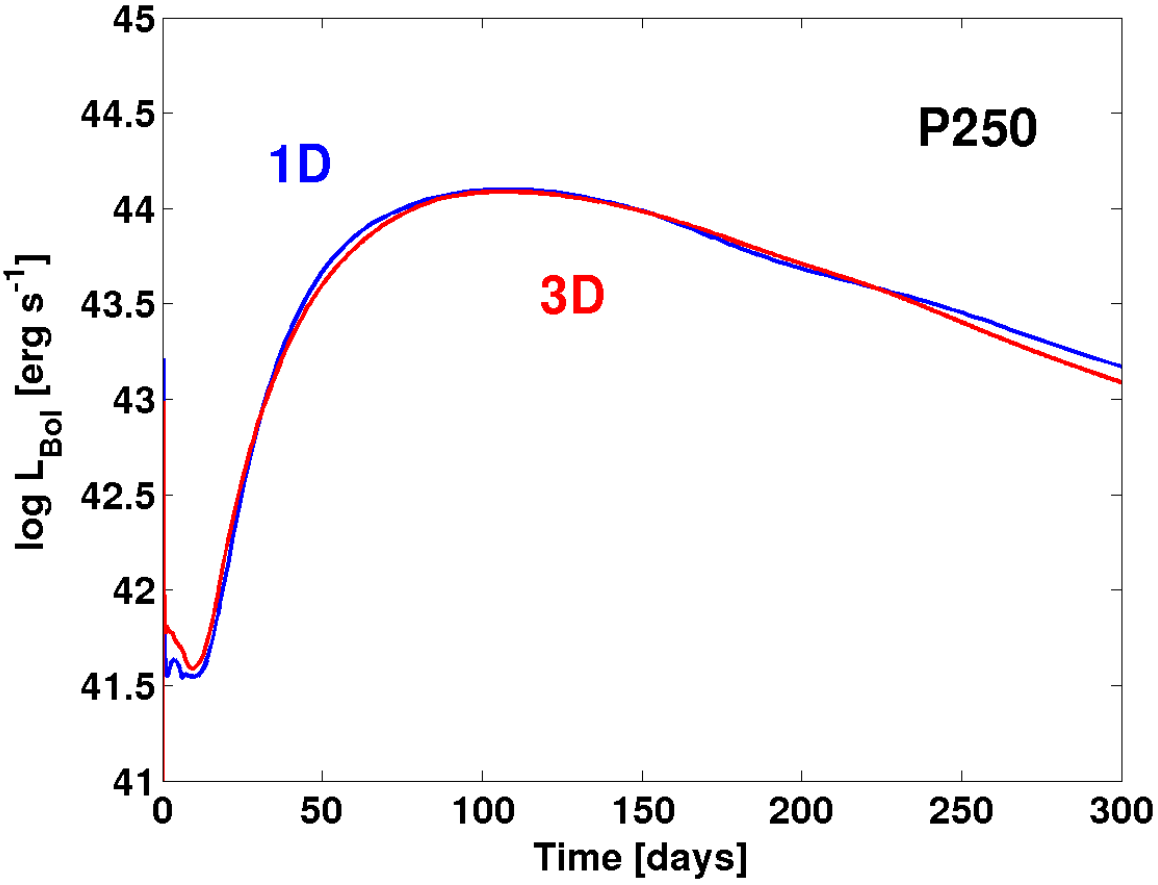

Figure 6.11 Bolometric light curves for P250 PISN models whose explosions are simulated in 1D (blue line) and 3D (red line).

6.3 Neutrino Signals

In this section we will present and discuss the results of a calculation of the neutrino signal from PISNe. For a more complete presentation we refer the reader to Wright et al. [Wri17b], from which this section has been adapted.

In Section 6.1 we discussed neutrino emission and detection from different types of SNe. We made the case that since Type Ia SNe can produce enough neutrinos to be detected by upcoming neutrino observatories at distances of a few kiloparsecs, then PISNe (being larger thermonuclear explosions) should also be similarly detectable. To motivate a calculation on this detectability, however, we need to show that the local PISN rate may be non-zero. To do this, we will first show that VMS exist in the local Universe, and then show that such stars are capable of forming carbon-oxygen cores in the necessary mass range ($64\ M_\odot < M_{CO} < 133\ M_\odot$). The second step is necessary because, with the high metallicity of the local Universe, line-driven mass loss can severely reduce the stellar mass prior to formation of the carbon-oxygen core.

Prior to recent developments in stellar evolution, it was thought that only non-rotating stars of zero metallicity (both properties reduce mass loss) with ZAMS masses in the range of $140\ M_\odot < M_{ZAMS} < 260\ M_\odot$ explode as PISNe [Heg02]. More recently, simulations have shown that stars with high initial rotation rates experience an evolution that is more chemically homogeneous. This facilitates the formation of a larger carbon-oxygen core for a given initial mass. With an initial rotation rate of 80% of Keplerian velocity, zero-metallicity stars with initial masses as low as $65\ M_\odot$ exploded as PISNe [Cha12].

Also more recently, Langer et al. [Lan07] find that stars with initial metallicities up to $Z_\odot/3$ may retain enough mass to explode as PISNe. Furthermore, recent simulations show that a sufficiently strong surface dipolar magnetic field can limit mass loss so that even stars at near-solar metallicity can explode as PISNe [Geo17]. So it seems there are still some open questions regarding the requirements for producing stars with large enough carbon-oxygen cores. Our understanding of this issue would strongly benefit from observations of PISNe and, if PISNe are indeed possible at non-zero metallicities, then we may observe a nearby event from a progenitor whose properties are well-known.

The theoretical expectation for the rate of PISNe is very uncertain because of the afore-mentioned uncertain mass loss of massive stars. The estimate by Langer et al. [Lan07] is that there is one PISN event for every 1000 SNe in the local universe. To make this estimate the authors considered only the mass range $140\ M_\odot < M_{ZAMS} < 260\ M_\odot$ and thus do not include the previously mentioned extension down to lower ZAMS masses in the presence of rapid rotation. Additionally, while they include the effects of magnetic torques on mixing, they do not consider a surface dipolar magnetic field and its effect on the mass-loss rate, as in Georgy

et al. [Geo17]. Weighing these uncertainties, we adopt a conservative lower limit for the ZAMS mass of PISN progenitors of 100 $M_\odot$, which is also the lower limit for VMS [**Vink2004**]. Many nearby stars have mass estimates exceeding this value, and some by a large margin. Several such stars exist in the Magellanic Clouds [**Kudritzki1996**]. In R136/30 Dor, twenty-three stars are estimated from models to fit the criterion, of which the most massive is estimated to be 325^{+55}_{-45} $M_\odot$ [Cro16]. This particular star greatly exceeds the previous estimates of ~ 150 $M_\odot$ for the upper limit of stars in general [Fig05], and for this particular cluster [Koe06]. Aside from the Magellanic Clouds, VMS have also been found in NGC3603 [Sch08] and near the galactic center in the Arches cluster [Mar08]. There are even a few VMS candidates within a few kpc of Earth [Gar81; Mas91; De 06; Sch09; Kas10; Cle15]. If one of these stars were to explode with enough mass left over, identifying the object as a PISN from its electromagnetic radiation alone may be non-trivial (see discussion in Section 2). However, a neutrino signal, in tandem with electromagnetic observations, may be able to unambiguously identify a PISN.

To answer this question, we perform the following calculation for models P250 and P150. Using our most and least massive models ensures that the calculated signals will approximately be the strongest and weakest signals expected for PISNe. We use data from the simulations described in Section 4.2 whose explosion results appear in Table 4.2. For each model, we calculate neutrino emission as a function of energy, time, and flavor. We then compute the flavor oscillations for the neutrino journeys through the stellar envelope and the expected event rates at various current and upcoming neutrino observatories.

We begin by calculating the neutrino emission using a similar strategy to that used by Wright et al. [Wri16] and Wright et al. [Wri17a] for the neutrino emission from Type Ia SNe. That is, we use NuLib [Ful82; Lan00; Lan03; Bur06; Oda94; Ste13; OCo10; Sul16]. We include the thermal emission process of neutrino pair production via electron-positron annihilation as well as the weak processes of electron and positron capture on protons, neutrons, and nuclei. We post-process the PISN simulations using the time evolution of the radial profiles of density, temperature, and composition. This information is incorporated into an EOS from which NuLib computes the neutrino emissivity. We calculate the emissivity for two different EOSs for comparison's sake. We use the Helmholz EOS (as in [Ito96]) whose advantage is consistency (it was the same EOS used in the original `FLASH` simulations). The disadvantage in using this EOS is that, to preserve consistency, we include only the isotopes that were included in the `FLASH` simulation (i.e. those included in the Aprox19 nuclear reaction network from Timmes & Swesty [Tim00]). Since these are the dominant isotopes, the prediction for the weak emission will not be too far off. The other EOS we employ is the SFHo EOS [Ste13]. The purpose of this EOS, which assumes Nuclear Statistical Equilibrium (NSE), is to see if the more complete isotopic network will reveal any high energy spectral features. For CCSNe, this EOS accurately describes

composition for $T > 0.5$ MeV ≈ 5.8 GK. Since this temperature value is only barely reached in our most massive (and hottest) PISN model (see Table 4.2) we restrict our calculation of the weak emission to zones where $T > 3$ GK. This limit is motivated by its success when used in the context of Type Ia SNe [Wri16; Wri17a]. Since the thermal emission is independent of composition, we relax the lower temperature limit to $T > 1.2$ GK as this is approximately the lower limit for the SFHo EOS in general [Ste13].

We present the results of the neutrino emission calculation in Figure 6.12. We set the time of maximum compression (the time where the gravitational potential energy is at its minimum) in the core of the PISN to be the zero-point ($t = 0$). This is also the time at which the neutrino luminosity is highest because the core temperature is at its highest, and as is evident from the figure, the thermal emission dominates. The duration of the neutrino signal is ~ 30 s, significantly longer than that of a Type Ia SN [Odr11; Wri16; Wri17a] or a CCSN [Tot98; Fis10]. The figure shows results from the previously discussed choices of EOS and temperature cutoff but with two additional setups. For the first setup, the Helmholz EOS is used together with a $T > 3$ GK cutoff and one in which the pair emission calculated from the SFHo EOS uses the same $T > 3$ GK cutoff as it does for the weak emission. This second additional setup captured a vast majority of signal for the P250 model so the thin red line was removed from the right side of the figure. In the case of P150, the two EOSs agree on pair emission. This is the case for the original cutoff choices ($T > 1.2$ GK for SFHo and no cutoff for Helmholz) and when both EOSs use a $T > 3$ GK cutoff. For P250, the SFHo EOS with a $T > 3$ GK cutoff results in pair emission near peak that agrees with that of the Helmholz EOS (with and without the $T > 3$ GK cutoff). Therefore, the choice of EOS is not crucial for calculating the luminosity of the dominant emission process. Nonetheless, the temperature cutoff must be chosen carefully to avoid significant errors.

For the weak emission, the situation is reversed. Here, the temperature cutoffs have very little effect but the choice of EOS is important, especially early on. Specifically, the SFHo EOS over-predicts the luminosity from weak emission. This is likely due to its assumption of NSE which effectively predicts nuclei to exist before they have actually been made. This analysis is consistent with the fact that the differences decrease with time, since at later times these nuclei will have been produced. However, since thermal processes dominate, the full neutrino signal can be computed to sufficient accuracy with either EOS if the right temperature cutoffs are chosen.

To verify that the neutrino pair-production is the dominant thermal process, and all other thermal processes need not be included, we compare the contributions of various thermal processes in a calculation using a code based on Itoh et al. [Ito96], SNEUT4[3]. Figure 6.13 shows

[3]The code is available for download at `http://cococubed.asu.edu/code_pages/nuloss.shtml`

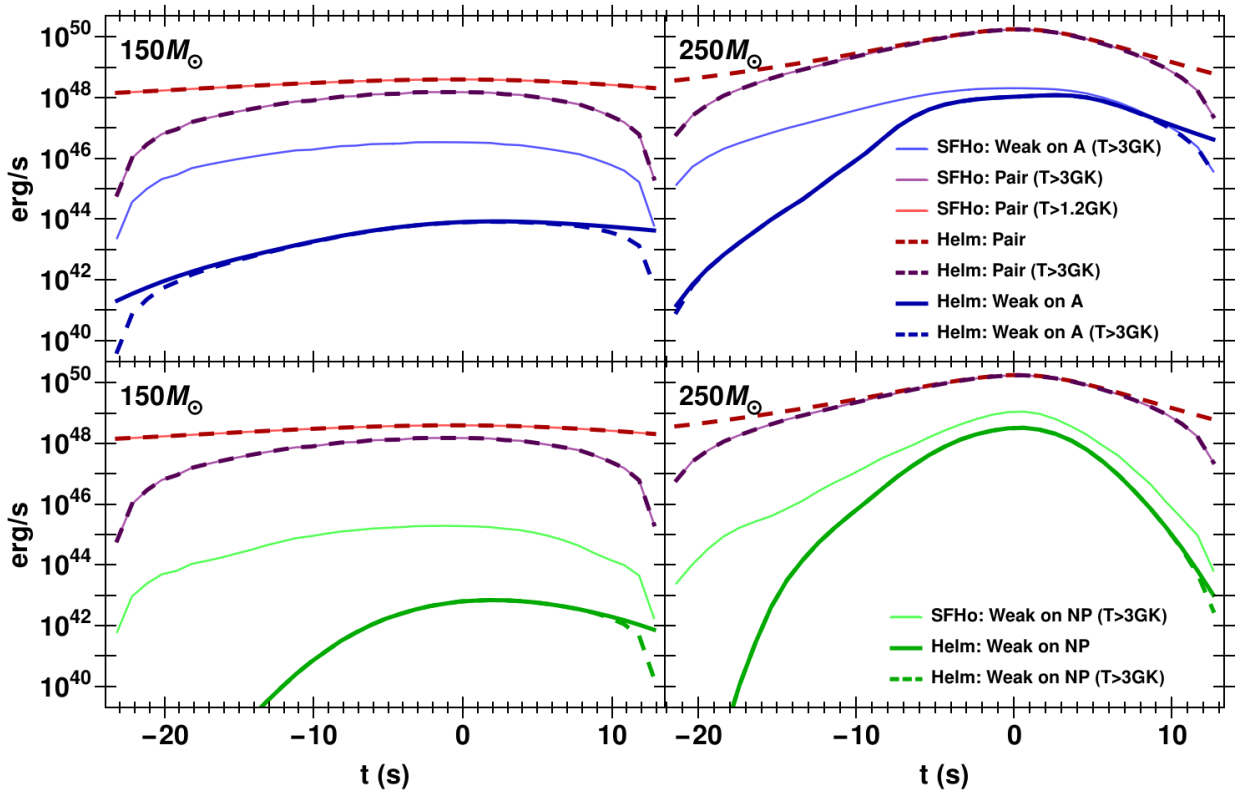

Figure 6.12 PISN total neutrino luminosity as a function of time arising from the various neutrino emission processes considered. The results for the P150 simulation are shown on the left, the P250 on the right. Emission due to pair production is shown as red and purple lines, electron capture on nuclei are the blue lines, and electron and positron capture on nucleons are the green lines. The various temperature cuts used are given in the legend. We have also calculated the weak and thermal emission using the Helmholtz EOS using temperature cutoffs in order to make a comparison although this EOS does not fail at lower temperatures in the same way as the SFHo EOS. This is Figure 1 from Wright et al. [Wri17b].

that, for P250, pair production is several order of magnitudes more important than the rest throughout the time period considered (the same is also true for P150). Therefore we can ignore all non-pair thermal processes. Additionally, as a further check on our results, we include the NuLib pair luminosity which agrees rather well with that of SNEUT4.

In Figure 6.14 we present the neutrino spectra near maximum compression (and emission) from the NuLib calculation. We include results using both EOSs and for both PISN models. The spectra follow closely the expectation from purely thermal emission for all neutrino flavors with the exception of ν_e and $\bar{\nu}_e$. For these flavors, the flux across all energies is enhanced due to weak processes. Additionally, for the ν_e, the use of the SFHo EOS reveals a spectral feature at 10 MeV. We interpret this feature to be mainly due to electron capture on copper (see Wright et al. [Wri16] and Wright et al. [Wri17a]). This feature is present throughout the signal duration.

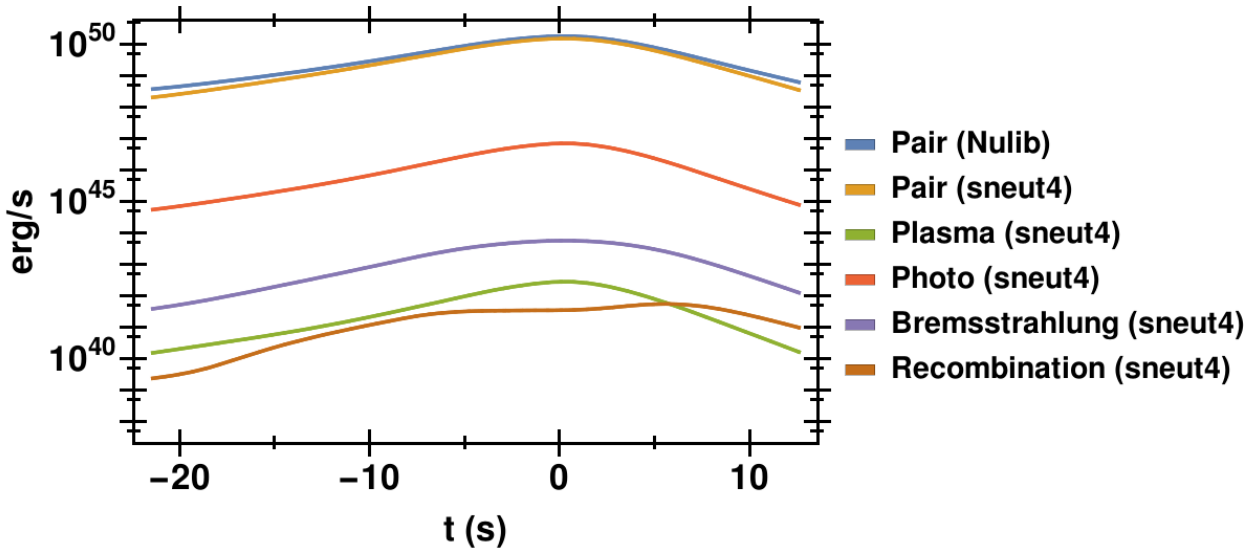

Figure 6.13 PISN total neutrino luminosity for thermal processes for the P250 simulation. The different thermal processes are color coded as per the legend and the code used to generate each is given in parentheses. The calculation assumes the Helmholtz EOS for all processes. The "Pair (Nulib)" line is a reproduction of the "Helm: Pair" line from Fig. 6.12. This is Figure 2 from Wright et al. [Wri17b].

The feature, however, may not be present at all times in reality due to the EOS's assumption of NSE which is less valid at early times.

Figure 6.14 also includes a gray region which represents the spectra (from the calculation using the SFHo EOS) at $t = 12.6$ s. This is included to represent the evolution of the spectra in time. There is little change in the shape as the flux increases then decreases, while the thermal peak slightly shifts to higher then lower energies. This result is in contrast to the behavior seen for Type Ia SNe, in which the thermal peak shifted to lower energies faster due to faster cooling of the emitting regions.

Since our goal is to predict how the signal will look when it reaches Earth, we account for neutrino oscillations during its journey. This journey includes both the propagation of neutrinos through the SN ejecta and across the vacuum of space to Earth. We use the same calculation strategy as in Wright et al. [Wri16] and Wright et al. [Wri17a].

To this end we solve the Schrödinger equation for the evolution matrix. The Hamiltonian drives the oscillations and includes a vacuum term, a matter term, and a self-interaction term. Transition probabilities are calculated from the solution of the evolution matrix. The equation can be solved in either the flavor or the matter basis (often termed the mass basis in vacuum) [Bet86]. One can switch between the two bases with a mixing matrix which contains three mixing angles (θ_{12}, θ_{23} and θ_{13}) and a CP-violating phase δ_{CP}. The squared neutrino masses go

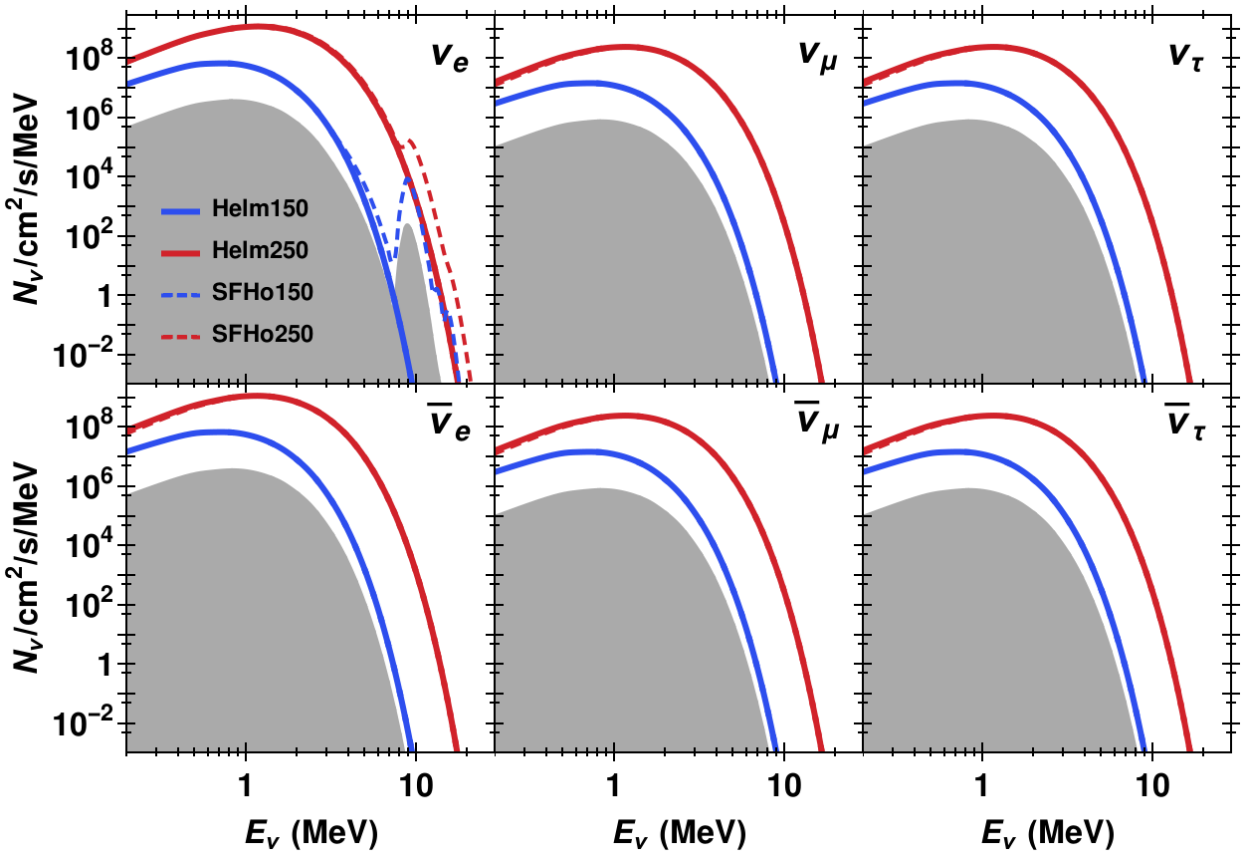

Figure 6.14 PISN neutrino flux spectra. Each curve is the sum of all considered weak and thermal processes at the time slice nearest maximum emission. The gray region is the spectra from the SFHo, P250 results at $t = 12.6$ s. This is Figure 3 in Wright et al. [Wri17b].

into the Hamiltonian. We adopt the following values given in Table 6.1 for these parameters.

Table 6.1 Adopted values for neutrino oscillation parameters.

$m_2^2 - m_1^2$	$\lvert m_3^2 - m_2^2 \rvert$	θ_{12}	θ_{13}	θ_{23}	δ_{CP}
7.5×10^{-5}eV^2	2.32×10^{-3}eV^2	33.9°	9°	45°	0

Since the sign of $m_3^2 - m_2^2$ is unknown, two mass orderings are possible. These are known as the normal mass ordering (NMO) (which assumes $m_3^2 - m_2^2 > 0$) and the inverted mass ordering (IMO) (which assumes $m_3^2 - m_2^2 < 0$). For the oscillation of neutrinos as they traverse the stellar mantle, we include both the vacuum and the matter terms in the Hamiltonian but not the self-interaction term as its effect was found to be negligible. After the neutrinos have exited the star, only the vacuum term is needed. The details of this formalism and a calculation showing

neutrino self-interaction can be ignored are included in Wright et al. [Wri17b].

We continue now to discuss the oscillations that occur as the neutrinos travel through the stellar mantle. Here, the matter term of the Hamiltonian is extremely important. This added term introduces a dependence on the material density and its electron fraction (which sits very close to 0.5 for the signal duration). Figure 6.15 shows the density profile of the PISN ejecta at four times. Two of the times chosen are the beginning and end of the signal, one is near maximum compression (and emission), and one is chosen to be the time by which a clear shock has developed ($t \approx -5.4$ for P250 and $t \approx 6.8$ for P150). Also visible on the plot are the densities at which 1 MeV neutrinos experience two Mikheyev-Smirnov-Wolfenstein (MSW) resonances (high and low). These densities are calculated using the 2-flavor approximation (see Wright et al. [Wri17b]). At the times when the shock crosses the resonances there are significant oscillation effects [Par86]. These effects are strong for P250, as we shall see. For P150, however, since the shock forms past the high MSW resonance and only crosses the low MSW resonance after the signal has decreased significantly, the effects are weak.

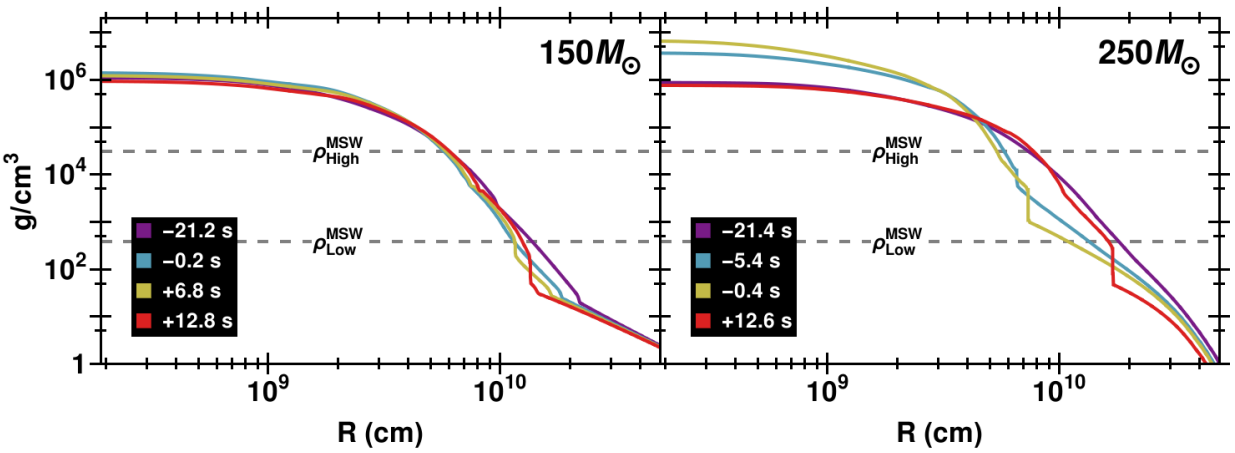

Figure 6.15 Density profiles for various time slices for P150 (left) and for P250 (right). The two horizontal dashed lines are the 2-flavor MSW densities for 1 MeV neutrinos. This is Figure 4 in Wright et al. [Wri17b].

We calculate the neutrino transformation probabilities occurring within the star in the matter basis (see Wright et al. [Wri17b] for more details along with figures showing the results of the calculation). We then account for vacuum oscillations and the associated decoherence of the neutrino wavepacket [Giu98] to arrive at probabilities $p_{\alpha\beta}$ that a neutrino emitted as flavor β at the source will be detected as flavor α at Earth. The electron neutrino and antineutrino survival probabilities (p_{ee} and $\bar{p}_{ee}$) for both models and both mass orderings are plotted as a

function of energy in Figure 6.16. In general, the oscillations are detrimental to the survival of the dominant flavor (at emission) of neutrinos and antineutrinos (the electron flavor). However, the passage of the shock through the high MSW resonance aids p_{ee} for the NMO and $\bar{p}_{ee}$ for the IMO. The low MSW resonances effect is considerably weaker but is visible in the p_{ee} for the IMO. Lastly, the effects of the MSW resonances are much more pronounced for P250 than for P150 for the reasons discussed in the last paragraph.

Next we calculate the energy-dependent flux for each of the six neutrino flavors by combining the previously calculated emission spectra and flavor transformation probabilities along with the usual attenuation with distance. For the following figures and tables we set the distance to the PISN to be 10 kpc. We present the neutrino flux spectra at Earth for the time of maximum compression (and emission) for both mass orderings in Figure 6.17. To see the aggregate effects of the neutrino oscillations, on should compare this figure with Figure 6.14. Due to oscillations, the previously discussed spectral feature at 10 MeV has propagated to mu and tau neutrino flavors. Additionally, the excess in electron flavor neutrinos compared to the other flavors in Figure 6.14 is no longer present.

Finally we compute what neutrino observatories will see for a signal characterized by our previous calculations. For this we use the software package SNOwGLoBES. We consider five different detectors whose type and mass are given in Table 6.2. We stress that the detector models are approximate, which is indicated by the use of the word "type" in the table. This is unavoidable since complete detector descriptions for the current detectors are not openly available. For the planned detectors, a complete description has not even been finalized. Also, since detector thresholds are unknown for the planned detectors, we do not include them for any of the detectors for consistency. However, a 0.5 MeV threshold is present from the calculation. Similarly to the detector descriptions and thresholds, we do not know all of the detector's efficiencies. So, to preserve our consistent analysis, we optimistically assume that the neutrino energies are perfectly reconstructed.

Table 6.2 A summary of the detector types. * Assuming 30% phototube coverage, see SNOwGLoBES documentation for discussion on phototube coverage. † For IceCube, the mass given is the 'effective' mass. This is Table I in Wright et al. [Wri17b].

Detector	**Type**	**Mass (kt)**
Super-Kamiokande type [Fuk03] *	Water Cherenkov	50
Hyper-Kamiokande type [16]	Water Cherenkov	374
DUNE type detector [Acc16]	Liquid Ar	40
JUNO type detector [An16]	Scintillator	20
IceCube [Abb11]	Water Cherenkov	3500†

Table 6.3 Numbers of interactions per detector for each mass ordering and a PISN at 10 kpc. These event counts are for the whole neutrino burst. The last two columns represents the number of interactions observed when neutrino oscillations are not taken into account. This is Table II in Wright et al. [Wri17b].

Mass	**Detector**	**NMO**		**IMO**		**Unoscillated**	
		Helm	SFHo	Helm	SFHo	Helm	SFHo
P150	Hyper-Kamiokande	1.77	1.78	1.74	1.75	3.02	3.05
	Super-Kamiokande	0.24	0.24	0.23	0.23	0.40	0.41
	DUNE	0.14	0.14	0.15	0.15	0.25	0.25
	JUNO	0.10	0.10	0.10	0.10	0.17	0.17
P250	Hyper-Kamiokande	52.23	50.08	43.32	41.98	85.70	84.19
	Super-Kamiokande	6.98	6.69	5.79	5.61	11.46	11.26
	DUNE	2.95	2.78	3.17	3.06	5.30	5.20
	JUNO	3.13	3.00	2.48	2.40	5.06	4.97

In Table 6.3 we present the expected event counts for the detectors listed in Table 6.2, with the exception of IceCube, for both models, mass orderings, and EOSs (for which the differences are small). To further highlight the effects of oscillations we also include the unoscillated event counts. The overall counts for the P250 case sits about three orders of magnitude below those for a CCSN occurring at the same distance of 10 kpc [Mir15]. However, the signal is still about two orders of magnitude stronger than that expected for a Type Ia SN [Odr11; Wri16; Wri17a]. For P150, whose signal is approximately the weakest possible neutrino signal from a PISN, the signal is $\sim$ few times stronger than that expected for Type Ia SN and would just barely be detected at a distance of 10 kpc. The effect of neutrino oscillations on the expected event rate is largely negative owing to the fact that the electron flavor neutrinos (whose survival probability was severely hampered by oscillations) are the neutrinos that the detectors are most sensitive to. The choice of the mass ordering also affects the expected event counts. The NMO predicts more events than the IMO for Super-Kamiokande (SK), Hyper-Kamiokande (HK), and JUNO. However, for DUNE, the IMO predicts more events than the NMO. This can be explained by noting that DUNE is the only detector of the four not sensitive to inverse beta decays (which are caused by the scattering of $\bar{\nu}_e$s off protons) together with the observation that the flux of $\bar{\nu}_e$s is about an order of magnitude higher for the NMO than for the IMO (see again Figure 6.17). Irrespective of mass ordering, however, the event counts are high enough to distinguish a PISN from a Type Ia SNe or a CCSNe. The PISN signal would be characterized by an event rate that rises to peak over $\sim$ 15 seconds whereas a CCSN signal would peak almost immediately after core bounce [Fis10]. The sheer timescale of the neutrino emission in PISNe ($\sim$ 30 s) would rule out a Type Ia SN origin for the signal which lasts for less than $\sim$ 5 s [Odr11; Wri16; Wri17a].

The time structure of the signal, which we have shown is distinct from those of Type Ia SNe and CCSNe based only on the signal duration and time of peak, is shown in detail in Figure 6.18.

The shape of the signal is Gaussian-like and weakly dependent on the choice of EOS. For P250 and assuming the NMO (IMO), HK can expect about 5 (4) events per second at the signal peak. For P150, the signal is much weaker and the shape resembles a much shallower Gaussian.

We also present the energy structure of the neutrino signal in Figure 6.19. Evident in the figure is the double-peaked structure seen in the NMO for P250 (except in the spectrum for DUNE). The second peak in this structure (which is suppressed in the IMO) is centered around 2-3 MeV and is due to the contribution to the event rate from inverse beta decays (which is missed by DUNE). The fact that the peak shows up for the NMO and not the IMO (due to the larger flux of electron antineutrinos predicted for NMO) means that the detection of a PISN neutrino signal could constrain the neutrino mass ordering, which is very exciting.

Finally, we discuss the sensitivity of IceCube (the last detector listed in Table 6.2) to the neutrino signal. Unlike the other detectors, IceCube will not be able to provide directional or spectral information for its detections. Instead, the signal would manifest only in the background of low-energy neutrinos. Therefore, the signal must be strong enough to add a statistically significant excess over the background to be detected. For P250 (P150), this requirement roughly translates to a maximum detection distance of 1 kpc (70 pc). The likelihood of massive enough stars existing in this tiny neighborhood is extremely low.

To conclude this section we note that an even stronger neutrino source than a high-mass PISN would be a direct-collapse black hole triggered by the PI (also possibly a strong gravitational wave source (see Section 6.1). One would have to perform the calculation to learn exactly what the signal would look like but we can be sure that the core (whose contraction is reversed by nuclear burning in PISNe) would accelerate in its collapse and rapidly increase in temperature. The thermal emission of neutrino pairs would therefore ramp up as well. The collapsing core would also be rapidly increasing in density and would soon reach neutrino trapping densities. We predict then that the signal would exhibit an exponential rise in emissivity followed by a sharp cut-off. The time variability of such an event would easily distinguish it from any of the SN sources which we have discussed (PISN, Type Ia SN, and CCSN). Since this requires a higher mass progenitor, it is even less likely to occur than a high-mass PISN (especially in the local universe). However, the signal would be visible out to a larger distance.

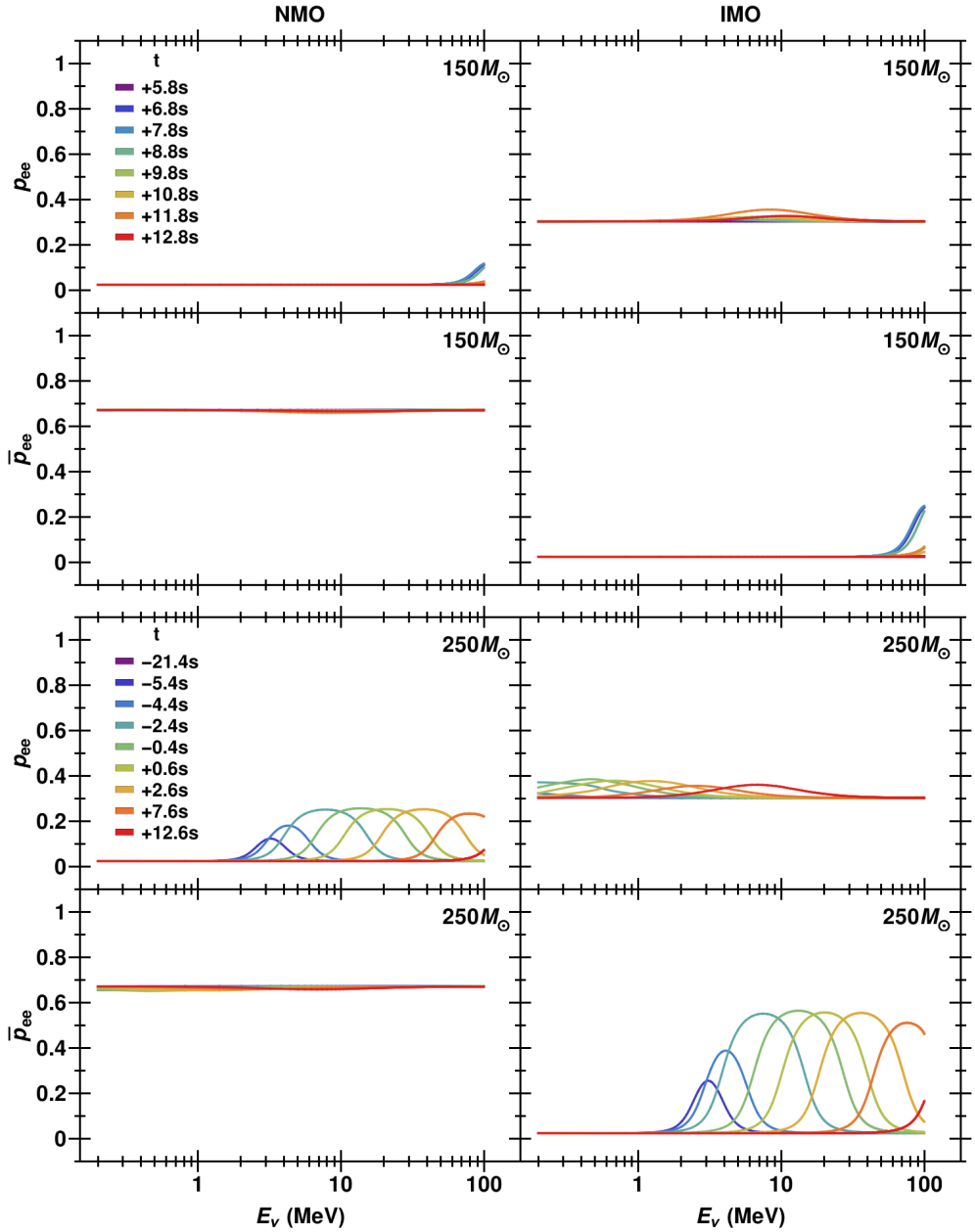

Figure 6.16 p_{ee} for neutrinos and $\bar{p}_{ee}$ for antineutrinos for both mass orderings. The time slices chosen are representative of when oscillation features occur. The top four subplots are for the P150 simulation and the bottom four subplots are for the P250 simulation. This is Figure 8 from Wright et al. [Wri17b].

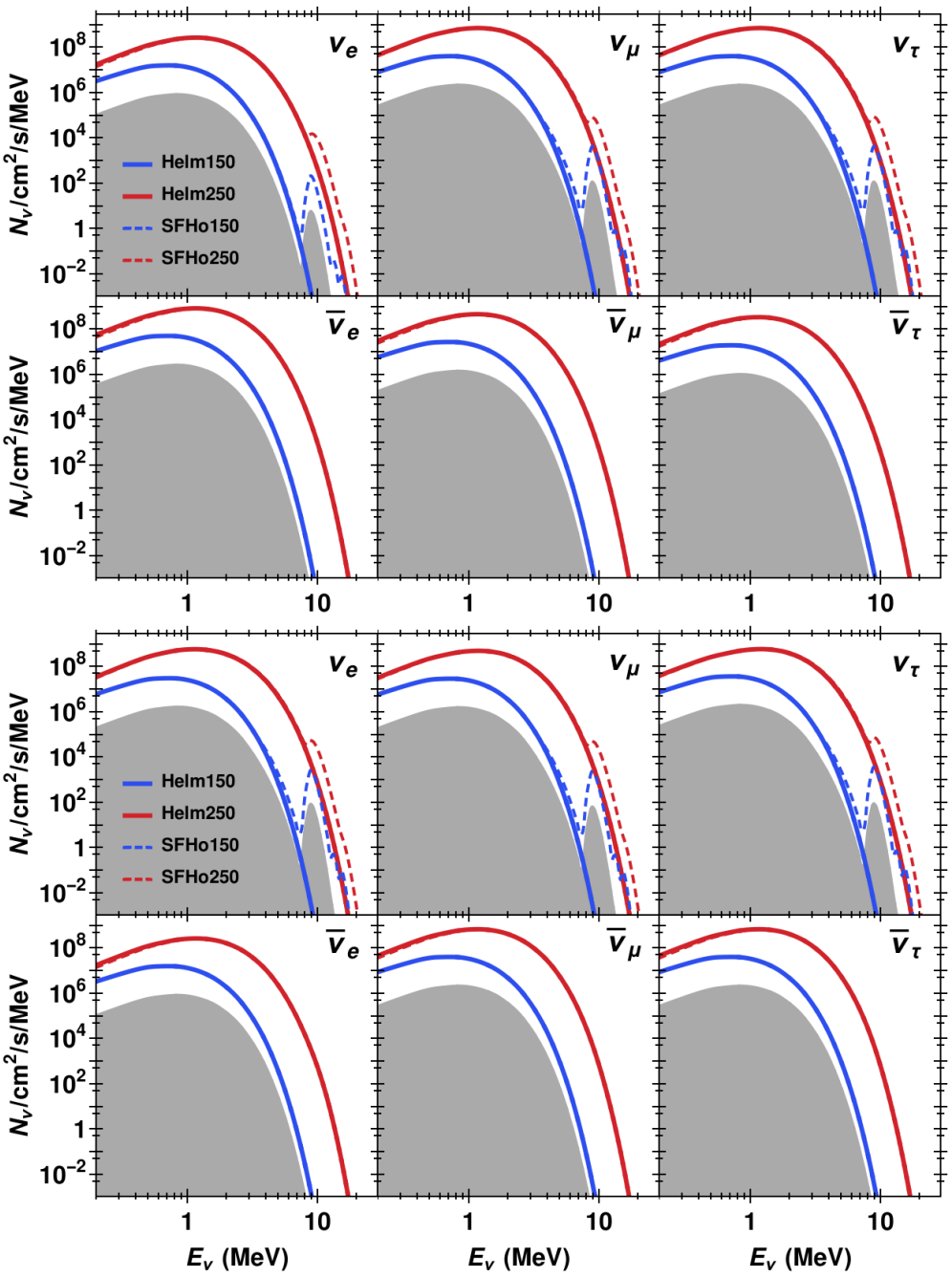

Figure 6.17 Total oscillated neutrino flux from a PISN at 10 kpc. Each curve is the sum of all considered weak and thermal processes at the time slice nearest maximum emission. The top subplot is for NMO and the bottom subplot represents IMO. The gray region is the spectra from the SFHo, P250 results at $t = 12.6$ s. This is Figure 9 from Wright et al. [Wri17b].

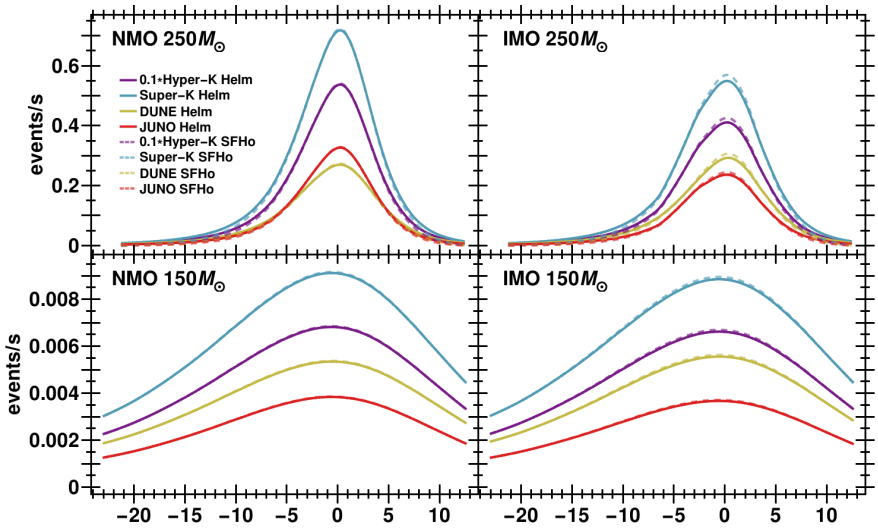

Figure 6.18 Detector interaction event rate from a PISN at 10 kpc (event rates scale inversely to the square of the distance). The left (right) plots are for NMO (IMO) and the top (bottom) plots are for P250 (P150). The purple line representing the event rate in HK has been rescaled to a tenth of its proper value for plotting convenience. This is Figure 10 in Wright et al. [Wri17b].

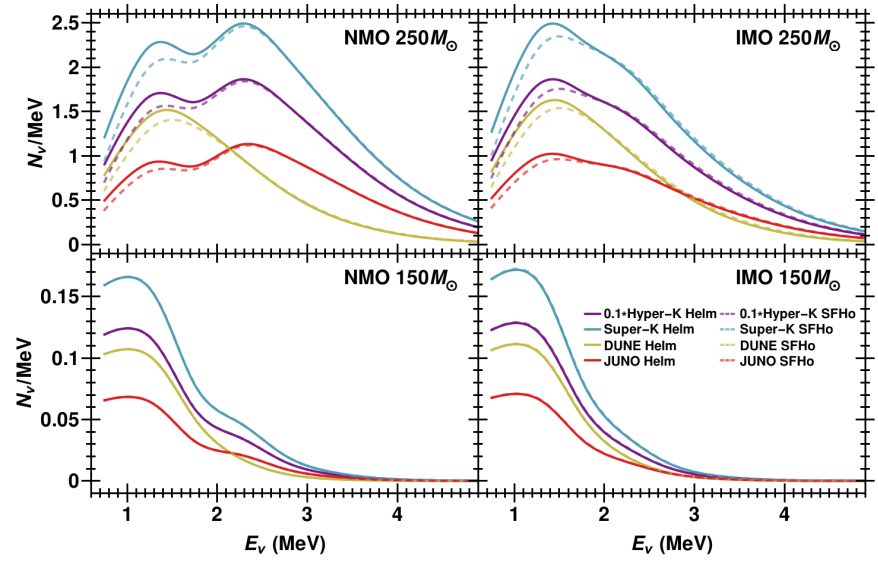

Figure 6.19 Detector interaction event differential spectrum. Event count is the total for the whole neutrino burst. The left (right) plots are for NMO (IMO) and the top (bottom) plots are for P250 (P150). The purple line representing the event rate in HK in the bottom plot has been rescaled to a tenth of its proper value for plotting convenience. This is Figure 11 from Wright et al. [Wri17b].

6.4 Light Curves and Spectra with SuperNu

In this section we discuss the motivation and first steps taken, along with some future plans, for computing spectra from our multi-dimensional PISN simulations. For this we use the radiation transport code SuperNu [Wol13; Wol14]. While it does not have the hydrodynamic coupling between matter and radiation included in STELLA, it has the ability to compute synthetic spectra and can simulate in 2D and 3D. Without the hydrodynamic coupling there is no momentum transfer between radiation and matter. However, radiation does affect the temperature of the matter. This approximation is valid after sufficient time has passed since the SN explosion when the ejecta are expanding homologously. The code applies the Implicit Monte Carlo (IMC; Fleck & Cummings [Fle71]) and the Discrete Diffusion Monte Carlo (DDMC; Densmore et al. [Den07]) methods to solve the radiative transport equations.

With this code, we aim to compute spectra at all epochs of the SN. We will attempt to identify any identifiable spectral features that result from the mixing in the ejecta (particularly that near the Si-O interface). We expect modifications to the OI absorption feature at ~ 6200 , in particular (see Figure 8 in Chatzopoulos et al. [Cha15]), due to the spreading of oxygen through a wider range of velocities than in the 1D case. However, many other lines may be affected due to the same spreading in velocity of oxygen, silicon, and sulfur. We plan to eventually simulate in 2D and 3D to assess any viewing angle dependence. To begin, we will use angular-averaged profiles from the multidimensional FLASH simulations as input for 1D SuperNu simulations.

In order to do this, there is one extra step in this calculation that is required. This is because the temperatures that exist at the end of the FLASH simulations are higher than can be accommodated as input by SuperNu. For P250, the model for which we explored mixing in high resolution, the final temperature in the core is $\sim 9 \times 10^8$ K, while the opacity calculations in SuperNu are only reliable for $3 \lesssim \log(T) \lesssim 5$. Our chosen method to attack this issue is to run to later times in FLASH. For this, we need to go beyond SBO by including a stellar wind profile outside the stellar atmosphere for the shock to expand into. Such a wind is presumed to exist outside stars due to their mass loss. Here, we similarly truncate the profile to avoid the shock velocity exceeding the speed of light as in Section 6.2 We set the density profile for this wind to scale with $1/r^2$ and the temperature of this wind to be flat at 10^3 K. However, due to computational difficulties, this approach can not reliably evolve until the ejecta have sufficiently cooled. We encounter numerical problems in the FLASH simulations of unknown origin after the central temperature had cooled to below 4×10^6 K (~ 6300 s after SBO). This is still more than an order of magnitude higher than the target maximum temperature.

In order to reach this target maximum temperature, we temporarily use the code SNEC to simulate this cooling phase, although in the end this phase will be simulated with FLASH. SNEC

is a 1D Lagrangian radiation-hydrodynamics code which can accurately compute bolometric LCs (which will help with code comparisons) and is described in detail by Morozova et al. [Mor15]. After the ejecta have sufficiently cooled, we map the profile into SuperNu to compute spectra and LCs. We show a comparison of the LC calculated from the high-resolution 1D FLASH simulation with STELLA and those calculated from the angular-averaged profiles of the 2D and 3D high-resolution FLASH simulations. We first note that LCs calculated by SuperNu are almost identical. This is expected because they were both computed with the same codes and, although we found greater mixing at the Si-O interface in 3D than in 2D, only mixing of nickel is expected to affect LCs. We also note that SBO is caught only by STELLA because the SuperNu calculations required significant evolution after SBO to allow time to cool. Finally, we note that the peak bolometric luminosities are similar, but the rise times differ by about 50 days. This is probably due to the differing treatment of opacities between the two codes.

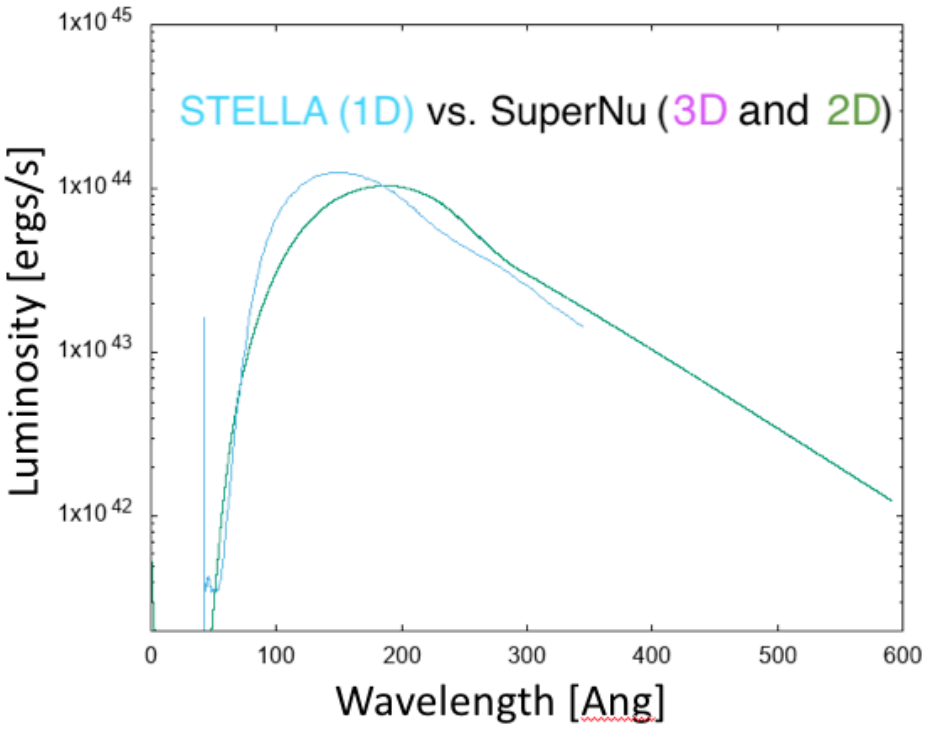

Figure 6.20 Bolometric light curves for P250 PISN model computed from the 1D FLASH profile with STELLA (cyan) and from the 3D (magenta) and 2D (green) angular-averaged FLASH profiles (extended with SNEC) with SuperNu.

We would also like to test the difference from simulating the cooling phase with FLASH and SNEC. Note that the former approach is not quite reliable; however, the opacities should

still be approximately captured. We present such a comparison of the spectra near peak luminosity in Figure 6.21. We note that we used differing FLASH explosion profiles (1D and 3D angular-averaged) but these differences are likely to be subtle since mixing was not particularly strong. We find that these spectra are largely similar, though the spectrum from simulating the cooling phase with FLASH seems to underestimate the extent of some absorption and emission features. We plan to solve the numerical problem encountered in FLASH and evolve to lower temperatures in order to isolate the differences from using FLASH versus SNEC.

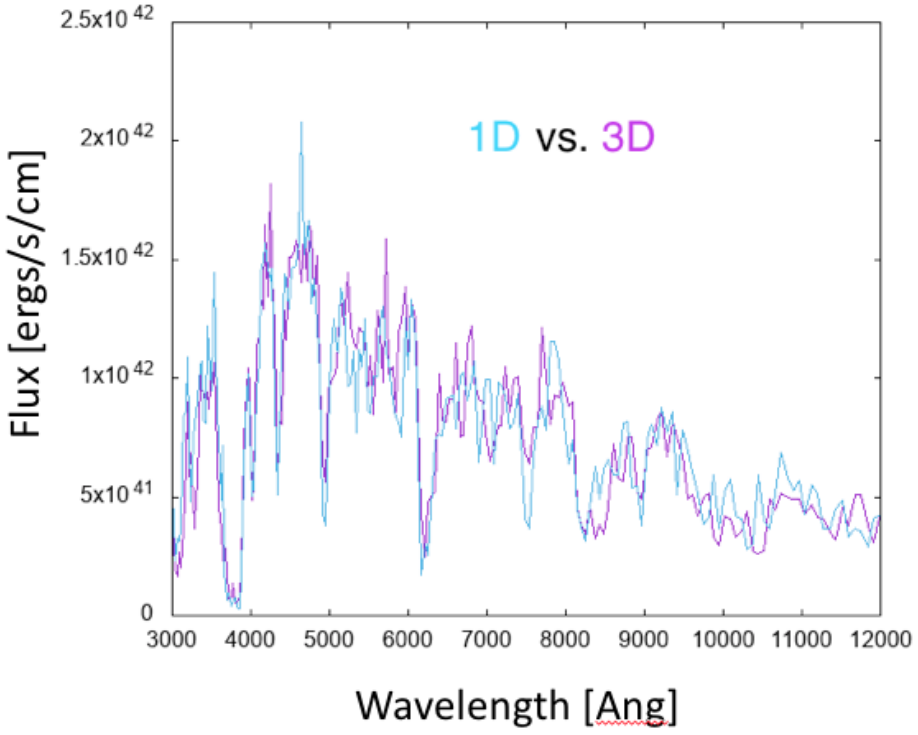

Figure 6.21 Synthetic spectra near peak light for the P250 PISN model computed from the 1D FLASH profile extended with FLASH (cyan) and the 3D angular-averaged FLASH profile extended with SNEC (magenta)

In order to perform SuperNu simulations in multiple dimensions, we will need to provide a multidimensional input profile. While one could input a spherically-symmetric initial state from angular-averaged profiles cooled via a 1D FLASH simulation, we would lose any information that would provide viewing-angle dependence. Therefore, we need to extend the multidimensional evolution described in Chapter 5 throughout the cooling phase. Since we are interested in the spectral consequences of chemical mixing in the ejecta, we will need to take care to preserve (and follow the continued instability growth of) the structure of the final states

from the original multidimensional simulations. Additionally, we cannot allow any crossing of refinement boundaries by these mixing features (recall that this causes spurious mixing as shown in Figure 5.1). We have formulated the following procedure to meet these requirements. We will describe the procedure for 2D simulations, but the method is easily extendable to 3D.

We begin with the final profile of the high resolution 2D simulation (before the angular-average and subsequent appending of the envelope). We map this 2D profile onto a larger 2D grid that has a nested structure like those described in Section 5.2. Here, the highest level of refinement (with resolution $(3.25 \times 10^7$ cm) again occupies the central half square which now extends to 3.75×10^{10} cm in the x-direction (instead of the 1.00×10^{10} cm of the original simulation). Outside of this half square is a drop in refinement of one level, followed by further drops in refinement where each subsequent half square has twice the extent in the x-direction as the previous one. We run until the region of interest approaches the first refinement boundary (ensuring the shock wave has not reached any domain boundary).

Thus, the effective resolution (number of zones across the interface) of the region of interest (the Si-O interface) actually increases as the radius of this interface increases by a factor of ~ 4. We then map onto a new, larger, grid that follows the same pattern of nested half-squares. The data from the previous simulation (interior to a radius equal to the extent of the domain of the previous simulation in the x-direction) is mapped exactly from the checkpoint file to the same physical space which constitutes an inner region of the new simulation. The space outside this circle is either filled using the spherical wind parameters (as in our 1D `FLASH` ejecta cooling simulations) or from the spherically-symmetric `GENEC` model while densities and temperatures are set for a modified region to deal with discontinuities as described in Section 6.2.

Next, before any significant evolution in the new simulation, we derefine the inner half-square of the highest refinement level to equal that of the next half square. This is the region that will contain the region of interest. As its effective resolution had increased by $\sim 4\times$, we can afford to derefine in this region (decreasing the effective resolution by a factor of 2). We then run until the region of interest approaches the boundary of what has now become the inner half square. We repeat this process until the ejecta have cooled sufficiently. Forcing each subsequent half-square to have twice the extent in the x-direction as the previous one guarantees that the effective resolution (i.e. the number of spatial zones over mass coordinate) for all parts of the star will stay above the initial value. In the region of interest, this initial value is higher than it was at the end of the original 2D simulation. Thus we are effectively following instability growth at an even better level of accuracy. Furthermore, the process of derefining the inner region after each re-mapping continually increases the time step. This, together with the hierarchical grid structures, make the method extremely computationally efficient despite having to model

out to ~ 10 days.

This method is depicted in Figure 6.22 where we present the grid structure over a density color map at the beginning of the second additional 2D simulation (described above). Derefinement of the inner half square is barely visible between the two panels. For this simulation, as in Figure 5.1, the blocks represent AMR blocks. However, this time the blocks are 192x192 computational cells. The block size was increased to improve the visibility of the grid structure for these plots. While one can easily see the hierarchical structure of the grid, the block lines become very crowded towards the center. In Figure 6.23 we present a zoomed-in view of the same data. In this figure, anisotropies in the density profile are visible and preserved through the derefinement step. Finally, we present an even more zoomed-in view showing the ^{28}Si mass fraction in Figure 6.24. From this figure two important points are evident. First, the left panel shows that the previous simulation saw the RT instabilities grow to larger-scale plumes (compare with Figure 5.3). This is consistent with our analysis that suggested the difference between 2D and 3D was the speed of RT growth. We see similar features eventually develop when followed with sufficient resolution. Second, these new features are adequately preserved after derefinement, and this is clear from the right panel of Figure 6.24.

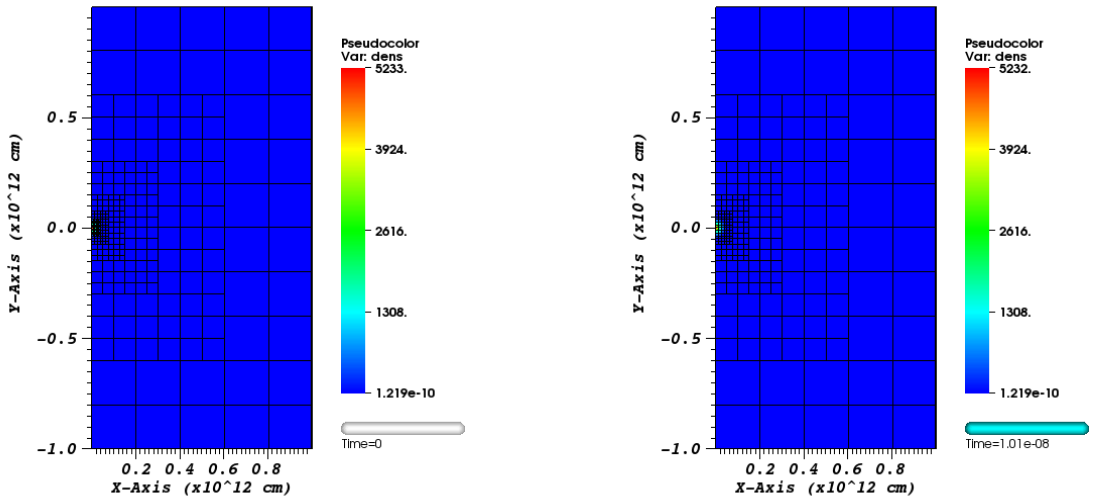

Figure 6.22 Pseudocolor of density on a log-scale overlaid on top of the grid structure pre-derefinement (left) and post-derefinement (right). The boxes correspond to AMR blocks of 192x192 cells each.

In addition to the further advanced mixing at the Si-O layer, which has now frozen out in mass coordinate, we find a new RT instability that develops behind the shock following SBO.

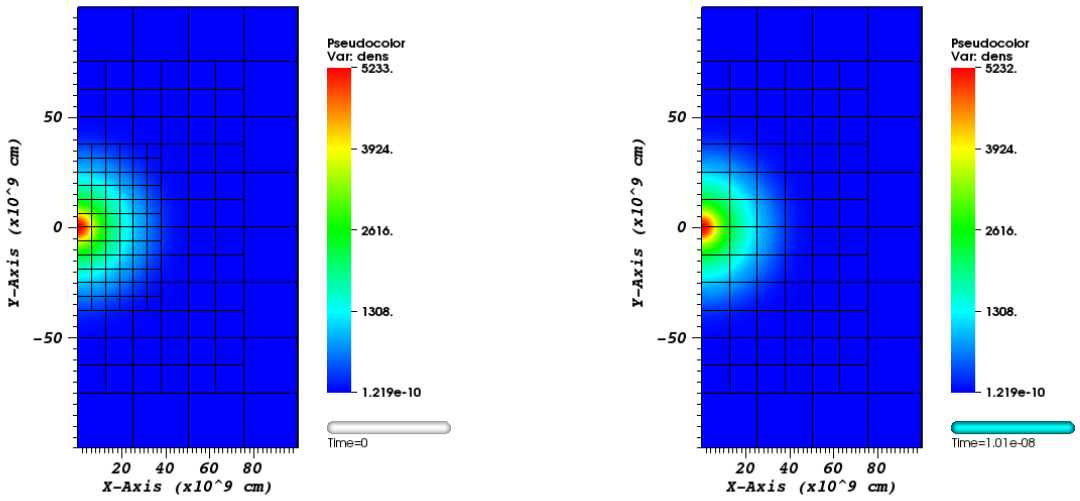

Figure 6.23 Zoomed-in pseudocolor of density on a log-scale overlaid on top of the grid structure pre-derefinement (left) and post-derefinement (right). The boxes correspond to AMR blocks of 192x192 cells each.

This is visible in the density pseudocolor shown in Figure 6.25. These features have continued to grow up until this point. A zoomed-in view of a characteristic RT mushroom is provided in Figure 6.26. The overdensities are on the order of ~ 10. These features are similar to those that formed from a reverse shock after the forward shock crosses into the hydrogen envelope in the simulations of Chen et al. [Che14a] (see their Figure 11). They also find overdensities on the order of ~ 10. For our simulations, the composition is uniform in this region so the instability is not expected to have spectral consequences, but is interesting nonetheless. We conclude this section by noting that the computational resources required for each subsequent simulation (in which we increase the grid size by a factor of ~ 100) are only marginally higher than those required for the last. Overall, we estimate that simulating until temperatures cool sufficiently will take on the order of ~ 10 times more CPU hours than the original 2D simulation from Chapter 5. Therefore, this approach is likely feasible in 3D.

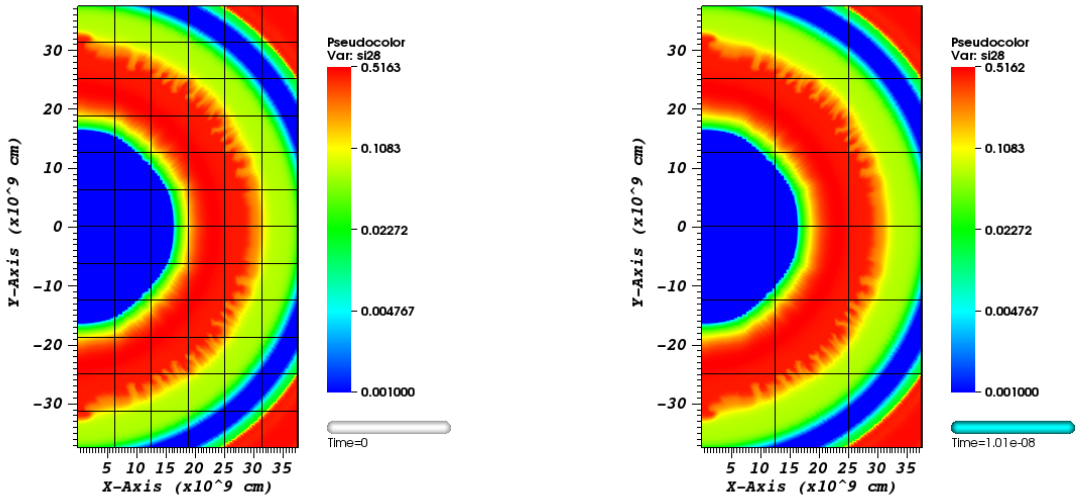

Figure 6.24 A further zoomed-in view of pseudocolor of ^{28}Si mass fraction on a log-scale overlaid on top of the grid structure pre-derefinement (left) and post-derefinement (right). The boxes correspond to AMR blocks of 192x192 cells each.

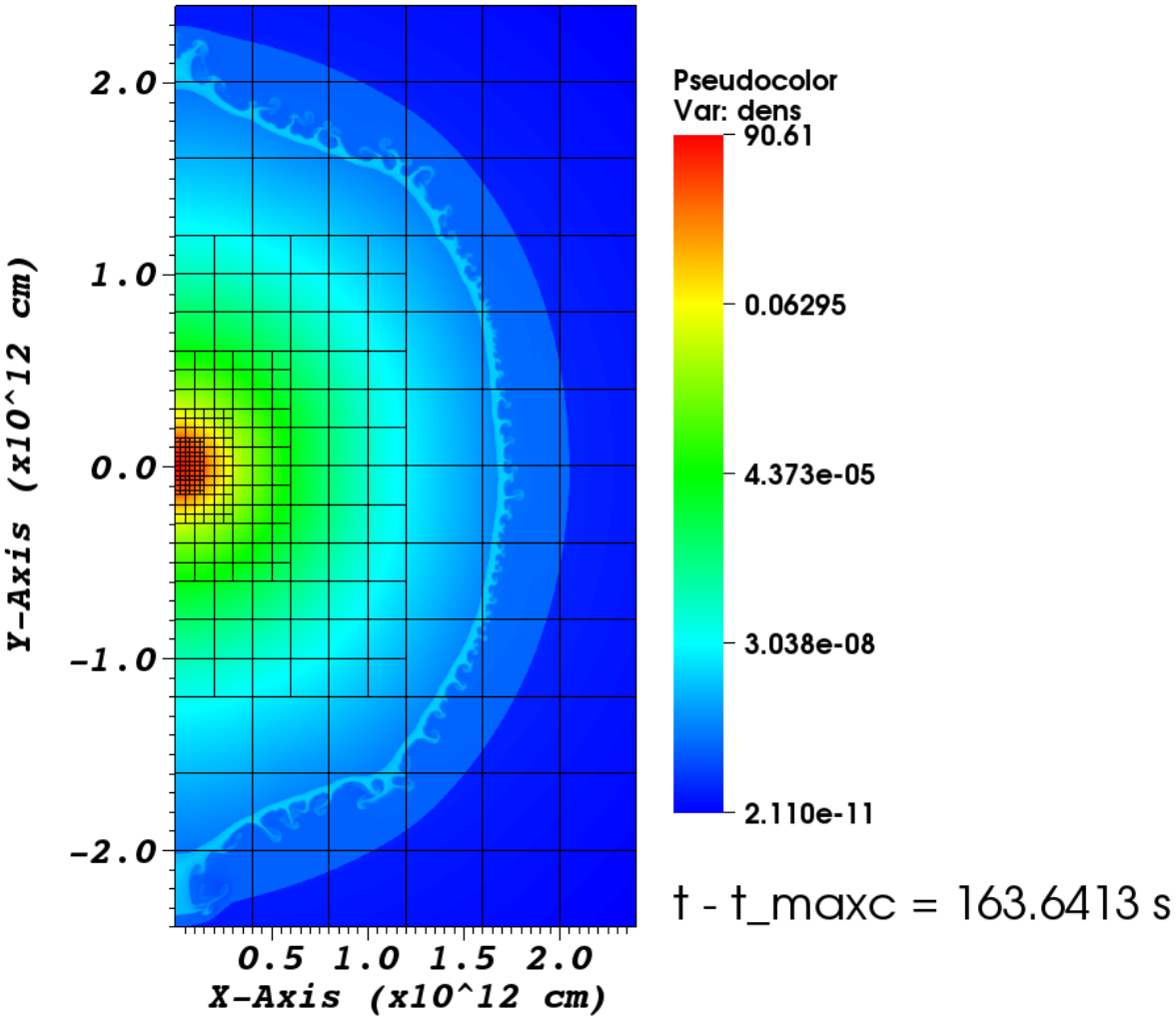

Figure 6.25 A zoomed-out view of pseudocolor of density on a log-scale overlaid on top of the grid structure at ~ 163.6 s after maximum compression. The boxes correspond to AMR blocks of 192x192 cells each.

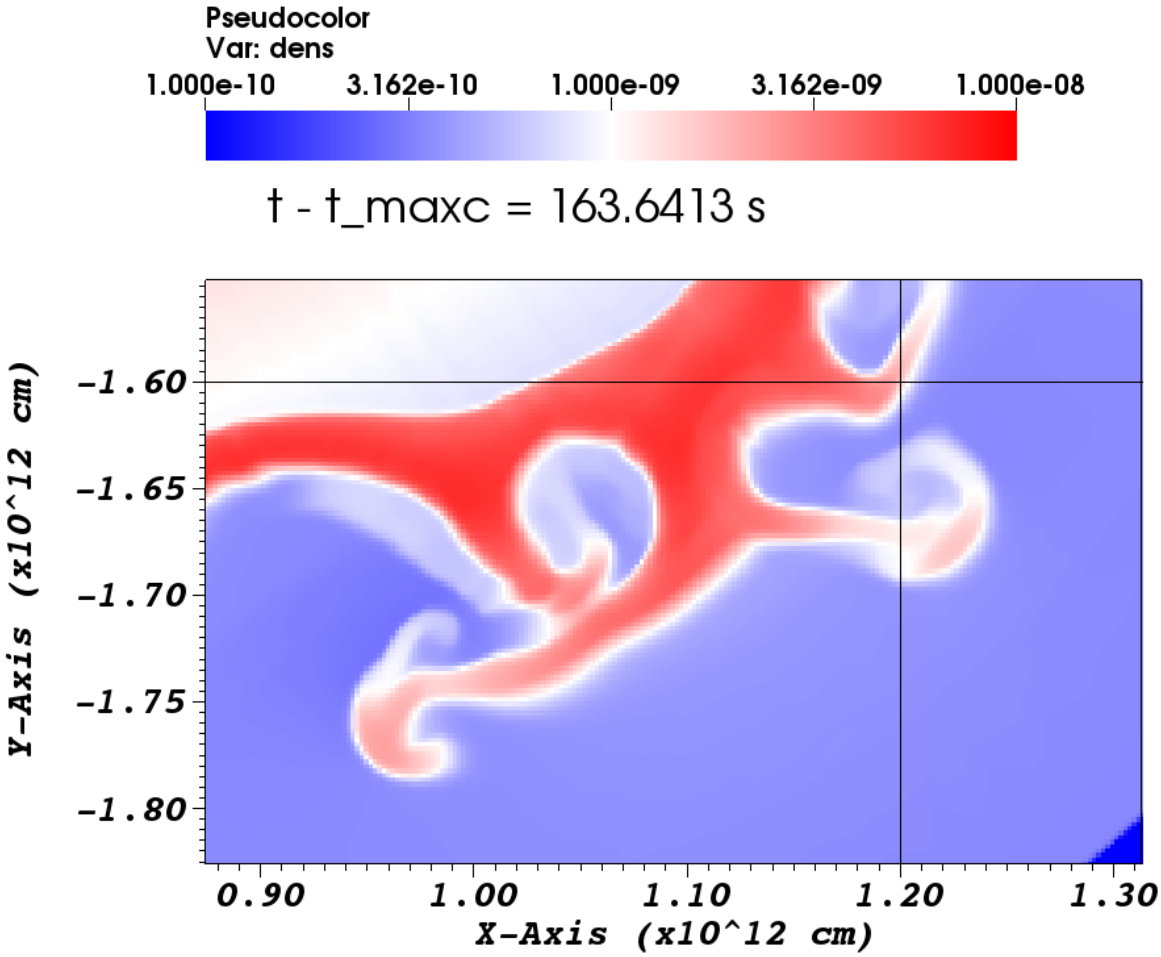

Figure 6.26 A zoomed-in view of pseudocolor (note the different color scale than in Figure 6.25 chosen to better show contrast) of density on a log-scale overlaid on top of the grid structure at ~ 163.6 s after maximum compression. The boxes correspond to AMR blocks of 192x192 cells each.

6.5 Conclusion

In this Chapter, we have explored three possible PISN signals, all of which will be useful for interpreting upcoming observations. In Section 6.2, we described our method for computing LCs, which, in addition to involving simulations with STELLA, involved further evolution with FLASH. Our method for appending the envelope was successful in creating a smooth profile without discontinuities while preserving the outer envelope structure. We presented bolometric and broad-band LCs for all four of our PISN models. Our bolometric LCs are characterized by rise times ~ 50 days shorter than others in the literature owing to the relatively low opacities predicted by STELLA and the relatively shallow envelopes of our progenitors. Explosions of our more massive models, P250 and P200, would appear as a luminous Type Ic SN and our P175 explosion as a subluminous CCSN event. Conversely, our P150 LC exhibits no Ni-powered maximum, and instead is brighter at early times due to recombination of hydrogen. One way to distinguish PISN events from other similarly appearing SNe is to catch SBO. This, however, seems to be only a possibility for our lower mass models P150 and P175 since their larger radii lead to longer SBO signals.

The fast rise to peak luminosity seen in our LCs makes our most massive model (and only superluminous model), P250, a good candidate for explaining the observations of PTF12dam. While not all of the observational characteristics can be explained by our model, we argued that the agreement was close enough that a PISN interpretation for the event cannot be ruled out.

Next, in Section 6.3, we applied our P150 and P250 explosion results to calculate the expected neutrino signal at Earth for such PISNe occurring at a distance of 10 kpc. Neutrino emission is dominated by the thermal process of pair-production, which produces all three neutrino flavors. Electron and positron captures are also included and give a slight boost to the electron neutrino component of the signal. Additionally, electron capture on copper introduces an interesting spectral feature. Due to the significantly higher core temperatures reached in P250 (see Table 4.2), thermal (and therefore overall) emission was much greater than for P150.

We described our neutrino oscillation calculation where we included effects of the surrounding stellar matter and the subsequent decoherence that results from vacuum oscillations. In general, oscillations hampered the prospects for detectability as many of the emitted electron neutrinos oscillate to other flavors (to which the neutrino detectors are less sensitive). However, a significant number of events (~ 50 for Hyper-K) is expected (for both the NMO and the IMO) for a P250 like PISN at 10 kpc. For a P150 like PISN at 10 kpc, the signal is likely to be just barely detected. These hypothetically detected signals would easily be distinguishable from those of other SN types (Type Ia and CCSN) due to their long signal duration. The

neutrino burst is expected to be Gaussian-like with an energy structure that depends on the neutrino mass ordering. The measured energy structure for those detectors sensitive to IBD is expected to be double-peaked for the NMO, but not for the IMO. A detection of high enough statistical significance could therefore place constraints on the neutrino mass ordering. Finally, for IceCube to see a signal, the PISN must occur very nearby to appear above the low-energy event background.

Lastly, in Section 6.4, we reported on the progress towards computing spectra that reflect our findings from our 3D simulations with SuperNu. We presented preliminary results comparing the bolometric LCs of SuperNu and STELLA. We described our plans for satisfying the temperature requirements of SuperNu with more FLASH simulations. We also report on the use of the SNEC code while the former procedure is being worked out. We show that either method should be suitable based on the spectra at peak luminosity we present. We then describe a method for simulating the expansion and cooling of the ejecta in 2D with FLASH. This method does a good job at preserving the interesting features that will likely affect spectra while keeping computational costs reasonable. We also report the discovery of another fluid instability that is triggered by SBO. The resultant RT features are visible in the density. While this is unlikely to affect spectra due to the compositional uniformity in the region, it is nonetheless interesting. We compare this result with a similar result from the 2D simulations of Chen et al. [Che14a].

CHAPTER

7

CONCLUSION

7.1 Summary and Implications of Results

In this dissertation, we have explored many topics relating to PISNe. Although the mechanism is relatively simple in terms of the basic physics and model predictions, many non-trivial aspects emerge when you study it. The large uncertainties involved (e.g. mass loss rates, environmental dependence of IMFs, opacities, etc.) make the topic somewhat controversial, and therefore exciting. PISNe are rich in the diversity that follows from the differing behavior of explosions across the mass range and the observational diversity from progenitor characteristics. We explored this diversity focusing on compact progenitors of intermediate metallicity.

We described the possible connection between SLSNe and PISNe citing examples of candidate events. This possibility motivated an exploration into the multidimensional effects of PISNe. While it appears clear that multidimensional effects are not important for the nucleosynthetic products and explosion energies, the mixing that set in after may be important. Understanding of this mixing will assist in exploring the possible SLSN-PISN connection as well as interpreting future transient detections. Our 3D simulations, which are the first to be published [Gil17], showed that mixing is more important than previously found in 2D, which will hopefully motivate further exploration in 3D.

Our investigation into the observational signatures of PISNe has led to many exciting

prospects for identifying PISNe. One of these prospects is catching a SBO from a low-mass PISN. The timescales of our SBO signals for P150 and P175 are not much smaller than those of the cadences of planned transient surveys. With our extremely compact model P250, we computed a superluminous synthetic LC which was shown to match many of the observational features of the SLSN PTF12dam. Most important of these features is the fast rise to peak luminosity. While the model predicts a somewhat slower rise to peak luminosity, the gap that had existed between model and observations has largely been bridged.

We also present the first calculation of neutrino emission from PISNe. We show that the neutrino signal from PISN is very similar to that of Type Ia SNe except that it is much stronger. This is not a surprise since PISNe are similar events to Type Ia SNe (both are thermonuclear explosions but PISNe are significantly more energetic and luminous in photons). We found additionally that upcoming neutrino observatories will be able to identify a nearby PISN. However, the likelihood of a PISN occurring near enough is very low. Nonetheless, the confirmed existence of VMS in the local universe proves that this probability is non-zero. If we are lucky enough to observe such an event, valuable constraints may be placed on the neutrino mass ordering which is currently one of the most exciting questions in particle physics.

We describe the current state of a very exciting project with the goal of exploring the effects of multidimensional mixing on PISNe spectra in Section 6.4. This project is naturally motivated by our findings in our 3D simulations. Mixing near the Si-O interface is incapable of redistributing the radioactive LC power source ^{56}Ni, but may affect spectra. In order to figure out if such mixing is detectable in spectra, we must perform this calculation. In order to do this calculation, further `FLASH` simulations are required. We describe our strategy of following the expansion and cooling of ejecta as the shock traverses a stellar wind. We further describe a mapping procedure in 2D that preserves the interesting features with reasonably low required CPU resources. This effort led to the result that larger-scale RT features grow even in 2D when given enough time. Furthermore, we found that SBO into the stellar wind can drive RT instabilities behind the shock.

7.2 Future Work

In the future, we plan to explore PISN properties of zero-metallicity stars computed with `GENEC`. Such models do not yet exist and are likely to make novel predictions. This expectation is based on the fact that unique properties emerged for non-zero metallicity stars. This study will aid in the interpretation of upcoming observations of the early universe (see Section 2.5).

Additionally, we plan to explore how the mixing we found depends on resolution. In Chapter 5 we saw a qualitative difference in behavior by going to higher resolution (distinct RT features

forming in the 3D case). We plan to study the effect of resolution for all models which will teach us how the mixing behavior differs between the different masses. We can then make informed predictions for the multidimensional effects on observable characteristics of low-mass PISNe.

Finally, we will continue the project on computing spectra from our multidimensional results (described in Section 6.4). We will extend our method that we have demonstrated for 2D to 3D. An added bonus that will come from this is to study mixing over a longer time-scale. We saw the instabilities continue to grow in 2D. Likewise, we expect to see the mixing we found in 3D to grow further. Although we saw no strong mixing of nickel, following this longer in 3D may lead to non-negligible effects on the resultant LC shapes.

BIBLIOGRAPHY

[Abb11] Abbasi, R. et al. "IceCube sensitivity for low-energy neutrinos from nearby supernovae". *A&A* **535**, A109 (2011), A109. arXiv: 1108.0171 [astro-ph.HE].

[Abe02] Abel, T. et al. "The Formation of the First Star in the Universe". *Science* **295** (2002), pp. 93–98. eprint: astro-ph/0112088.

[Acc16] Acciarri, R. et al. "Long-Baseline Neutrino Facility (LBNF) and Deep Underground Neutrino Experiment (DUNE) Conceptual Design Report, Volume 4 The DUNE Detectors at LBNF". *ArXiv e-prints* (2016). arXiv: 1601.02984 [physics.ins-det].

[Alm10] Almgren, A. S. et al. "CASTRO: A New Compressible Astrophysical Solver. I. Hydrodynamics and Self-gravity". *ApJ* **715** (2010), pp. 1221–1238. arXiv: 1005.0114 [astro-ph.IM].

[An16] An, F. et al. "Neutrino physics with JUNO". *Journal of Physics G Nuclear Physics* **43**.3, 030401 (2016), p. 030401. arXiv: 1507.05613 [physics.ins-det].

[Bar67] Barkat, Z. et al. "Dynamics of Supernova Explosion Resulting from Pair Formation". *Physical Review Letters* **18** (1967), pp. 379–381.

[Bet86] Bethe, H. A. "Possible explanation of the solar-neutrino puzzle". *Physical Review Letters* **56** (1986), pp. 1305–1308.

[Bli98] Blinnikov, S. I. et al. "A Comparative Modeling of Supernova 1993J". *ApJ* **496** (1998), p. 454. eprint: arXiv:astro-ph/9711055.

[Bli06] Blinnikov, S. I. et al. "Theoretical light curves for deflagration models of type Ia supernova". *A&A* **453** (2006), pp. 229–240. eprint: astro-ph/0603036.

[Bli00] Blinnikov, S. et al. "Radiation Hydrodynamics of SN 1987A. I. Global Analysis of the Light Curve for the First 4 Months". *ApJ* **532** (2000), pp. 1132–1149. eprint: astro-ph/9911205.

[Bro04] Bromm, V. & Loeb, A. "Accretion onto a primordial protostar". *New Astr.* **9** (2004), pp. 353–364. eprint: astro-ph/0312456.

[Bur06] Burrows, A. et al. "Neutrino opacities in nuclear matter". *Nuclear Physics A* **777** (2006), pp. 356–394. eprint: astro-ph/0404432.

[Cal02] Calder, A. C. et al. "On Validating an Astrophysical Simulation Code". *ApJS* **143** (2002), pp. 201–229. eprint: astro-ph/0206251.

[Cha12] Chatzopoulos, E. & Wheeler, J. C. "Effects of Rotation on the Minimum Mass of Primordial Progenitors of Pair-instability Supernovae". *ApJ* **748**, 42 (2012), p. 42. arXiv: 1201.1328 [astro-ph.HE].

[Cha14] Chatzopoulos, E. et al. "Multidimensional Simulations of Rotating Pair Instability Supernovae". *American Astronomical Society Meeting Abstracts #223*. Vol. 223. American Astronomical Society Meeting Abstracts. 2014, p. 335.06.

[Cha15] Chatzopoulos, E. et al. "Emission from Pair-instability Supernovae with Rotation". *ApJ* **799**, 18 (2015), p. 18. arXiv: 1410.0039 [astro-ph.HE].

[Che11] Chen, K.-J. et al. "Multidimensional simulations of pair-instability supernovae". *Computer Physics Communications* **182** (2011), pp. 254–256. arXiv: 1006.2385 [astro-ph.HE].

[Che14a] Chen, K.-J. et al. "Pair Instability Supernovae of Very Massive Population III Stars". *ApJ* **792**, 44 (2014), p. 44. arXiv: 1402.5960 [astro-ph.HE].

[Che14b] Chen, K.-J. et al. "Two-dimensional Simulations of Pulsational Pair-instability Supernovae". *ApJ* **792**, 28 (2014), p. 28. arXiv: 1402.4134 [astro-ph.HE].

[Che15a] Chen, K.-J. et al. "Pair-Instability Supernovae of Non-Zero Metallicity Stars". *Numerical Modeling of Space Plasma Flows ASTRONUM-2014*. Ed. by Pogorelov, N. V. et al. Vol. 498. Astronomical Society of the Pacific Conference Series. 2015, p. 47. arXiv: 1407.7550 [astro-ph.HE].

[Che15b] Chen, T.-W. et al. "The host galaxy and late-time evolution of the superluminous supernova PTF12dam". *MNRAS* **452** (2015), pp. 1567–1586. arXiv: 1409.7728.

[Cho16] Choudhury, S. et al. "Photometric metallicity map of the Large Magellanic Cloud". *MNRAS* **455** (2016), pp. 1855–1880. arXiv: 1510.05769.

[Cle15] Clementel, N. et al. "3D radiative transfer simulations of Eta Carinae's inner colliding winds - I. Ionization structure of helium at apastron". *MNRAS* **447** (2015), pp. 2445–2458. arXiv: 1412.7569 [astro-ph.SR].

[Cou13] Couch, S. M. et al. "An Improved Multipole Approximation for Self-gravity and Its Importance for Core-collapse Supernova Simulations". *ApJ* **778**, 181 (2013), p. 181. arXiv: 1307.3135 [astro-ph.HE].

[Cro16] Crowther, P. A. et al. "The R136 star cluster dissected with Hubble Space Telescope/STIS. I. Far-ultraviolet spectroscopic census and the origin of He II λ1640 in young star clusters". *MNRAS* **458** (2016), pp. 624–659. arXiv: 1603.04994 [astro-ph.SR].

[De 06] De Becker, M. et al. "Early-type stars in the young open cluster IC 1805. II. The probably single stars HD15570 and HD15629, and the massive binary/triple system HD15558". *A&A* **456** (2006), pp. 1121–1130. eprint: astro-ph/0606379.

[Den07] Densmore, J. D. et al. “A hybrid transport-diffusion method for Monte Carlo radiative-transfer simulations”. *Journal of Computational Physics* **222** (2007), pp. 485–503.

[Des18] Dessart, L. “A magnetar model for the hydrogen-rich super-luminous supernova iPTF14hls”. *A&A* **610**, L10 (2018), p. L10. arXiv: 1801.05340 [astro-ph.HE].

[Des12] Dessart, L. et al. “Superluminous supernovae: ^{56}Ni power versus magnetar radiation”. *MNRAS* **426** (2012), pp. L76–L80. arXiv: 1208.1214 [astro-ph.SR].

[Des13] Dessart, L. et al. “Radiative properties of pair-instability supernova explosions”. *MNRAS* **428** (2013), pp. 3227–3251. arXiv: 1210.6163 [astro-ph.SR].

[Dub09] Dubey, A. et al. “Extensible Component Based Architecture for FLASH, A Massively Parallel, Multiphysics Simulation Code”. *ArXiv e-prints* (2009). arXiv: 0903.4875 [cs.SE].

[Eks08] Ekström, S. et al. “Effects of rotation on the evolution of primordial stars”. *A&A* **489** (2008), pp. 685–698. arXiv: 0807.0573.

[Eks12] Ekström, S. et al. “Grids of stellar models with rotation. I. Models from 0.8 to 120 $M_\odot$ at solar metallicity ($Z = 0.014$)”. *A&A* **537**, A146 (2012), A146. arXiv: 1110.5049 [astro-ph.SR].

[Fig05] Figer, D. F. “An upper limit to the masses of stars”. *Nature* **434** (2005), pp. 192–194. eprint: astro-ph/0503193.

[Fis10] Fischer, T. et al. “Protoneutron star evolution and the neutrino-driven wind in general relativistic neutrino radiation hydrodynamics simulations”. *A&A* **517**, A80 (2010), A80. arXiv: 0908.1871 [astro-ph.HE].

[Fle71] Fleck Jr., J. A. & Cummings, J. D. “An implicit Monte Carlo scheme for calculating time and frequency dependent nonlinear radiation transport”. *Journal of Computational Physics* **8** (1971), pp. 313–342.

[Fry01] Fryer, C. L. et al. “Pair-Instability Supernovae, Gravity Waves, and Gamma-Ray Transients”. *ApJ* **550** (2001), pp. 372–382. eprint: astro-ph/0007176.

[Fry00] Fryxell, B. et al. “FLASH: An Adaptive Mesh Hydrodynamics Code for Modeling Astrophysical Thermonuclear Flashes”. *ApJS* **131** (2000), pp. 273–334.

[Fuk03] Fukuda, S. et al. “The Super-Kamiokande detector”. *Nuclear Instruments and Methods in Physics Research A* **501** (2003), pp. 418–462.

[Ful82] Fuller, G. M. et al. “Stellar weak interaction rates for intermediate-mass nuclei. II - $A = 21$ to $A = 60$”. *ApJ* **252** (1982), pp. 715–740.

[Gal12] Gal-Yam, A. “Luminous Supernovae”. *Science* **337** (2012), p. 927. arXiv: 1208.3217.

[Gal09] Gal-Yam, A. et al. “Supernova 2007bi as a pair-instability explosion”. *Nature* **462** (2009), pp. 624–627. arXiv: 1001.1156.

[Gar81] Garmany, C. D. & Massey, P. “HD 15558 : an extremely luminous O-type binary star.” *Publications of the Astronomical Society of the Pacific* **93**.554 (1981), p. 500.

[Gar16] Garnavich, P. M. et al. “Shock Breakout and Early Light Curves of Type II-P Supernovae Observed with Kepler”. *ApJ* **820**, 23 (2016), p. 23. arXiv: 1603.05657 [astro-ph.SR].

[Geo17] Georgy, C. et al. “Possible pair-instability supernovae at solar metallicity from magnetic stellar progenitors”. *A&A* **599**, L5 (2017), p. L5. arXiv: 1702.02340 [astro-ph.SR].

[Gil17] Gilmer, M. S. et al. “Pair-instability Supernova Simulations: Progenitor Evolution, Explosion, and Light Curves”. *ApJ* **846**, 100 (2017), p. 100. arXiv: 1706.07454 [astro-ph.SR].

[Giu98] Giunti, C. et al. “When do neutrinos cease to oscillate?” *Physics Letters B* **421** (1998), pp. 237–244. eprint: hep-ph/9709494.

[Grä11] Gräfener, G. et al. “The Eddington factor as the key to understand the winds of the most massive stars. Evidence for a Γ-dependence of Wolf-Rayet type mass loss”. *A&A* **535**, A56 (2011), A56. arXiv: 1106.5361 [astro-ph.SR].

[Heg02] Heger, A. & Woosley, S. E. “The Nucleosynthetic Signature of Population III”. *ApJ* **567** (2002), pp. 532–543. eprint: astro-ph/0107037.

[Hir87] Hirata, K. et al. “Observation of a neutrino burst from the supernova SN1987A”. *Phys. Rev. Lett.* **58** (14 1987), pp. 1490–1493.

[Hir07] Hirschi, R. “Very low-metallicity massive stars:. Pre-SN evolution models and primary nitrogen production”. *A&A* **461** (2007), pp. 571–583. eprint: arXiv:astro-ph/0608170.

[Hir15] Hirschi, R. “Evolution and Nucleosynthesis of Very Massive Stars”. *Very Massive Stars in the Local Universe*. Ed. by Vink, J. S. Vol. 412. Astrophysics and Space Science Library. 2015, p. 157. arXiv: 1409.7053 [astro-ph.SR].

[Hos18] Hosek, M. et al. “The Initial Mass Function of the Arches Cluster”. *American Astronomical Society Meeting Abstracts # 231*. Vol. 231. American Astronomical Society Meeting Abstracts. 2018, p. 214.05.

[16] “Hyper-Kamiokande Design Report” (2016).

[Ins17] Inserra, C. et al. “Complexity in the light curves and spectra of slow-evolving superluminous supernovae”. *MNRAS* **468** (2017), pp. 4642–4662. arXiv: 1701.00941 [astro-ph.HE].

[Ito96] Itoh, N. et al. “Neutrino Energy Loss in Stellar Interiors. VII. Pair, Photo-, Plasma, Bremsstrahlung, and Recombination Neutrino Processes”. *ApJS* **102** (1996), p. 411.

[Jer16] Jerkstrand, A. et al. “Nebular spectra of pair-instability supernovae”. *MNRAS* **455** (2016), pp. 3207–3229. arXiv: 1510.02698 [astro-ph.SR].

[Jer17] Jerkstrand, A. et al. “Long-duration Superluminous Supernovae at Late Times”. *ApJ* **835**, 13 (2017), p. 13. arXiv: 1608.02994 [astro-ph.HE].

[Jog11] Joggerst, C. C. & Whalen, D. J. “The Early Evolution of Primordial Pair-instability Supernovae”. *ApJ* **728**, 129 (2011), p. 129. arXiv: 1010.4360.

[Jog10] Joggerst, C. C. et al. “The Nucleosynthetic Imprint of 15-40 M_{sun} Primordial Supernovae on Metal-Poor Stars”. *ApJ* **709** (2010), pp. 11–26. arXiv: 0907.3885.

[Kas11] Kasen, D. et al. “Pair Instability Supernovae: Light Curves, Spectra, and Shock Breakout”. *ApJ* **734**, 102 (2011), p. 102. arXiv: 1101.3336 [astro-ph.HE].

[Kas10] Kashi, A. & Soker, N. “Periastron Passage Triggering of the 19th Century Eruptions of Eta Carinae”. *ApJ* **723** (2010), pp. 602–611. arXiv: 0912.1439 [astro-ph.SR].

[Koe06] Koen, C. “On the upper limit on stellar masses in the Large Magellanic Cloud cluster R136”. *MNRAS* **365** (2006), pp. 590–594.

[Koz15] Kozyreva, A. & Blinnikov, S. “Can pair-instability supernova models match the observations of superluminous supernovae?” *MNRAS* **454** (2015), pp. 4357–4365. arXiv: 1510.00439 [astro-ph.HE].

[Koz14a] Kozyreva, A. et al. “Explosion and nucleosynthesis of low-redshift pair-instability supernovae”. *A&A* **566**, A146 (2014), A146. arXiv: 1405.6340 [astro-ph.HE].

[Koz14b] Kozyreva, A. et al. “Observational properties of low-redshift pair instability supernovae”. *A&A* **565**, A70 (2014), A70. arXiv: 1403.5212 [astro-ph.HE].

[Koz17] Kozyreva, A. et al. “Fast evolving pair-instability supernova models: evolution, explosion, light curves”. *MNRAS* **464** (2017), pp. 2854–2865. arXiv: 1610.01086 [astro-ph.HE].

[Kru14] Krumholz, M. R. “The Formation of Very Massive Stars”. *Very Massive Stars in the Local Universe*. Ed. by Vink, J. S. Springer, 2014. Chap. 3, pp. 43–71.

[Kuc14] Kuchugov, P. A. et al. “The differences in the development of Rayleigh-Taylor instability in 2D and 3D geometries”. *Plasma Physics Reports* **40**.6 (2014), pp. 451–458.

[Lan00] Langanke, K. & Martínez-Pinedo, G. “Shell-model calculations of stellar weak interaction rates: II. Weak rates for nuclei in the mass range /A=45-65 in supernovae

environments". *Nuclear Physics A* **673** (2000), pp. 481–508. eprint: nucl-th/0001018.

[Lan03] Langanke, K. et al. "Electron Capture Rates on Nuclei and Implications for Stellar Core Collapse". *Physical Review Letters* **90**.24, 241102 (2003), p. 241102. eprint: astro-ph/0302459.

[Lan07] Langer, N. et al. "Pair creation supernovae at low and high redshift". *A&A* **475** (2007), pp. L19–L23. arXiv: 0708.1970.

[Löh87] Löhner, R. "An Adaptive Finite Element Scheme for Transient Problems in CFD". *Comput. Methods Appl. Mech. Eng.* **61**.3 (1987), pp. 323–338.

[Mac99] MacNeice, P. et al. "PARAMESH: A parallel adaptive mesh refinement community toolkit". **126** (1999).

[Mar17] Marshall, P. et al. *LSST Science Collaborations Observing Strategy White Paper: "Science-driven Optimization of the LSST Observing Strategy"*. 2017.

[Mar08] Martins, F. et al. "The most massive stars in the Arches cluster". *A&A* **478** (2008), pp. 219–233. arXiv: 0711.0657.

[Mas91] Massey, P. & Thompson, A. B. "Massive stars in CYG OB2". *AJ* **101** (1991), pp. 1408–1428.

[Mat99] Matzner, C. D. & McKee, C. F. "The Expulsion of Stellar Envelopes in Core-Collapse Supernovae". *ApJ* **510** (1999), pp. 379–403. eprint: astro-ph/9807046.

[Mir15] Mirizzi, A. et al. "Supernova Neutrinos: Production, Oscillations and Detection". *ArXiv e-prints* (2015). arXiv: 1508.00785 [astro-ph.HE].

[Mor18] Moriya, T. J. et al. "Superluminous supernovae". *ArXiv e-prints* (2018). arXiv: 1803.01875 [astro-ph.HE].

[Mor15] Morozova, V. et al. "Light Curves of Core-collapse Supernovae with Substantial Mass Loss Using the New Open-source SuperNova Explosion Code (SNEC)". *ApJ* **814**, 63 (2015), p. 63. arXiv: 1505.06746 [astro-ph.HE].

[Nic13] Nicholl, M. et al. "Slowly fading super-luminous supernovae that are not pair-instability explosions". *Nature* **502** (2013), pp. 346–349. arXiv: 1310.4446.

[Nic17] Nicholl, M. et al. "The Magnetar Model for Type I Superluminous Supernovae. I. Bayesian Analysis of the Full Multicolor Light-curve Sample with MOSFiT". *ApJ* **850**, 55 (2017), p. 55. arXiv: 1706.00825 [astro-ph.HE].

[Noe12] Noebauer, U. M. et al. “Monte Carlo radiation hydrodynamics: methods, tests and application to Type Ia supernova ejecta”. *MNRAS* **425** (2012), pp. 1430–1444. arXiv: 1206.6263 [astro-ph.HE].

[OCo10] O’Connor, E. & Ott, C. D. “A new open-source code for spherically symmetric stellar collapse to neutron stars and black holes”. *Classical and Quantum Gravity* **27**.11, 114103 (2010), p. 114103. arXiv: 0912.2393 [astro-ph.HE].

[Oda94] Oda, T. et al. “Rate Tables for the Weak Processes of sd-Shell Nuclei in Stellar Matter”. *Atomic Data and Nuclear Data Tables* **56** (1994), pp. 231–403.

[Odr11] Odrzywolek, A. & Plewa, T. “Probing thermonuclear supernova explosions with neutrinos”. *A&A* **529**, A156 (2011), A156. arXiv: 1006.0490 [astro-ph.SR].

[Par86] Parke, S. J. “Nonadiabatic level crossing in resonant neutrino oscillations”. *Physical Review Letters* **57** (1986), pp. 1275–1278.

[Qui12] Quimby, R. M. et al. “Discovery of a Super-Luminous Supernova, PTF12dam”. *The Astronomer’s Telegram* **4121** (2012).

[Rak67] Rakavy, G. & Shaviv, G. “Instabilities in Highly Evolved Stellar Models”. *ApJ* **148** (1967), p. 803.

[Sal55] Salpeter, E. E. “The Luminosity Function and Stellar Evolution.” *ApJ* **121** (1955), p. 161.

[Sch94] Schmidt, B. P. et al. “The expanding photosphere method applied to SN 1992am AT CZ = 14 600 km/s”. *AJ* **107** (1994), pp. 1444–1452.

[Sch18] Schneider, F. R. N. et al. “An excess of massive stars in the local 30 Doradus starburst”. *Science* **359** (2018), pp. 69–71. arXiv: 1801.03107 [astro-ph.SR].

[Sch08] Schnurr, O. et al. “The very massive binary NGC 3603-A1”. *MNRAS* **389** (2008), pp. L38–L42. arXiv: 0806.2815.

[Sch09] Schuster, M. T. et al. “Imaging the Cool Hypergiant NML Cygni’s Dusty Circumstellar Envelope with Adaptive Optics”. *The Astrophysical Journal* **699**.2 (2009), p. 1423.

[Sod08] Soderberg, A. M. et al. “An extremely luminous X-ray outburst at the birth of a supernova”. *Nature* **453** (2008), pp. 469–474. arXiv: 0802.1712.

[Sta14] Stacy, A. & Bromm, V. “The First Stars: A Low-mass Formation Mode”. *ApJ* **785**, 73 (2014), p. 73. arXiv: 1307.1798.

[Sta16] Stacy, A. et al. “Building up the Population III initial mass function from cosmological initial conditions”. *MNRAS* **462** (2016), pp. 1307–1328. arXiv: 1603.09475.

[Ste13] Steiner, A. W. et al. “Core-collapse Supernova Equations of State Based on Neutron Star Observations”. *ApJ* **774**, 17 (2013), p. 17. arXiv: 1207.2184 [astro-ph.SR].

[Sul16] Sullivan, C. et al. “The Sensitivity of Core-collapse Supernovae to Nuclear Electron Capture”. *ApJ* **816**, 44 (2016), p. 44. arXiv: 1508.07348 [astro-ph.HE].

[Tim00] Timmes, F. X. & Swesty, F. D. “The Accuracy, Consistency, and Speed of an Electron-Positron Equation of State Based on Table Interpolation of the Helmholtz Free Energy”. *ApJS* **126** (2000), pp. 501–516.

[Tol17] Tolstov, A. et al. “Ultraviolet Light Curves of Gaia16apd in Superluminous Supernova Models”. *ApJ* **845**, L2 (2017), p. L2. arXiv: 1707.05746 [astro-ph.HE].

[Tor07] Tornatore, L. et al. “Population III stars: hidden or disappeared?” *MNRAS* **382** (2007), pp. 945–950. arXiv: 0707.1433.

[Tot98] Totani, T. et al. “Future Detection of Supernova Neutrino Burst and Explosion Mechanism”. *ApJ* **496** (1998), pp. 216–225. eprint: astro-ph/9710203.

[Vin15] Vink, J. S., ed. *Very Massive Stars in the Local Universe*. Vol. 412. Astrophysics and Space Science Library. Springer International Publishing Switzerland, 2015. arXiv: 1406.4836 [astro-ph.SR].

[Vin14] Vink, J. S. “Very Massive Stars in the Local Universe”. *Very Massive Stars in the Local Universe*. Ed. by Vink, J. S. Springer, 2014. Chap. 1, pp. 1–6.

[Wal08] Waldman, R. “Around the Pair Instability Valley Massive SN Progenitors”. *The Art of Modeling Stars in the 21st Century*. Ed. by Deng, L. & Chan, K. L. Vol. 252. IAU Symposium. 2008, pp. 329–332. arXiv: 0805.3874.

[Wan17] Wang, L. et al. “A First Transients Survey with JWST: the FLARE project”. *ArXiv e-prints* (2017). arXiv: 1710.07005 [astro-ph.IM].

[Wan16] Wang, S. Q. et al. “A Triple-energy-source Model for Superluminous Supernova iPTF13ehe”. *ApJ* **828**, 87 (2016), p. 87. arXiv: 1509.05543 [astro-ph.HE].

[Wha13] Whalen, D. J. et al. “Finding the First Cosmic Explosions. I. Pair-instability Supernovae”. *ApJ* **777**, 110 (2013), p. 110. arXiv: 1211.4979.

[Wha14a] Whalen, D. J. et al. “Finding the First Cosmic Explosions. III. Pulsational Pair-instability Supernovae”. *ApJ* **781**, 106 (2014), p. 106. arXiv: 1311.1221.

[Wha14b] Whalen, D. J. et al. “Pair-instability Supernovae in the Local Universe”. *ApJ* **797**, 9 (2014), p. 9. arXiv: 1312.5360 [astro-ph.HE].

[Whe17] Wheeler, J. C. et al. “Circumstellar Interaction Models for the Bolometric Light Curve of Type I Superluminous SN 2017egm”. *ApJ* **851**, L14 (2017), p. L14. arXiv: 1710.04994 [astro-ph.HE].

[Wol14] Wollaeger, R. T. & van Rossum, D. R. “Radiation Transport for Explosive Outflows: Opacity Regrouping”. *ApJS* **214**, 28 (2014), p. 28. arXiv: 1407.3833 [astro-ph.HE].

[Wol13] Wollaeger, R. T. et al. “Radiation Transport for Explosive Outflows: A Multigroup Hybrid Monte Carlo Method”. *ApJS* **209**, 36 (2013), p. 36. arXiv: 1306.5700 [astro-ph.HE].

[Woo07] Woosley, S. E. et al. “Pulsational pair instability as an explanation for the most luminous supernovae”. *Nature* **450** (2007), pp. 390–392. arXiv: 0710.3314.

[Wri16] Wright, W. P. et al. “Neutrinos from type Ia supernovae: The deflagration-to-detonation transition scenario”. *Phys. Rev. D* **94**.2, 025026 (2016), p. 025026. arXiv: 1605.01408 [astro-ph.HE].

[Wri17a] Wright, W. P. et al. “Neutrinos from type Ia supernovae: The gravitationally confined detonation scenario”. *Phys. Rev. D* **95**.4, 043006 (2017), p. 043006. arXiv: 1609.07403 [astro-ph.HE].

[Wri17b] Wright, W. P. et al. “Neutrino signal from pair-instability supernovae”. *Phys. Rev. D* **96** (10 2017), p. 103008.

[Yoo12] Yoon, S.-C. et al. “Evolution of massive Population III stars with rotation and magnetic fields”. *A&A* **542**, A113 (2012), A113. arXiv: 1201.2364 [astro-ph.SR].

[Yos08] Yoshida, N. et al. “Protostar Formation in the Early Universe”. *Science* **321** (2008), p. 669. arXiv: 0807.4928.

[Yos11] Yoshida, T. & Umeda, H. “A progenitor for the extremely luminous Type Ic supernova 2007bi”. *MNRAS* **412** (2011), pp. L78–L82. arXiv: 1101.0635 [astro-ph.SR].

[Yus13] Yusof, N. et al. “Evolution and fate of very massive stars”. *MNRAS* **433** (2013), pp. 1114–1132. arXiv: 1305.2099 [astro-ph.SR].